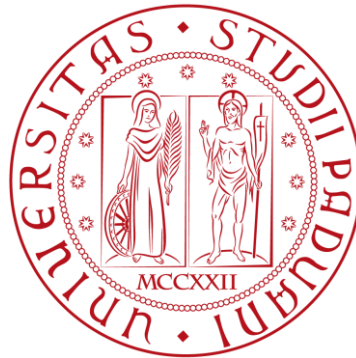# UNIVERSITÀ DEGLI STUDI DI PADOVA

Dipartimento di Ingegneria industriale DII

Corso di Laurea Magistrale in Ingegneria Aerospaziale

Development of a sensor for microvibrations measurement in the AlbaSat CubeSat mission

Studente: Docente:
NUNZIO MICALI   Prof. ALESSANDRO FRANCESCONI

ANNO ACCADEMICO 2022-2023

I never lose.
I either win or learn.
("N. Mandela")

ACKNOWLEDGMENTS

Voglio dedicare questo lavoro di tesi anzi, interamente, il mio percorso universitario alle due persone che ho più a cuore: i miei nonni, Silvana e Nuccio. Colonne portanti della mia vita, da cui ho potuto apprendere tutto ciò che so oggi. Spero di essere riuscito a renderli fieri di questo traguardo ottenuto, ricambiando, seppur in diversa misura, l'investimento che hanno fatto con me.

Accanto a loro, tutto il resto della famiglia: mamma Eleonora, papà Francesco, mia sorella Greta e ultimo, ma non per importanza, mio zio Giovanni.

Mi sento di dover ringraziare, in questo frangente, anche, un'altra persona speciale con cui ho avuto la possibilità di condividere la mia carriera universitaria, anzi la nostra: Riccardo. Insieme, siamo dove siamo oggi, dopo tanti sacrifici di studio. Mi sono sentito membro della sua famiglia come, credo, lui della mia; questa fratellanza ci ha motivati a raggiungere il traguardo della Laurea.

Un sincero ringraziamento va anche al Professore Alessandro Francesconi, che ha contribuito eccellentemente alle conoscenze da me apprese e al mio supervisore Federico Basana, lavoratore instancabile e devoto ma anche una persona semplice con cui condividere una risata.

Per finire, vorrei esprimere un sentimento di gratitudine anche a miei amici più cari, quelli con cui sono cresciuto, tra Caltagirone ed Alì Terme, e quelli più recenti, conosciuti a Padova ma anche a Barcellona: immensamente grazie per essere stati al mio fianco e per aver reso questo viaggio assolutamente più piacevole.

ABSTRACT

Microvibrations on spacecraft represent an issue for payloads requiring high pointing accuracy and/or stability over time, and they might represent a particular concern for CubeSats and small satellites that, usually, are not equipped with very-high performance attitude control systems. Hence, collecting reliable measures of the vibration spectra during the operations of a CubeSat represents a significant research activity.

This thesis presents the development of a sensor, configured as a payload within the AlbaSat mission, capable of accurately measuring the microvibrations in space, with particular focus on those produced by the Momentum Exchange Devices (MED), i.e., Reaction or Momentum Wheels, that represent one of the most important microvibrations sources. The thesis takes place in the framework of the AlbaSat mission. AlbaSat is a 2U CubeSat developed by a student team of the University of Padova under the "Fly Your Satellite! – Design Booster" programme promoted by the European Space Agency (ESA). The mission has four different objectives: (1) to collect measurements of the space debris environment in-situ, (2) to measure the microvibrations on board the CubeSat, (3) to precisely determine the position of the satellite through laser ranging and (4) to investigate alternative systems for possible Satellite Quantum Communication applications on nanosatellites.

The requirements for the correct sizing of the sensor and the chosen physical and functional architecture are defined and presented in the thesis.

A meticulous schedule for functional tests is finally outlined, aimed at verifying the correct functionality of the microvibration sensor. These tests serve as a starting point for the future development of the payload.

SOMMARIO

Le microvibrazioni sui veicoli spaziali rappresentano un problema per i carichi utili che richiedono alta precisione di puntamento e/o stabilità nel tempo e possono rappresentare una preoccupazione particolare per i CubeSats e i satelliti di piccole dimensioni che, di solito, non sono equipaggiati con sistemi di controllo d'assetto ad alte prestazioni. Pertanto, raccogliere misurazioni affidabili degli spettri di vibrazione durante le operazioni di un CubeSat rappresenta una significativa attività di ricerca.

Questa tesi presenta lo sviluppo di un sensore, configurato come carico utile all'interno della missione AlbaSat, in grado di misurare con precisione le microvibrazioni nello spazio, con particolare attenzione a quelle prodotte dai Momentum Exchange Devices (MED), ossia, Reaction o Momentum Wheels, che rappresentano una delle fonti di microvibrazioni più importanti.

La tesi si colloca nell'ambito della missione AlbaSat. AlbaSat è un CubeSat di 2U sviluppato da un gruppo di studenti dell'Università di Padova nell'ambito del programma "Fly Your Satellite! – Design Booster" promosso dall'Agenzia Spaziale Europea (ESA). La missione ha quattro obiettivi differenti: (1) raccogliere misurazioni dell'ambiente dei detriti spaziali in situ, (2) misurare le microvibrazioni a bordo del CubeSat, (3) determinare con precisione la posizione del satellite tramite rilevamento laser e (4) investigare sistemi alternativi per possibili applicazioni di Comunicazione Quantistica Satellitare su nanosatelliti.

I requisiti per il corretto dimensionamento del sensore e l'architettura fisica e funzionale scelta sono definiti e presentati nella tesi.

Infine, viene delineato un dettagliato programma di test funzionali, mirato a verificare la corretta funzionalità del sensore di microvibrazioni. Questi test fungono da punto di partenza per lo sviluppo futuro del payload.

x

LIST OF ACRONYMS

ACS	Attitude Control System
ADC	Analog to Digital Converter
ADCS	Attitude Determination and Control Subsystem
AIT	Assembly, Integration and Test
AIV	Assembly, Integration and Verification
BLDC	BrushLess Direct Current
CCRs	Corner Cube Retroreflectors
CLK	Clock
CNES	Centre National d'Études Spatiales
COTS	Commercial Off The Shelf
CS	Chip Select
DAC	Digital to Analog Converter
DC	Direct Current
DFT	Discrete Fourier Transform
DII	Dipartimento di Ingegneria Industriale
DIT	Dynamic Interaction Test
DM	Development Model
DoF	Degree of Freedom
DSP	Digital Signal Processor
EGSE	Electrical Ground Support Equipment
EQM	Engineering Qualification Model
ESA	European Space Agency
EPS	Electric Power Subsystem
FEM	Finite Element Model
FFT	Fast Fourier Transform
FGS	Fine Guidance Sensor
FM	Flight Model

FOV	Field Of View
FS	Full Scale
FSM	Fine Steering Mirror
FT	Functional Test
FTP	Functional Test Plan
FYS	Fly You Satellite!
GPIO	General Purpose Input/Output
GS	Ground Station
GSE	Ground Station Equipment
HGA	High Gain Antenna
HIL	Hardware-In-the-Loop
HPF	High-Pass Filter
HST	Hubble Space Telescope
IS	Impact Sensor
ISIM	Integrated Science Instrument Module
JAXA	Japan Aerospace Exploration Agency
JWST	James Webb Space Telescope
LEO	Low Earth Orbit
LEOP	Launch and Early Operations Phase
LOS	Line Of Sight
LPF	Low-Pass Filter
LST	Large Space Telescope
MED	Momentum Exchange Devices
MEMS	Micro Electro-Mechanical Systems
MISO	Master Input Slave Output
MOSI	Master Output Slave Input
MRR	Modulating Retro Reflector
MVS	Micro-Vibrations Sensor
MW	Momentum Wheel
MWA	Momentum Wheel Assembly
NASA	National Aeronautics and Space Administration
OBC	On Board Computer

ODR	Output Data Rate
OTE	Optical Telescope Element
PASTEC	PASsager TEChnologique
PCB	Printed Circuit Board
PCS	Pointing Control System
PFM	Proto-Flight Model
PLL	Phase-Locked Loop
PSD	Power Spectral Density
QM	Qualification Model
QPL	Quantum Payload
RAM	Random Access Memory
RF	Radio Frequency Subsystem
RFT	Reduced Functional Test
RW	Reaction Wheel
RWA	Reaction Wheel Assembly
SA	Solar Array
SDO	Solar Dynamics Observatory
SDTV	Structural Dynamics Test Vehicle
SLR	Satellite Laser Ranging
SNR	Signal Noise Ratio
SOHO	Solar and Heliospheric Observatory
SRAM	Static Random Access Memory
TBC	To Be Confirmed
TRL	Technology Readiness Level
TT&C	Telemetry, Tracking and Command

LIST OF FIGURES

LIST OF TABLES

CONTENTS

Chapter 1

INTRODUCTION

In an era where space economy plays an increasingly pivotal role in advancing the comprehension of the universe, the miniaturization and cost-effectiveness introduced by CubeSats have revolutionized the accessibility of space missions for scientific research, technological advancement, and educational pursuits. Compact and standardized satellites have revolutionized the space industry, making it possible to conduct groundbreaking experiments and missions that were once limited to larger and cost-prohibitive spacecraft.

Among the numerous challenges faced by CubeSat missions, one critical aspect is their control and stability in the space environment. Specifically, the precise measurement and mitigation of microvibrations originating from on-board components, such as as Momentum Exchange Devices (MED) e.g., Momentum Wheels (MWs) or Reaction Wheels (RWs), take on paramount importance for the success of scientific observations and delicate experiments.

This thesis delves into the complex domain of microvibrations in CubeSats, with a focused emphasis on the development and verification of a Micro-Vibrations Sensor (MVS). The main goal of this research is to design a sensor capable of measuring microvibrations generated by a MW installed on a CubeSat. By accomplishing this goal, the study endeavours to enrich the understanding of the microvibration environment within the satellite and devise strategies to enhance overall stability and precision in future CubeSats missions.

This Master Thesis is organized as follows. It commences with an overview of the AlbaSat mission, which is part of the European Space Agency (ESA) "Fly Your Satellite!" (FYS) project. Subsequently, following a literature review combined with an investigation into the state of the art of missions that have focused on the study of

microvibrations, the sources of disturbance that generate microvibrations are analysed. Furthermore, the study delves deeper into characterizing the MED microvibrations and determining their frequency range, which is crucial when selecting appropriate sensors.

Additionally, the thesis outlines the process for the functional testing of the MVS payload. This method ensures the verification and validation of the sensor performance. The experimental campaign aims to assess the MVS capabilities in capturing microvibrations produced under various operational scenarios.

Ultimately, this research strives to contribute to the advancement of CubeSat technology, facilitating their integration into intricate space missions with elevated scientific and exploratory objectives. The investigation seeks to unravel the microcosmos of CubeSat stability, thereby paving the path towards augmented precision, reliability, and efficiency in future small satellite endeavours [1].

"Fly Your Satellite! – Design Booster" is a recurring hands-on program conducted by the Education Office of the ESA. FYS was established with the primary aim of supporting university student teams in developing their own CubeSats, permitting the transfer of knowledge and expertise from ESA specialists to the students. The selected teams are guided through project reviews and supervised during the design consolidation and verification activities, adhering to ESA professional practice and tailored standards fitting the scope of university CubeSat projects.

1.1 The AlbaSat Mission

Alba CubeSat UniPD is a student team from the University of Padova with the goal of launching a student-built CubeSat into space. The primary objective of the team is to provide an educational opportunity for students to engage in hands-on activities during their studies. It was founded in 2019 by a student initiative.

1.1.1 Mission Description

The proposed mission encompasses four distinct objectives:

1. To collect in-situ measurements of the $sub-mm$ space debris environment in LEO (Low Earth Orbit);
2. To study the microvibration environment on the satellite due to MW;
3. To do precise orbit and attitude determination through laser ranging;

4. To investigate alternative systems for possible Satellite Quantum Communication applications on nanosatellites.

The collected data will contribute to advancing the understanding of the space environment and provide valuable support to ongoing research activities at the University of Padova.

To accomplish the mission, the team is currently developing AlbaSat, a 2U CubeSat equipped with four distinct payloads. The first payload is an Impact Sensor (IS), that will be placed on a satellite outer face to detect and count the number of debris impacts. The second payload is a Commercial Off The Shelf (COTS) sensor designed to measure microvibrations experienced by the satellite during its mission phases. The third payload consists of several Corner Cube Retroreflectors (CCRs) distributed across different faces of the CubeSat. These CCRs will play a crucial role in precisely determining the position of AlbaSat using Satellite Laser Ranging (SLR) techniques. Lastly, the fourth payload is a Modulating Retro Reflector (MRR), featuring a CCR with a Micro Electro-Mechanical Systems (MEMS) Grating Modulator as one of its mirrors. The MRR deformations will alter the reflection angle of a ground-shined laser beam, thereby achieving its modulation. Throughout the 2U platform, COTS components will be widely utilized, encompassing subsystems such as Telemetry, Tracking, and Control System (TT&C), Electric Power System (EPS), Attitude Determination Control System (ADCS), and On-Board Computer (OBC).

1.1.2 *Mission Phases*

The mission comprises four key phases: Launch and Early Orbit Phase (LEOP), Commissioning, Routine, and Disposal.

1. LEOP: This phase starts from in-orbit deployment and continues until the satellite complete all the after-deployment tasks. The mission phase includes launch and orbit insertion, detumbling manoeuvre, and first contact with Ground Station (GS).

2. Commissioning: The spacecraft reaches a fully operational capabilities during this phase. Procedures for GS passes are verified, the IS and the MVS are activated, and the Quantum Payload (QPL) is tested.

3. Routine: In this phase, the spacecraft collects IS data and transmits beacons in its nominal mode. GS passes and QPL activities are performed. The Microvibrations Sensor (MVS) is activated to collect data during periods without GS contact.

4. Disposal: The spacecraft is safely brought to the end of its mission during the disposal phase.

1.1.3 *System Description*

A high-level functional architecture of the system is shown in Figure 1.
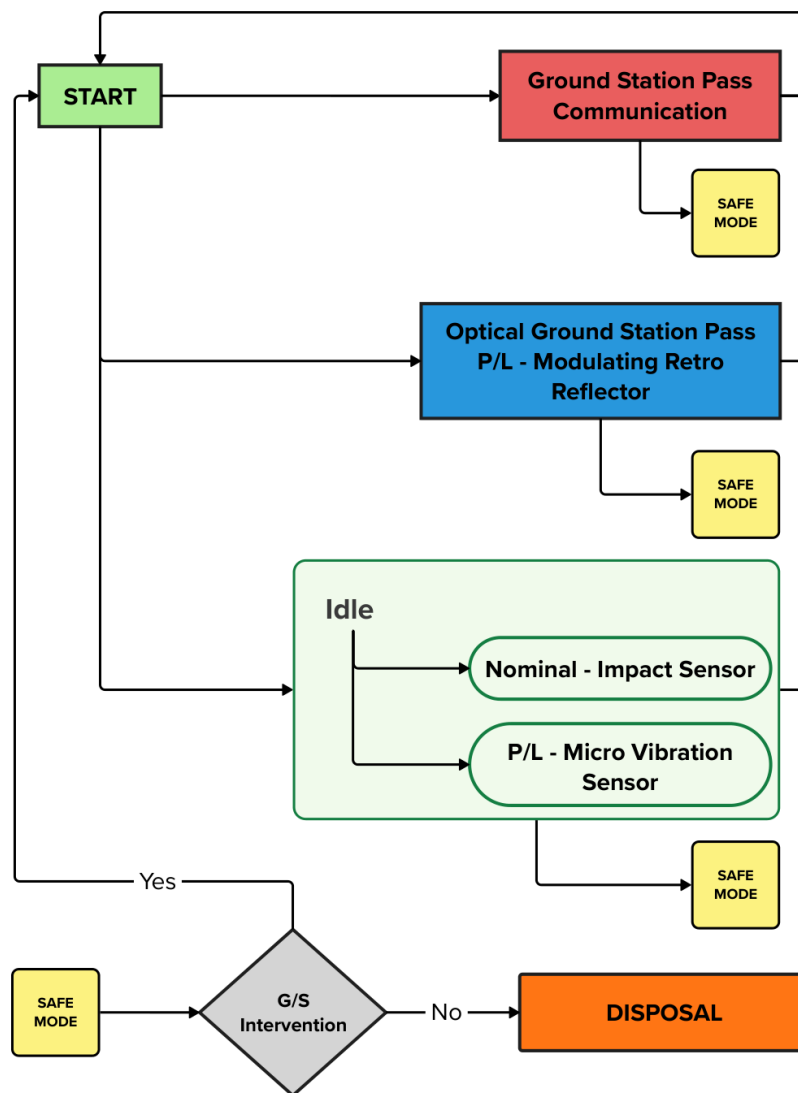
Figure 1 - Functional architecture of the AlbaSat system.

A graphical representation of the AlbaSat CubeSat is given in Figure 2.
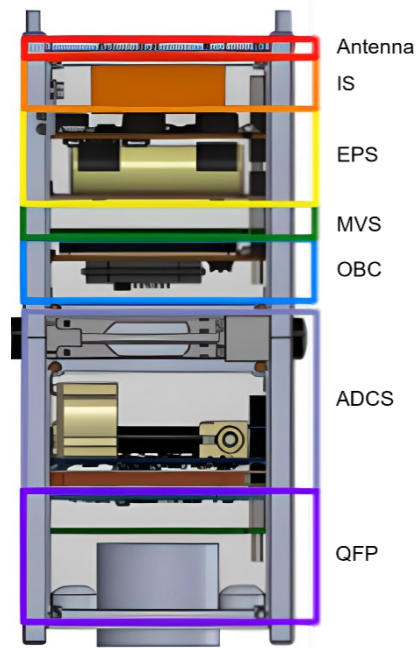
Figure 2 - Visual representation of the envelope of each subsystem.

1.2 The Microvibrations

Microvibrations, also known as low-level mechanical oscillations, are periodic disturbances that represent a critical phenomenon affecting various engineering systems and structures, particularly in the realm of aerospace and space technology [2]. These small-scale vibrations can have substantial implications on the performance, precision, and stability of sensitive devices, instruments, and, specially, optical platforms.

The significance of addressing microvibrations stems from their pervasive presence in space missions, satellite deployments, and scientific experiments. These mechanical disturbances can arise from a multitude of sources, such as moving parts, rotating components, mechanical interactions, thermal effects, and even electromagnetic forces. Despite their seemingly inconsequential nature, the cumulative impact of microvibrations can accumulate over time, potentially leading to misalignments, decreased accuracy, and compromised mission objectives [3].

In space missions, where extreme environmental conditions prevail, the challenge of managing microvibrations becomes particularly pronounced. Precision instruments, imaging systems, and communication payloads on spacecraft are susceptible to the detrimental effects of microvibrations, as even minute disturbances can disrupt data acquisition, hinder imaging resolutions, and hinder the performance of onboard sensors [4].

To address these challenges, a comprehensive understanding of the microvibration environment is essential. Thorough analysis, characterization and modelling of these mechanical oscillations facilitate the development of effective mitigation strategies, thus enabling more accurate measurements, reliable operations, and enhanced mission success rates.

For the purposes of this thesis, spacecraft microvibrations are small-amplitude mechanical vibrations due to dynamic interactions, usually in the range of $micro-g$ (μg) to $milli-g$ (mg), which typically occur at frequencies from a few Hz (tipically $0.1\ Hz$) up to a few hundred Hz (typically $1000\ Hz$).

1.2.1 *Microvibrations on CubeSat*

In recent years, the emergence of CubeSats and other miniaturized spacecraft has brought microvibrations to the forefront of research and development efforts [5]. These compact satellites, with their constrained dimensions and weight, necessitate innovative solutions to mitigate microvibrations and ensure optimal performance during their missions.

By analysing the microvibration environment, understanding its origins, and devising effective mitigation techniques, this research seeks to enhance the stability, precision, and overall success of future CubeSat missions.

Nowadays, even for CubeSats there is a demand for very accurate pointing, and it is possible to observe in literature [6] a growing trend as regards the mitigation of microvibrations. Poor satellite pointing stability can have a detrimental impact on the optical and imaging capabilities of satellite instruments. As shown in Figure 3, disturbances in the satellite orientation can lead to a noticeable reduction in imaging quality during an Earth observation mission. In the left section of the figure, one can observe the time-varying Line-of-Sight (LOS) pointing. Meanwhile, on the right side of Figure 3, there is a comparison of the relative quality of three distinct images. From left to right, these images depict: one captured in the presence of significant microvibration disturbances, another after implementing certain corrective measures to alleviate the effects of microvibrations, and finally, an image taken when the imager LOS remained undisturbed throughout the image acquisition period. These disturbances, often caused by microvibrations and other external factors, can disrupt data acquisition, hinder imaging resolutions, and compromise the overall performance of the satellite onboard sensors. Achieving precise and stable satellite pointing is crucial for obtaining accurate and reliable data for various scientific and operational purposes.
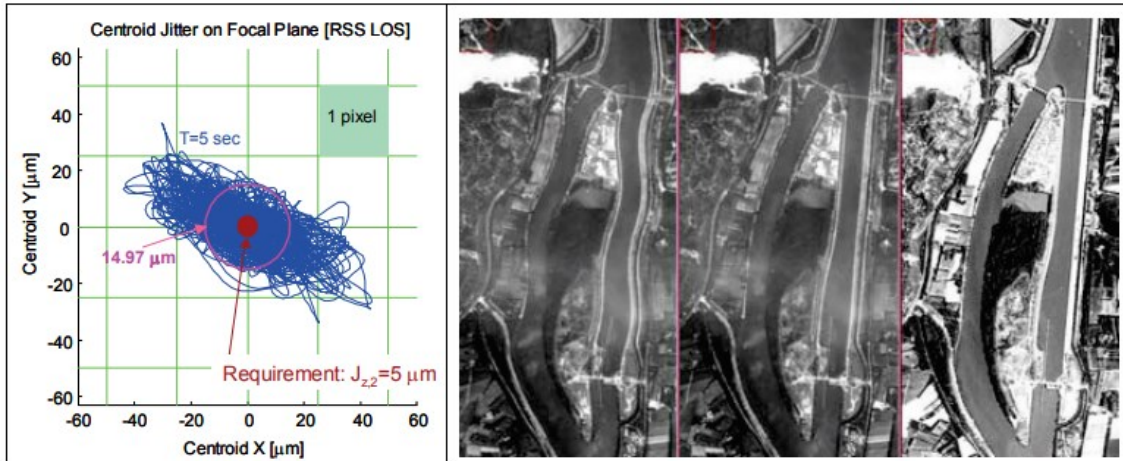
Figure 3 - Line of sight (LOS) pointing as a function of time (left) and resulting effects on image quality (right) [1].

Over the past decades, there has been a significant improvement in the sensor (angular) resolution of satellites, as depicted in Figure 4, driven by the increasing demand for high-resolution images. This evolution in payloads resolution has also led to a corresponding need for enhanced satellite pointing stability. As a consequence, the requirements for low disturbances on Earth observation and space astronomy satellites have become much more stringent. Precise and stable satellite pointing is now essential to meet the demands for accurate and high-quality data acquisition, especially for applications that rely on fine angular resolution [2].
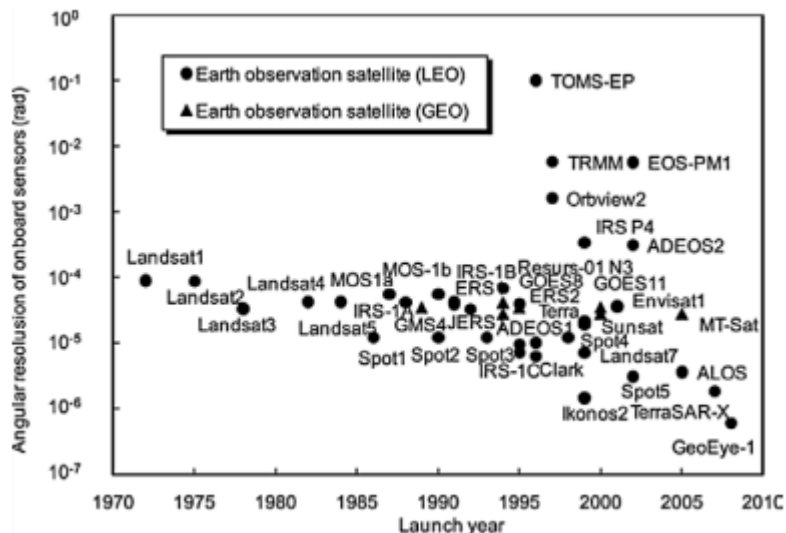
Figure 4 - Satellite imaging sensor resolutions move toward the one micro-radian over the years and drive the satellite pointing error in the same trend [4].

8

1.3 **Thesis Motivations**

This thesis was conducted within the framework of the AlbaSat project.
The primary objective of this thesis is to contribute to the advancement of satellite technology, particularly within the context of CubeSats, by addressing a critical aspect known as microvibrations. Specifically, this research aims to achieve the following:

1. *Development of a payload for nanosatellite applications*: the core purpose is to lay the groundwork for creating a satellite payload that can be integrated into a 2U CubeSat. This payload is designed with the capability of measuring microvibrations in the space environment.

2. *Enable in-situ data collection*: a critical point to emphasize is that microvibrations cannot be accurately assessed on Earth, as they are inherently influenced by gravitational forces. Consequently, in-situ measurements aboard the satellite are indispensable to unravel the intricate dynamics of them. On one hand, the in-orbit microvibrations measurement is an approach with the most dynamically representative configuration. On the other hand, results from the in-orbit measurements need to be treated with extreme care. Measurements in orbit also contain the vibratory signals from all other sources: cryocoolers, pointing mechanism of payloads and, also, interactions of multiple reaction wheels in operation simultaneously at different speeds. This interference is unavoidable given the operational constraints of the spacecraft such as its trajectory and scientific operations. Even in a dedicated listening campaign of the wheel, the operational wheel speed range during the campaign is limited. In addition, the dedicated in-orbit measurements require dedicated equipment and sensors which lead to an increase of the spacecraft cost. The in-orbit measurements mainly aim to confirm the predicted microvibrations performance or obtain statistics of wheel microvibrations performance in flight.

3. *Support for future space missions*: the research aspires to offer a robust and reliable design for a microvibrations sensor. This design not only serves as a valuable tool for the AlbaSat project but also lays the groundwork for potential use in upcoming space missions. By addressing the issue of microvibrations, this work contributes to enhancing the performance and longevity of future satellite systems.

9

4. *Measure Momentum Wheel-related microvibrations*: a specific focus is directed toward measuring microvibrations stemming from MW, a prominent source of such disturbances. The goal is to develop an accelerometer-based sensor system that can effectively quantify these microvibrations, thereby aiding in their characterization and control.

In summary, this thesis endeavours to advance satellite technology by developing a novel payload for CubeSats, enabling in-situ microvibration data collection. It aims to facilitate future space missions, especially those grappling with microvibration-related challenges, by providing a practical and reliable solution for characterizing and mitigating these disturbances, particularly those generated by MW.

1.4 **Thesis Outline**

In this section, a flow diagram representing the thesis structure is shown in Figure 5. A concise summary of the content of each chapter can be found below the figure.
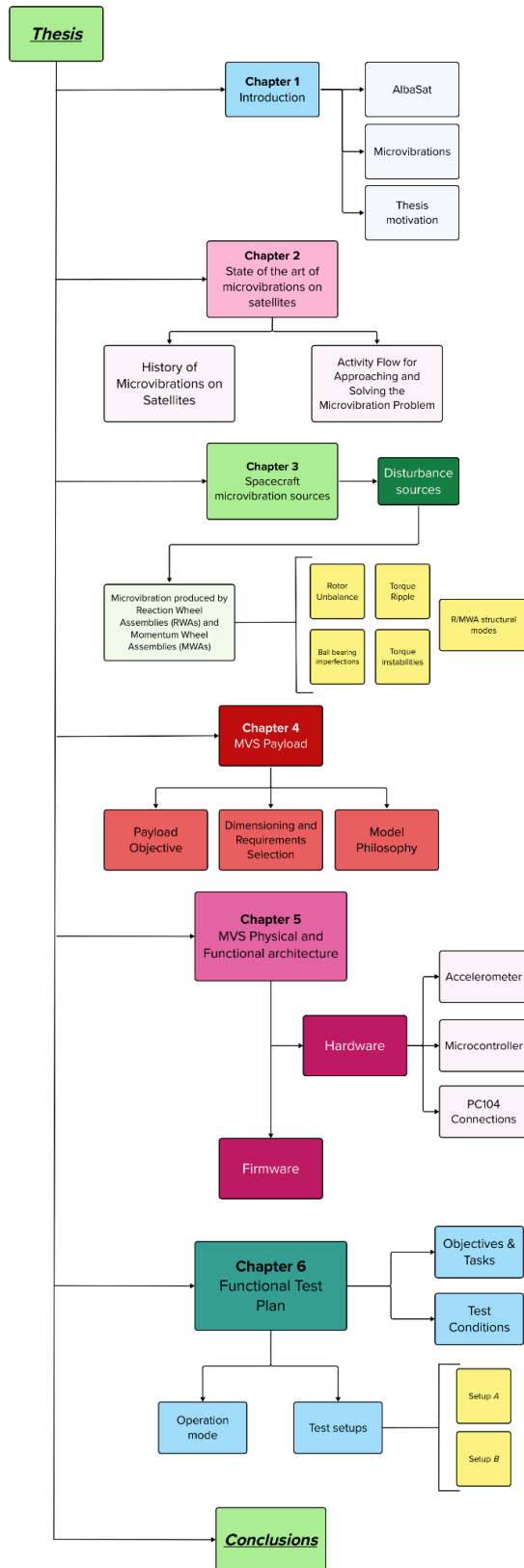
Figure 5 - Overall thesis structure.

Chapter 1 provides an overview of the context in which this thesis is developed.

Chapter 2 comprises a literature review of space missions that have addressed the issue of microvibrations and related problems. Furthermore, it also provides an activity flow for approaching and mitigate the microvibration problem.

Chapter 3 presents a study of the microvibrational environment of a satellite, analysing in detail the microvibrations produced by MED. Moreover, microvibration sources are discussed in detail to pave the way for the following chapters.

Chapter 4 contains the definition of the objectives and requirements of the microvibration sensor developed as a payload for the AlbaSat mission. It also collects the model philosophy adopted in the development of the sensor.

Chapter 5 first presents the physical architecture of the MVS payload. Subsequently, the selected COTS components and the electrical diagram of the developed PC104 board are illustrated. Finally, the system firmware is presented.

Chapter 6 presents the functional test plan for the MVS. Functional tests are of paramount importance for the payload overall performance and reliability. To ensure the system meets the required standards and achieves a Technology Readiness Level (TRL) of 4, a comprehensive plan for functional testing is meticulously developed, adhering to European standards and guidelines.

The final chapter contains the conclusions and presents the implication of the work performed as well as future works.

Chapter 2
STATE OF THE ART OF MICROVIBRATIONS ON SATELLITES

This chapter aims to describe microvibrations, with a focus on the state-of-the-art methods currently used to characterize the disturbances generated by on-board mechanisms and how the internal dynamics of the microvibration sources are implemented to fully represent the interaction with a spacecraft structure in a microvibration environment.

2.1 History of Microvibrations on Satellites

In the formulation of the next generation of space and Earth science missions, there is a constant trend by both the National Aeronautics and Space Administration (NASA) and the ESA to push towards higher-performing payloads and instruments. Currently, high-performance optical payloads with vibration-sensitive scientific instruments are planned for spaceflight missions by both NASA and ESA. Another challenging task is the stabilization of optical communications payloads, and control of microvibrations is essential for this aim [3]. These missions often have demanding goals that require precise observatory design. It must ensure accurate spacecraft pointing and stable accommodations for scientific instruments despite dynamic interactions. The term "observatory" here includes both the spacecraft bus and the optical payload. These instrument accommodations, in particular, frequently requires extremely strict, arcsecond ($arcsec$) level or less, constraints on attitude and attitude rate stability. In addition, they require to control a wide frequency range that often the Attitude Control System (ACS) cannot span.

Looking back one can observe that both NASA and ESA, together with their industry partners, have a long, technically rich, and impressive history of successfully addressing the spacecraft engineering problems associated with managing undesirable dynamic interactions that perturb an observatory payload instrument pointing/pointing stability

(aka "jitter"). This microvibration engineering history can be traced as far back as the mid-1970s when NASA was studying architectural concepts for the Large Space Telescope (LST), also known as Hubble Space Telescope (HST).

An overview of spacecraft microvibration engineering over the last four decades is provided in [3] - [4].

The HST project objectives primarily served as the impetus for the development of technologies to successfully address microvibrations in satellite engineering, which began roughly in the early 1980s. Since then, the interest in microvibration analysis has led to the development of sophisticated optical instruments that demand extremely stringent pointing requirements and platform stability. These are challenging for the control and mitigation of microvibrations on-board satellites.

2.1.1 *Hubble Space Telescope*

The HST observatory, the first of NASA Great Observatories, was deployed the 25 April 1990 from the Space Shuttle Orbiter Discovery into a $614\ km$ Earth orbit.

The HST was designed to achieve stringent LOS pointing stability while observing celestial objects for long exposures. At the highest-level, the telescope pointing requirement was specified at $< 7\ milli-arcsec\ (mas)$ over a $24-hour$ period. This ground-breaking space observatory Pointing Control System (PCS) was specifically created to stabilize the Solar Array (SA) and linked vehicle-telescope bending modes. Pre-launch jitter study and prediction required significant resources, a large portion of which were spent to disturbance source modelling and characterization to understand the potential effects on the telescope LOS jitter. The original HST jitter studies were focused on anticipating disturbance effects on a LOS central pointing vector as well as minimizing other known image-distorting effects. These studies were based on prior methodologies employed on secret satellites. The principal structural mode frequencies and the frequency of the maximal active control bandwidth should be kept far apart throughout design. Structural Dynamics Test Vehicle (SDTV) in full scale was also created by the NASA. The SDTV was a medium-fidelity demonstrator built with structural elements that would be used in flight. For each of the five flight-certified RWs used in the PCS, an unprecedented set of high-sensitivity induced vibration data was also collected. In order to completely analyse the telescope susceptibility to microvibration disturbances, a

Dynamic Interaction Test (DIT) of the fully-up HST observatory was carried out in the test facility of NASA while it was suspended by bungee-cord-like devices to off-load gravity. However, problems with the HST capacity to accomplish its job were discovered not long after it was launched into orbit. Not only was an optical imperfection in the telescope main mirror detected, but a review of real-time flight telemetry data revealed that the HST was suffering surprisingly huge disruptions, which were particularly noticeable when the spacecraft entered or left the Earth shadow. A focused investigation into the nature of the observed pointing disturbances revealed that the SAs were the source of the disturbance. The thermal/mechanical energy in the array was being stored and released in such a way that it excited the arrays fundamental modes. The PCS was initially supposed to adjust for these unanticipated pointing perturbations caused by the Sunrise/Sunset 'thermal snap' SA disturbances, but it was unable to do so. As soon as the problem was detected, efforts were launched to modify the PCS in order to mitigate the disturbances. A successful reconfiguration of the flight computer and a redesign of the control system, combined with a minor adjustment of the original performance requirements, resulted in a controller that fulfilled the new parameters the majority of the time. As a result of the PCS redesign efforts, a lot of flight data relevant to the control system performance was obtained. As more was discovered about the spacecraft on-orbit dynamic behaviour, simulation models were improved. As a result, several test campaigns were carried out to quantify the projected on-orbit disturbances generated by the micro turbo-machinery. In order to verify compliance with the HST 7 *mas* jitter criterion, this testing delivered validated inputs to a flexible body dynamic simulation [3].

2.1.2 *Solar and Heliospheric Observatory*

The Solar and Heliospheric Observatory (SOHO) spacecraft, a collaboration between ESA and NASA, was launched into a halo orbit around the Lagrange Point L1 in December 1995. SOHO has been in space for over 20 years and was originally intended to be a two-year mission. Sending SOHO to Lagrange point L1 has enabled scientists to investigate several elements of the Sun behaviour using photos captured by the multiple scientific equipment that comprise its payload. The SOHO spacecraft was designed to provide LOS stability below the picture pixel or resolution requirements of the science equipment. This translated into short-term stability requirements of less than 1 *arcsec*

for the majority of the payload equipment. The performance goal was to limit the peak dynamic jitter between 0.3 and 0.5 $arcsec$. The SOHO team was thus challenged with a difficult microvibration challenge. This was especially true considering the low heritage for dealing with such a sophisticated observatory in the early-mid 1990s [3]. The SOHO jitter assessment research was designed to be a well-balanced, pragmatic, and logical combination of analysis and testing that would serve as the foundation for the models and jitter prediction simulations. To facilitate the development of a verified spacecraft structural Finite Element Model (FEM), a set of modal survey experiments on observatory substructures were performed. To describe the individual disturbance causes, component level testing was undertaken. The RWs, which are commonly used in ACSs, as well as a number of scanning, focusing, and rolling mechanisms linked with individual science instruments, were recognized as the most significant disturbances. A SOHO jitter prediction analysis was carried out to assist the project team in determining the appropriate pointing/jitter error budget and adequate requirements flow down. In February 1995, a representative configuration of the flight model SOHO spacecraft underwent a final pre-launch jitter verification DIT test. The primary goal of this test, as with most full-fledged observatory DITs, was to make experimental measurements of the jitter caused on the most sensitive instruments by sequential activation of individual "real-world" disturbance sources. The SOHO jitter team was especially keen in acquiring LOS jitter data at frequencies over 150 Hz, the frequency threshold beyond which the team considered the validity of the spacecraft FEM was uncertain. The SOHO spacecraft was suspended in the test facility using a compliant bungee-cordlike suspension mechanism to minimize gravity effects and achieve the free-free boundary conditions representative of the flight condition. The jitter test data gathered during this suspended DIT matched well with the analytical expectations. When the in-flight microvibration data was compared to the pre-launch analytical jitter projections and ground test findings, the jitter levels were found to be generally positive. However, the in-flight LOS jitter in several instruments was found to be substantially lower than expected by the microvibration analysis. Investigations into the differences found that the reason of the overpredictions was either the application of worst-case analytical assumptions that were not observed in flight or less dynamic coupling than predicted in the pre-launch jitter study. This SOHO experience emphasizes the significance of comprehending the observatory disturbance

spectrum (from diverse sources) and its impact on important payload parts. Understanding the impacts on pointing stability and establishing whether any local payload structures are aroused by the disturbances is sometimes discovered only through testing.

Looking back, the SOHO jitter assessment experience appears to have been a very comprehensive and well-constructed campaign from which both ESA and NASA drew some important lessons learned to apply to their future complex and demanding mission applications.

2.1.3 *James Webb Space Telescope*

James Webb Space Telescope (JWST) employs six RWs to generate control torques in order to position the observatory, while three-star trackers and six gyroscopes conduct ACS sensing operations. This allows for adequate coarse pointing to maintain the SA aimed towards the Sun and the High Gain Antenna (HGA) directed toward Earth. Finer pointing is required to capture photos and spectra of celestial targets. For fine pointing control during observations, the ACS communicates with the Fine Guidance Sensor (FGS) in the Integrated Science Instrument Module (ISIM) and the telescope Fine Steering Mirror (FSM). As described in [7], the JWST requires 3.7 mas for telescope line of sight motion. JWST features a two-stage passive vibration isolation technology to reduce higher frequency $(> 2.0\ Hz)$ microvibration disturbances caused by RW static and dynamic imbalances, as well as bearing run-out. Stage 1 isolation consists of 7.0 Hz RW isolators positioned between each RW and the spacecraft bus, whereas Stage 2 isolation consists of a 1.0 Hz tower isolator located between the spacecraft bus and the observatory Optical Telescope Element (OTE). An additional bias control loop that governs RW speed operation near a set speed in the null-space of the RW cluster is used to bias the RWs to 2700 rpm. This RW speed bias set point is required to keep RW speeds within an appropriate speed range of 15 Hz to 75 Hz in order to avoid exciting structural vibrations that could cause LOS jitter.

2.1.4 *Solar-C*

Solar-C is the next generation of Japanese solar physics satellite, developed in conjunction with the US and the UK, and follows the earlier Hinode (Solar-B) solar mission, which provided unprecedentedly high-quality images of the Sun. The satellite

carried telescopes with resolutions less than $1/100,000 \ degree$. A systematic approach was developed to achieve this performance, which included sophisticated microvibration transmissibility tests (from the source of microvibrations to the telescopes) as well as accurate measurements of the disturbance levels [3].

2.1.5 *BepiColombo*

The ESA mission to Mercury, BepiColombo, is a collaboration between ESA and the Japan Aerospace Exploration Agency (JAXA). BepiColombo is the fifth pillar of the ESA Cosmic Vision Scientific Program. The impacts of microvibrations caused by the RWs, SA, and HGA drive mechanisms may degrade the functioning of the on-board instruments during scientific observation periods. Because most sensors require constant and highly accurate Nadir-pointing, the spacecraft pointing stability is strictly enforced. Line-of-sight stability must be greater than $1\ arcsec$ per $second$ and greater than $0.1\ arcsec$ per $msec$. The rotation requirement around the LOS is more lenient ($20\ arcsec$ per $second$ and $2\ arcsec$ each $msec$). During the two years of science operations orbiting Mercury, these pointing stability performance requirements must be met 95 % of the time. ESA conducted an analytical microvibrations study to confirm that the above instrument stability pointing requirements are met 95 % of the time in the face of RW disturbances, HGA (which continuously tracks Earth during science observation periods) disturbances, and SA disturbances. The BepiColombo jitter team performed a verification campaign with the 95 % probabilistic stability criterion. A Monte Carlo simulation approach was rejected because it would have necessitated individual spacecraft FEMs for each HGA and SA orientation examined. The pointing stability requirements were regarded as temporal, which means that they must be met 95 % of the time over the $2-year$ mission while considering the whole population of observatory configurations, as well as wheel speeds and HGA/SA drive mechanism speeds. Unfortunately, an a priori worst-case situation, i.e., the worst-case combination of HGA and SA orientations combined with worst-case mechanisms/wheel speeds, could not be identified. As a result, the technique taken was to generate confidence intervals for the entire population based on data derived from seven specific cases studied. As an aside, according to [8], the Kistler table wheel disturbance characterization testing was carried out using an "old" RW that was believed to be operationally indicative of the BepiColombo flight wheels. The Kistler test data on this particular RW, on the other hand, exhibited abnormally large axial and radial disturbance forces. An inquiry revealed that the "old" RW utilized for characterization testing may have had a faulty bearing, resulting in disturbance levels that were not actually typical of the flight wheels. To generate a more accurate set of disturbance data with which to validate the analytical RW models,

the Kistler testing was repeated with an Engineering Qualification Model (EQM) of the BepiColombo wheel. This particular experience emphasizes the vital importance of performing disturbance characterizations testing with component test articles (e.g., RWs) that correctly replicate the dynamical behaviours of the flight hardware. Otherwise, there is the risk of wasting test and analysis time and resources attempting to reconcile abnormal disturbance data. To obtain the most accurate representation, the real flight hardware shall be tested.

2.1.6 *SPOT-4*

SPOT-4 was launched in 1998 and remained operational until 2013. It is a second-generation SPOT-series satellite of Centre National d'Études Spatiales (CNES).

PASTEC (PASsager TEChnologique SPOT 4) was the most critical payload on board the satellite in terms of microvibrations. It was a passenger payload designed to explore the orbital environment. It carried two instruments, MEDY and MicroMEDY, whose goal was to measure satellite dynamics and characterize in-flight vibration and microvibration environments with a resolution of up to $10\ g$. In-orbit data revealed that resonance frequencies are slightly higher than those observed on the ground, but damping ratios are lower, especially in the range of the first global modes.

The SPOT family, OLYMPUS, GOCE, Solar Dynamics Observatory (SDO), Skybox, GeoEye, and WorldView exhibit difficult high-sensitive vibration instrumentation [3].

2.2 **Activity Flow for Approaching and Mitigate the Microvibration Problem**

Typically, the design and development of an appropriate level of microvibration control to suppress and/or isolate onboard disturbances necessitate thorough analysis, modelling, simulation, and comprehensive ground-based testing at both the component and subsystem levels (such as disturbance source characterization tests) as well as at the integrated system level to assess end-to-end performance. In many instances, post-launch flight tests are also conducted to validate the adequacy of pre-launch modelling and to update performance predictions based on the analysis of data collected in the actual operational environment of the mission.

Before initiating the design process, a jitter analyst should acknowledge and comprehend that not all observatory projects require the same level of concern while addressing the microvibration issue. While the design process is inherently iterative, a starting point is essential.

Table 1 summarizes the 'rules of thumb' and illustrates which microvibration designs are already known, which design drive the overall system, which designs represent the state of the art, and, lastly, which designs pose development risk as they are beyond the current state of the art.

Table 1 - Rules of Thumb for Initiating and Approaching New Microvibration Designs

Case	Stability/ Accuracy/ Reconstruction ($arc-seconds, 1-\sigma$)	Keys/Drivers to Microvibration Designs					
		Architecture	Model/ Simulation	ACS	Structural	Instrument Control	Testing
1	100 + +	ACS	Low Fidelity	HW	Low Freq modal	Functional	Interfaces @I&T
2	10 → 100	Thermal & ACS	Low Freq & Fidelity	HW, CSI	Mid Freq Modal	Functional	Subsystem V&V @ I&T
3	0.1 → 10	Thermal, ACS & Jitter	Med. Freq & Fidelity, @PDR	HW, CSI	Mid Freq Modal + Asymptotes	Functional + Compensation	Subsystem V&V @ I&T
4	0.01 → 0.1	Thermal, ACS & Jitter	High Freq & Fidelity, @ PDR	HW, CSI Operational	High Freq Modal + Asymptotes	Functional + Compensation	Subsystem @ I&T, Component @ CDR
5	$1e^{-3} \rightarrow 1e^{-2}$	Calibration Thermal, ACS & Jitter	High Freq & Fidelity, @ SRR	HW, CSI Operational, algorithms	High Freq Modal + Tailoring	Functional + distributed Control	System @ I&T, Subsystem @ CDR
6	$1e^{-4} \rightarrow 1e^{-3}$	Calibration Thermal, ACS & Jitter	High Freq & Fidelity, @ SRR	HW, CSI Operational, algorithms	High Freq Modal + Tailoring	Functional + distributed Control	System @ I&T, Subsystem @ CDR
Known Design		**Drives System**		**State of the Art**		**Beyond State of the Art → Risk**	

Chapter 3
SPACECRAFT MICROVIBRATION SOURCES

To gain a deeper insight into the microvibration levels that impact a spacecraft, it is vital to thoroughly examine all potential sources of disturbances. Employing a logical breakdown, as outlined in [1], enables the categorization of these sources into two main groups: external and internal disturbances. Among the onboard disturbances, this thesis focuses on the disturbances caused by MED.

3.1 Disturbance Sources

The attributes of potential sources of disturbance can be characterized in either the time or frequency domain, or even through a combination of both. These sources can be categorized into external (or natural) and internal disruptors.

3.1.1 *External Events*

Space is a challenging environment for spacecraft attitude control. External disturbances are regarded unimportant in the context of microvibrations since the ADCS compensates for them to a large extent.

External (or natural) occurrences hold significant importance primarily as potential disruptions to the micro-gravity environment. They stem from:

- Micro-meteoroids and debris impacts;
- Atmospheric drag;
- Earth gravity field gradient;
- Earth magnetic field;
- Solar flux & Earth albedo;
- Eclipse entry & exit.

3.1.2 *Internal Events*

Spacecraft subsystems can cause vibrations on spacecraft, which are then transferred to the pointing-sensitive payload through the structure. Because of the number of subsystems, their reciprocal interaction, and their broadband frequency microvibrations region, this disturbance category is the most significant for this investigation. The most crucial subsystems, intuitively, are those with mechanical moving parts, such as R/MWs, cryo-coolers, rockets, solar arrays, and antenna motors. Other events, such as a clank or a structural rapid stress release, may occur, adding further vibrations.

Then, internal events arise from:

- Propulsion subsystem;
- Avionics subsystem;
- Electrical power subsystem (EPS);
- Radio frequency (RFS) / telemetry & telecommand subsystem;
- Thermal control subsystem (TCS);
- Structure subsystem.

Table 2 lists the major internal disturbances and their signal characteristics.

Table 2 - Potential classification of microvibration disturbance sources.

Source	Harmonic	Transient
Reaction Wheel	⊠	
Control Momentum Gyros	⊠	
Gyroscopes	⊠	
Solar array drive mechanism	(⊠)	⊠
Antenna pointing mechanisms		⊠
Mirror scan mechanisms		⊠
Cryogenic coolers	⊠	
Micro-thrusters, gas flow regulators		⊠
Latch valve		⊠
Heat pipe	⊠	
Relay, RF switch	⊠	
Sudden stress release	⊠	
Clank phenomena (e.g., electromagnetic force effects)	⊠	

Both external and internal events can be further categorized by considering the source element, the nature of the physical event, the physics of the disruptor, and the type of signal.

3.2 Microvibrations produced by Reaction Wheel Assemblies (RWAs) and Momentum Wheel Assemblies (MWAs)

The disturbances caused by RWAs and MWAs were often seen as the most significant, and hence they have garnered the majority of attention over the years [3] [9] [10]. As a result, a relevant literature evaluation is devoted to these mechanisms in this thesis. RWA fundamentals and microvibration analysis approaches are discussed. Previous RWAs theoretical models and investigative methodologies are described.

Several researches have been conducted to study the disturbances caused by R/MWA. Masterson et al. completed extensive study on RWA in the domain of empirical and analytical disturbance models, concluding that mass imbalances are the most significant source of the disturbances [10]. Furthermore, Elias and Miller proposed a coupled RWA

disturbance analysis method based on dynamic mass measurement techniques [11], and Shigemune and Yoshiaki established a method to measure lower frequency disturbances induced by R/MWA [12], which are traditionally difficult to detect, revealing that the R/MWA internal dynamics are closely related to the disturbances. Zhou et al. devised a low-cost measurement device comprised of a seismic mass and two high-sensitivity accelerometers, which was used to test the microvibrations produced by cantilevered momentum wheel assemblies [13]. Most scientific articles published either focus on the disturbance caused by mass imbalance as the primary source of disturbance [10] [13] or individually investigate the disturbance causes.

A MWA (RWA) primarily consists of a flywheel (a rotating mass) which is typically supported by ball bearings and driven by a brushless Direct Current (DC) motor as depicted in Figure 6.
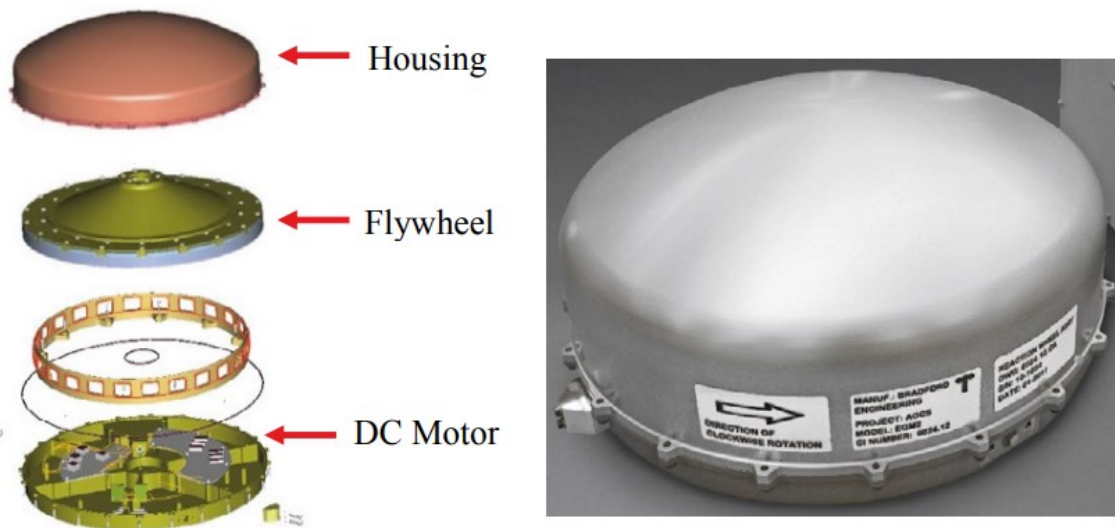
Figure 6 - Sketch of a Reaction Wheel Assembly [2].

The operating principle of a MW (or a RW) on a spacecraft is based on the conservation of momentum. A wheel provides momentum to the spacecraft by keeping the flywheel rotating at a constant speed. A response torque is produced by altering the spinning speed of the flywheel. A spacecraft moving or pointing capability is provided by this response torque.

Common flywheel configurations of a R/MWA are either symmetrical (flywheel at mid-span of the shaft) or cantilevered (flywheel at one end of the shaft), as illustrated in Figure 7.
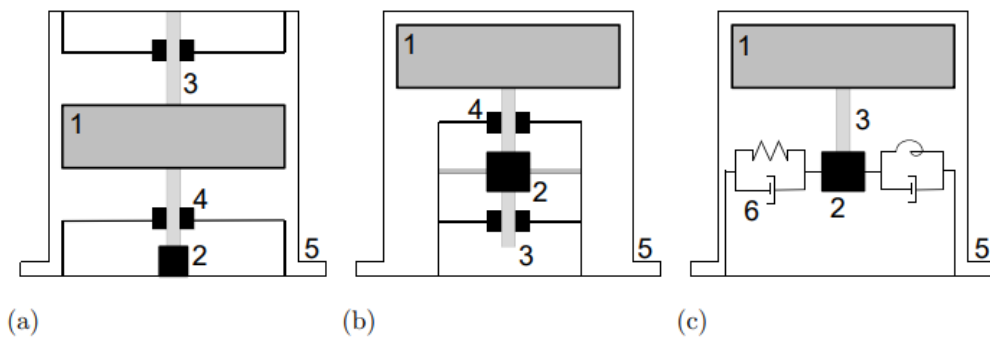
Figure 7 - Schematic cross-sectional view of R/MWA components and configurations: 1-flywheel, 2-motor, 3-rigid shaft, 4-ball bearings, 5-housing, 6-flexible components; (a) symmetric; (b) cantilever with rigid connection and (c) cantilever with flexible connection

It should be noted that it is common practice to put three or four R/MWAs on the spacecraft, and thus their relative position may influence the vibrations delivered to the spacecraft. Microvibrations caused by a single R/MWA are studied in this thesis.

The microvibrations induced by a R/MWA are classified as harmonic and continuous occurring at well-defined ratios of the angular frequency of a spinning flywheel [4].

According with [2], the following types are present:

- *Microvibrations* are periodic micro-disturbances which manifest themselves as three forces (F_X, F_Y, F_Z) and three torques (M_X, M_Y, M_Z). They are generated by the reaction wheel during its operations. The three main sources are:
  - Rotor imbalances: due to a residual uneven distribution of mass around the flywheel axis of rotation;

27

- Ball bearing imperfections: imperfections (not surface roughness) of bearing elements such as balls, raceways, and cages cause vibrations once they are in the contact zone of the bearing;
- Torque ripple: the torque ripples are caused by high frequency phase switching of the stator (coils) as inherent from the principle of a DC brushless motor.

- *Torque instabilities* are random or transient micro-disturbance of torque signal (M_Z). The torque instabilities occur due to the lubricant dynamics and the misbehaviour of bearings.

In general, microvibrations are analysed in the frequency domain, as they can be modelled as discrete harmonics (sine functions) with amplitudes proportional to the wheel speed squared. Any signal whose frequency shows a linear dependence on the wheel speed is called an engine order.

A harmonic number, also known as a harmonic order, is defined as the ratio of frequencies to wheel speed. This is especially useful because many types of microvibrations (such as imbalance, which occurs once per revolution and thus has harmonic order 1) have the same harmonic order across their entire speed range, whereas frequencies change linearly with speed.

Then, alternatively, microvibrations can be transformed into the order domain, where the frequencies are normalized by dividing them by the wheel speed.

Waterfall plots are a popular approach to display microvibrations, in which the amplitudes of the vibrations are 3D plotted in frequency or order domain, with frequencies/orders and speed (rpm) in the x and y axes, respectively. This approach facilitates the comprehensive observation of the entire frequency spectrum within the operational range of the component.

Regarding disturbances arising from a mechanical system, the vibrations that exhibit a linear correlation with rotational speed are referred to as *fundamentals*. These can be observed on waterfall diagrams as diagonal lines originating from the baseline. This process yields vertical lines representing harmonics beyond the first fundamental.
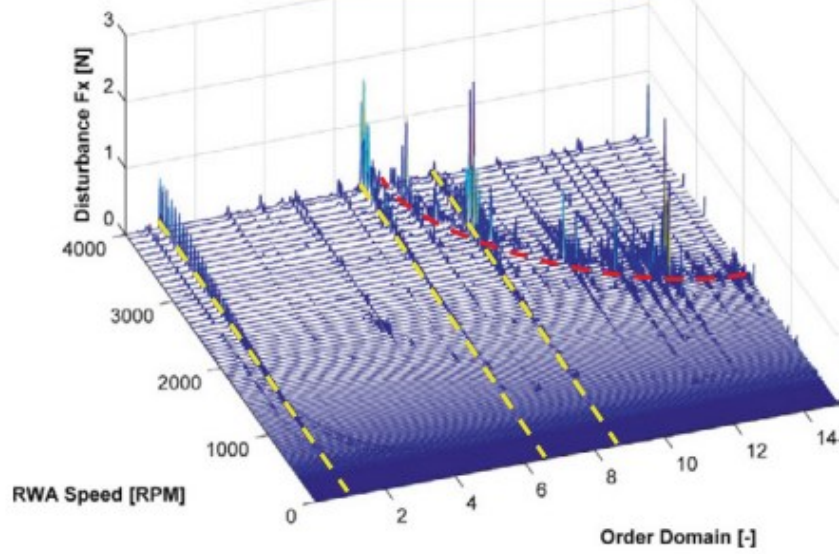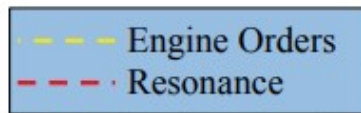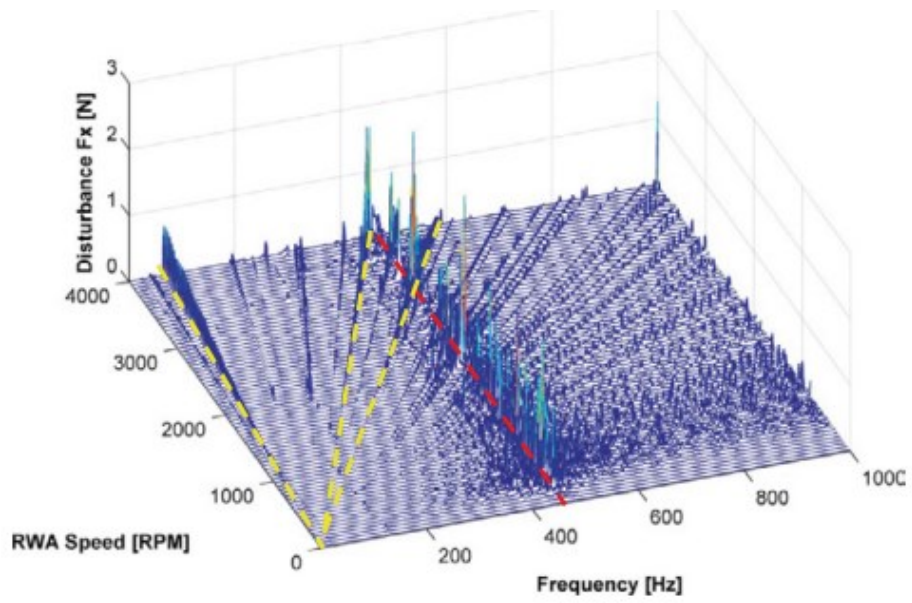
Figure 8 - Some example of engine orders and one resonance visualized in the frequency domain (top) and the order domain (bottom) [2].

In the case of a linear system, the total microvibration sources result from superimposing all engine orders. Because the frequencies of the microvibration sources fluctuate with speed, they interact with the structural modes of the wheel at different speeds (Figure 8). The interaction results in the amplification of the microvibration sources. This microvibration is subsequently relayed to the satellite wheel interface. Although the amplification effect has no detrimental effect on wheel operation, the generated microvibrations are frequently the strongest in the microvibration spectra.

Typically, the primary fundamental corresponds to the disturbance with the highest amplitude.

The disturbances of the previously listed reaction wheel are further analysed in the following. Specifically, the imbalance of the rotating mass can be divided into two phenomena, one static and the other dynamic. The main difference is that, respectively, the former generates forces in the plane of rotation while the latter generates moments outside the plane of rotation. Microvibrations due to imbalance, as a matter of fact, are often the greatest reaction wheel disturbances, while those due to bearing imperfections or torque ripple are usually very close to the noise floor.

3.2.1 *Rotor Imbalance*

The major cause of microvibrations in a reaction wheel is its imbalance [5]. This is an issue that emerges during the wheel fabrication process. Due to the inherent limitations of manufacturing, achieving perfect mass distribution in a component is unattainable. This results in an eccentricity or offset between the main axis of inertia (where the mass centre resides) and the wheel rotation axis. Consequently, imbalance is an inevitable attribute of the wheel manufacturing, present albeit minimally in any system involving a motor, shaft, and flywheel. This characteristic can only be mitigated by enhancing the uniformity of the flywheel mass distribution but not completely eliminated. A more formal explanation of imbalance will follow. A common reference frame established for a R/MW involves x and y axes situated in the wheel rotation plane and the z axis coinciding with the rotation axis. Consequently, as previously mentioned, the microvibrations produced by the wheel can generally be broken down into three force components (F_X, F_Y, F_Z) and three moment components, or torques (M_X, M_Y, M_Z).

3.2.1.1 Static Imbalance

Static imbalance arises due to an uneven dispersion of mass in the rotation plane of the rotor. This imbalance causes a displacement between the axis of inertia and the axis of rotation, illustrated in Figure 9. It is important to note that even in cases of pure static imbalance, the axis of inertia and the axis of rotation remain parallel to each other.
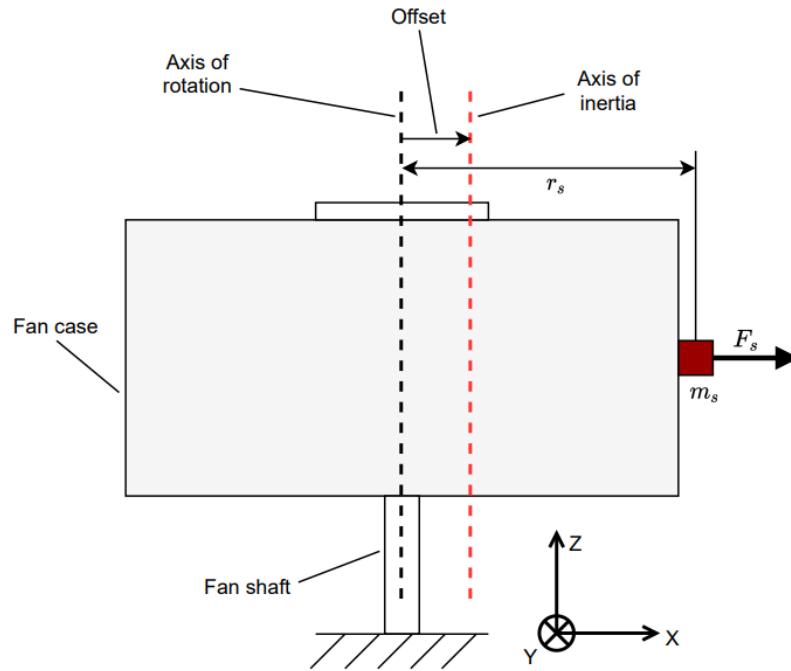
Figure 9 - Static Imbalance [5].

From a physical point of view, this can be expressed as:

$$U_s = m_s \cdot r_s \quad [g \cdot cm]$$ (1)

where U_s is the static imbalance, m_s is the mass of the static imbalance and r_s is the distance between the rotating axes and the mass m_s. The unit of static imbalance for reaction wheels is usually expressed in $g \cdot cm$ because its magnitude is small.

When the wheel starts working, U_S becomes a centrifugal force which appears once per spin and force such reason its harmonic is of first order in the frequency domain:

$$F_s = U_s \cdot \Omega^2$$ (2)

where Ω is the wheel rotation speed. This force is sensed during a microvibration test as radial forces F_X and F_Y . Because the static imbalance induced force F_S repeats every rotation of the rotor, the static imbalance has the order $h = 1$ in the order domain.

3.2.1.2 Dynamic Imbalance

A dynamic imbalance, instead, is caused by an uneven distribution of mass in planes parallel to the plane of rotation. This results in an angle between axis of rotation and axis of inertia.
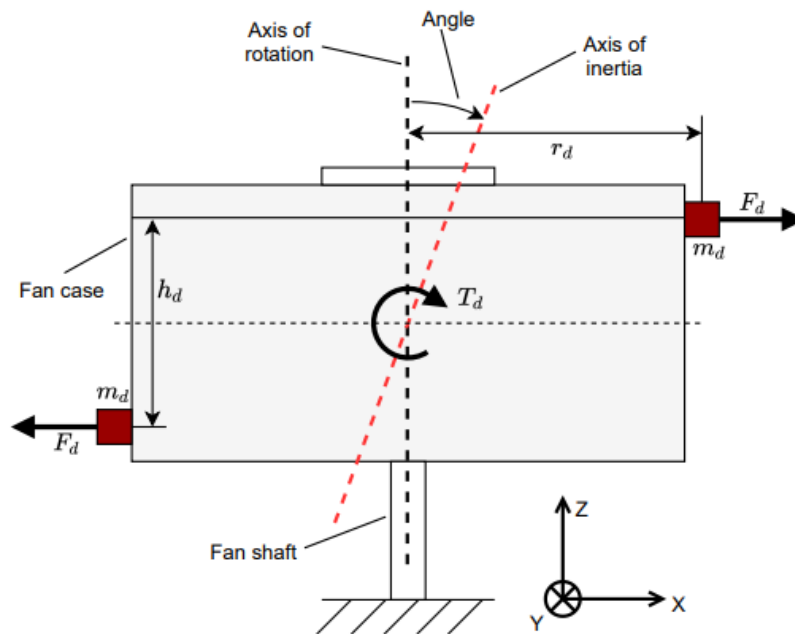
Figure 10 - Dynamic Imbalance [5].

32

The quantification of dynamic imbalance is given by the equation:

$$U_d = 2 \cdot m_d \cdot r_d \cdot h_d \quad [g \cdot cm^2] \tag{3}$$

where m_d represents the mass associated with dynamic imbalance, r_d stands for the radius between the axis of rotation and the dynamic imbalance mass and h_d is the distance between the two dynamic imbalance masses. When the rotor is in motion, the dynamic imbalance leads to a pair of centrifugal forces that generate a lateral moment:

$$M_d = U_d \cdot \Omega^2 \tag{4}$$

As the pair of centrifugal forces, F_d cancel each other out, only the lateral moment stemming from dynamic imbalance is observed during microvibration testing, manifesting as moments M_X and M_Y. As for the static imbalance, the induced moment from dynamic imbalance is detected at its maximum level once per revolution. Consequently, dynamic imbalance holds an order of $h = 1$ in the order domain.

3.2.2 Ball Bearing Imperfections

Vibrations in ball bearings can be divided into three types based on their source [14]:

1. Manufacturing: manufacturing imperfections can be further divided into two subcategories:

    o *Geometrical imperfection*: is referred to as local irregularities on the surface of bearing parts. Once an imperfection enters the contact zone of two bearing parts, an impulse force is generated. The repetition of the impulse forces causes vibration.

    o *Waviness*: deviation of the shape of the balls from an exactly spherical shape (out-of-roundness).

    In reaction wheel applications, one should anticipate solely imperfections and waviness. This is due to the fact that during on-ground operation, the reaction wheel bearings experience minimal loading, with a rotor mass, of up to $60\,N$, whereas the bearing load capacity exceeds $2000\,N$. As a result, prominent bearing failure modes like wear and spalling, categorized as bearing faults, are irrelevant for reaction wheels.

    Furthermore, within the context of this thesis, the term "bearing anomaly" pertains to exceptional or atypical characteristics of a bearing component. It is important to note that "bearing anomaly" does not signify bearing faults.

2. <u>Structure</u>: under the excitement induced by additional defects, the bearing and surrounding structure can reverberate. This is referred to as structural vibration.

3. <u>Handling</u>: vibrations caused by contamination and imperfections arising during the assembly process or verification tests are considered sources of vibration due to handling.

    o   Imperfections can originate not only from manufacturing but also from mechanical impacts during verification tests, such as random vibration and shock tests.

    o   Contaminations may lead to vibrations that change over time due to the mobility of the contaminants moving to various bearing parts. However, it is unlikely for contaminations to occur in reaction wheels due to stringent handling and inspection requirements.

All these imperfections have distinct harmonic orders that can be deduced from a kinematic bearing model. These orders are computed as outlined in Table 3, considering the absence of slippage between bearing components and focusing on imperfections within individual bearing parts (without the interplay of multiple imperfections).
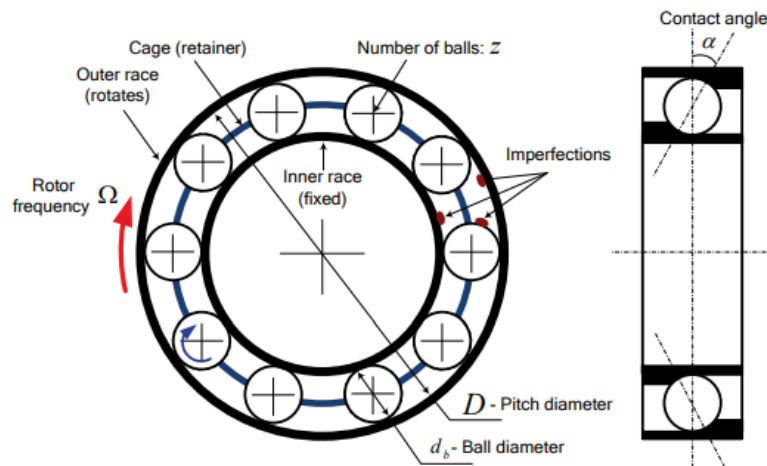
Figure 11 - A kinematic model for a ball bearing in reaction wheels [2].

Table 3 - Engine orders of a single imperfection on bearing parts in reaction wheels where the inner race is fixed.

Single Imperfection	Engine order
Inner Race Imperfection	$H_{IRI} = \dfrac{z}{2}\left(1 + \dfrac{d_b}{D}\cos(\alpha)\right)$
Outer Race Imperfection	$H_{ORI} = \dfrac{z}{2}\left(1 - \dfrac{d_b}{D}\cos(\alpha)\right)$
Cage Rotation Imperfection	$H_{CR} = \dfrac{1}{2}\left(1 + \dfrac{d_b}{D}\cos(\alpha)\right)$
Ball Imperfection and Ball Spin	$H_{BI} = 2 \cdot H_{BS} = \dfrac{D}{d_b}\left(1 - \left(\dfrac{d_b}{D}\cos(\alpha)\right)^2\right)$

Where z is the number of balls, d_b is the ball diameter, D is the pitch diameter and α is the contact angle, as shown in Figure 11.

3.2.3 *Torque Ripple*

Torque ripple, originating from the motor, manifests as uneven torque distribution around the rotation axis (T_Z). Torque ripple encompasses only deterministic (periodic) signals along the z axis, while other random disturbances are termed as torque instabilities. The origins of torque ripple in BLDC motors can be categorized into three groups: motor characteristics, motor structure, and motor control [15]. Ripples associated with motor characteristics arise from inherent physical attributes and parameters of the motor manufacturing materials. Consequently, their mitigation hinges on material selection for the motor. Motor structure pertains to the motor shape and dimensions, including its components. Motor control pertains to the motor control technique, which can also be manipulated to minimize torque ripple.

The torque ripple has a small contribution to the satellite pointing error compared to other types of microvibrations because the engine orders of torque ripple are not significantly amplified by wheel resonances (note that the wheel resonances are the cause of the highest peaks in the other microvibration spectra). These elevated peaks often breach the pointing error requirement. Furthermore, the maximum magnitude of torque ripple typically remains below $0.01\,Nm$. This value is significantly lower than the magnitudes of the other five types of microvibrations, each ranging in the order of a few

Nm and $0.1\,Nm$. In conclusion, the amplitude of torque ripple escalates with its frequency. The torque ripple at low frequencies appears notably smaller than $0.01\,Nm$. On the other hand, the torque ripple at high frequencies (exceeding $500\,Hz$) exhibits a significant amplitude (but stay under $0.01\,Nm$). However, vibrations at this elevated frequency range do not efficiently propagate through the spacecraft structure to affect the payload [16].

3.2.4 *Torque Instabilities*

Torque instabilities are referred to as random or transient disturbance on the reaction torque along the rotor axis of rotation (M_Z) [2].

On literature [17], three types of torque instabilities are observed and summarized in Table 4:

- *Torque noise* refers to a stochastic torque signal that appears alongside the generated reaction torque. This phenomenon is present across all operational modes, including constant speed, acceleration, and deceleration. With the exception of established sensor and setup resonances, the magnitude of torque noise is around $2 \cdot 10^{-5}\,Nm$;

- The *oil jog* phenomenon is thought to be due to the accumulation of excess oil at a particular point within the bearing. This amount of oil fills up the gap between the cage and the races, resulting in a sudden increase in friction [2]. Typically, the oil jogs are only present at the newly assembled bearing. They disappear with an accumulation of wheel rotation in an order of a few hundred hours;

- *Torque jump* is described as a rapid and abrupt reduction in reaction torque exceeding $0.005\,Nm$. This phenomenon typically endures longer than oil jogs, spanning over 5 seconds to a few hours. Comprehensive analysis of torque jump attributes this occurrence to instability in the bearing cage.

Table 4 - Summary of torque instability characteristics.

Type	Property	Temperature	Wheel Speed	Lubrification
Noise	Noise floor	Negligible	Increase (10% in $0...3000$ RPM $range$)	Slightly higher for over-lubrification
Oil jog	Occurrence	More frequent at higher temperature	Max. in $800...1200$ RPM $range$	More frequent for over-lubrification
	Amplitude	Lower and higher temperature	Max. at ~ 500 RPM, decrease at higher speed	Higher for over-lubrification
	Duration	No dependency	Decrease	No dependency
Torque jump	Occurrence	More frequent at lower temperature	More frequent at higher wheel speed	Appear only at over-lubrification
	Amplitude	Higher at lower temperature	Increase with speed from 1000 RPM	Inconclusive
	Duration	Sustained longer at lower temperature	No dependency	Inconclusive

In contrast to microvibrations, torque instabilities can be mitigated to some extent through an appropriate control strategy implemented in the Attitude and Orbit Control System. Hence, the discussion on torque instabilities is confined to this particular section. This thesis does not delve further into the torque instabilities.

3.2.5 *R/MWA Structural Modes*

The structural characteristics of a R/MWA are significantly influenced by its configuration. Generally, the impact of torque-induced vibrations is neglected due to the dominance of the flywheel angular speed, where the motor-driven spin speed of the flywheel far exceeds the perturbation angular speed within the torque Degree of Freedom (DoF). Consequently, an R/MWA can be described as a system with five DoFs, consisting of a singular DoF for axial translation, two DoFs for each radial (or in-plane) translation, and two DoFs for each radial (or out-of-plane) rotation. This results in the presence of five prevailing structural modes, which, owing to the symmetry around the axial axis, can be simplified into three modes known as:

- axial translation mode;
- radial translational mode (also referred to as *lateral*);
- radial rotational mode (also referred to as *rocking*).

Figure 12 shows a simplified model of a rotation mechanism with a single axial degree of freedom and two degrees of freedom in the radial direction [18].
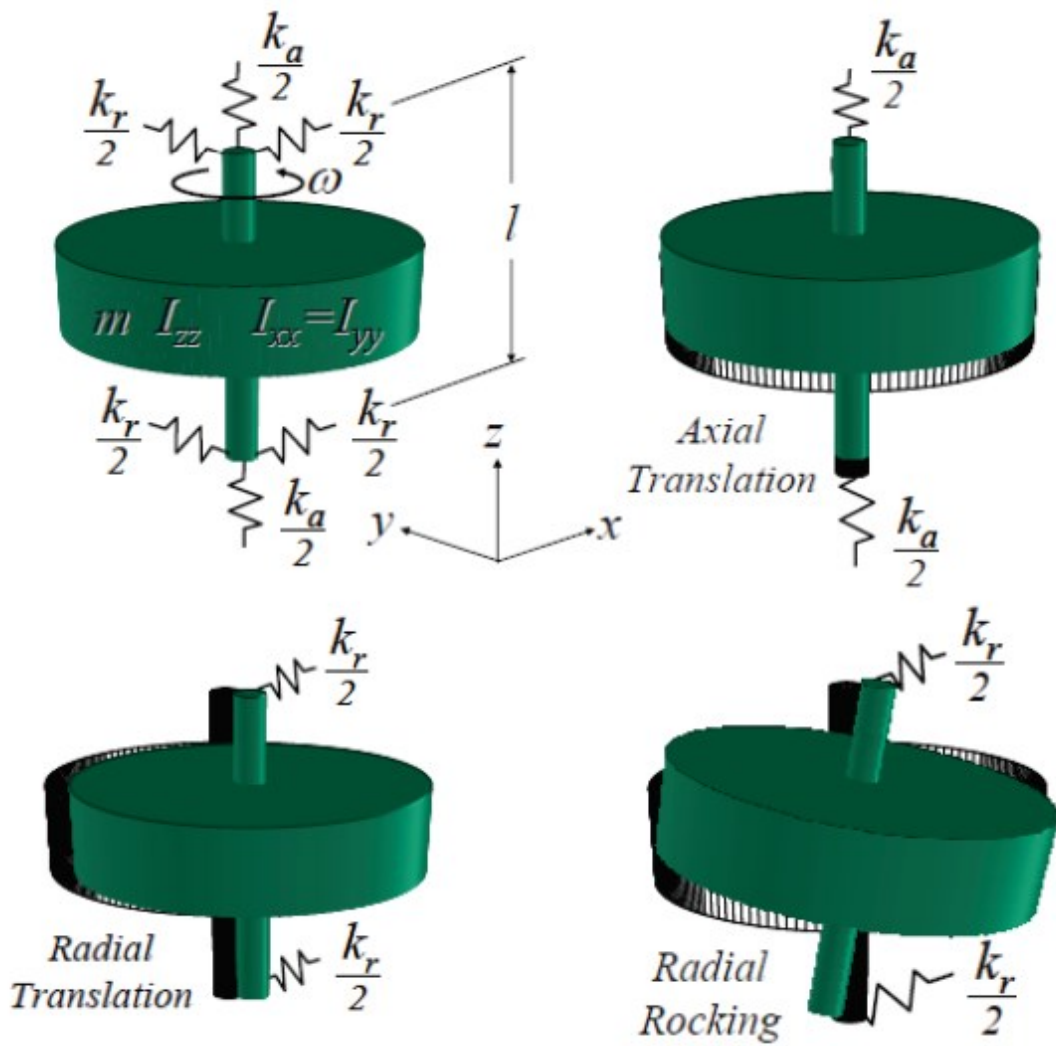
Figure 12 - Simply supported model of rotation mechanism and fundamental resonance modes.

The related frequencies are:

$$f_a = \sqrt{\frac{k_a}{m}}$$

$$f_r = \sqrt{\frac{k_r}{m}}$$

$$f_o = \sqrt{\frac{K_T}{I_{xx}}}$$

where K_T is the cross-axis torsional stiffness and I_{xx} is the cross-axis moment of inertia of the flywheel [1].

As the speed increases, the gyroscopic precession of the rotor gives rise to the formation of a whirl mode in the majority of rotational mechanisms. Additionally, the rocking mode experiences a division into two distinct natural frequencies: a slower frequency where the whirl opposes the rotation, and a faster frequency where the whirl direction aligns with the rotation. The divergence of whirl frequencies follows the relationship:

$$f_n(\omega) = \pm \frac{I_{zz}\omega}{2I_{xx}} \pm \sqrt{\left(\frac{I_{zz}\omega}{2I_{xx}}\right)^2 + \frac{K_t}{I_{xx}}}$$

With $f_n(\omega)$ the force amplitude of the fundamental at the drive frequency, I_{xx} the polar moment of inertia of the flywheel cross-axis torsional stiffness of the suspension and ω the wheel speed.

Figure 13 shows the variation of the eigenfrequencies with the rotational speed, which is called modified Campbell diagram. In the representation are displayed: combining speed-dependent disturbances arising from imbalanced rotating masses, the bearing imperfections, the motor with whirl frequencies and the primary static resonance frequency of the wheel assembly. This diagram enables the identification of *"critical speeds"* [18] .
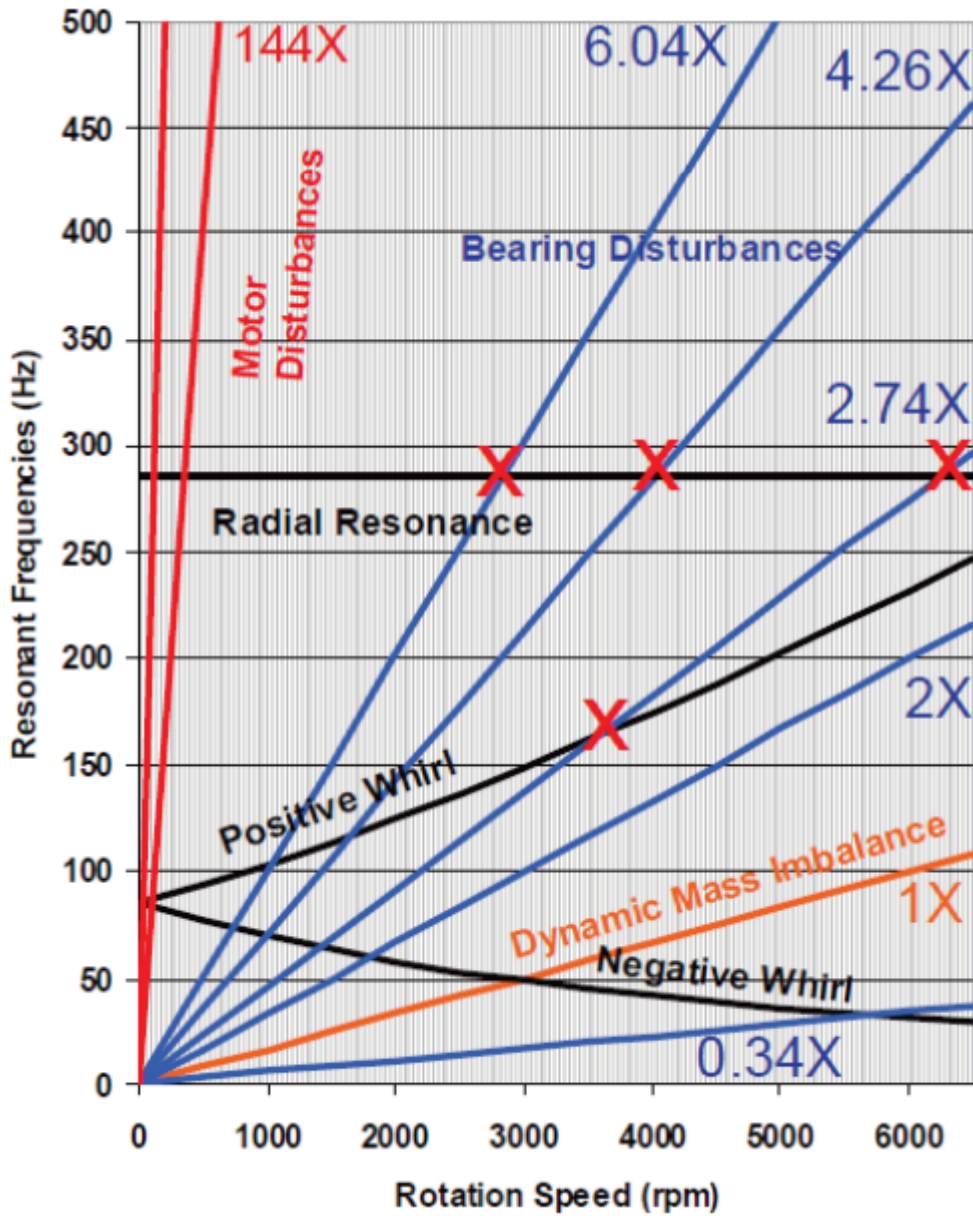
Figure 13 - Modified Campbell diagram showing significant coincidences of wheel assembly resonances and speed dependent disturbances (mass imbalance, bearings, motor).

In addition to the modified Campbell diagram, the associated spectra of disturbances are commonly displayed in the form of cascade or waterfall plots where a noise or vibration spectrum as a function of time or speed is shown in a 3D view. Illustrations of these cascade or waterfall plots are displayed in the following figures (Figure 14 - Figure 15), taken from a case study illustrated in [18].
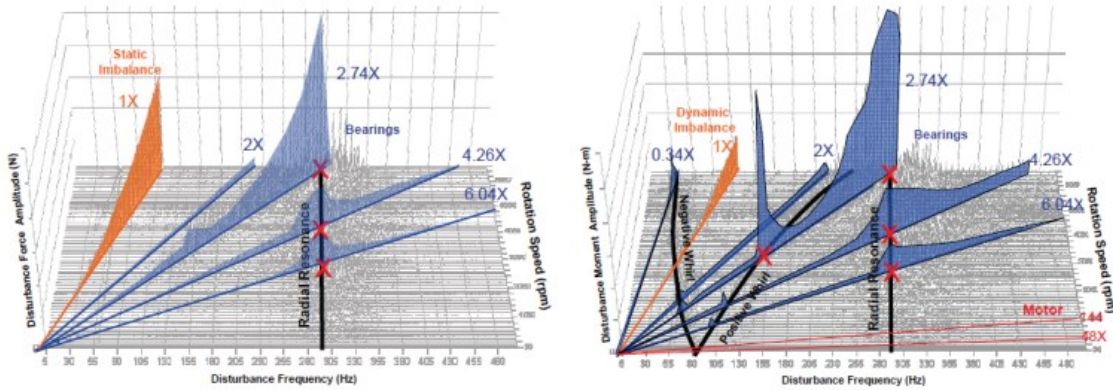
Figure 14 - Radial force and moment disturbance waterfall plot.
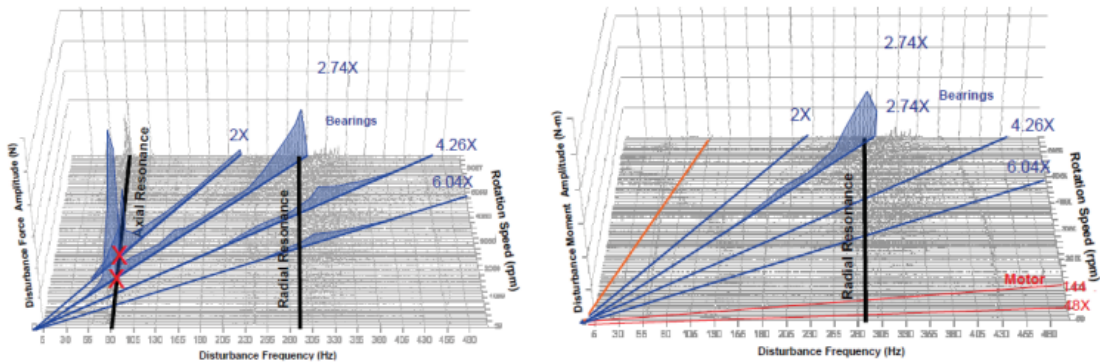
Figure 15 - Axial force and moment disturbance waterfall plot.

The imbalances in the flywheel (both static and dynamic) generate continuous disruptions as the wheel speed varies. The resultant force and torque are directly proportional to the square of the spinning speed and manifest at a frequency corresponding to the flywheel rotation rate. Consequently, the disturbance manifests as a gradually intensifying diagonal ridge (representing the fundamental harmonic) as the wheel speed progressively rises from 0 rpm, as depicted in Figure 14.

The sub- and super-harmonics also constitute tonal disturbances but emerge at fractional or integer multiples of the flywheel rotation rate. These disruptions exhibit considerably lower amplitudes and often stem from irregularities in bearings, motor cogging, motor drive inaccuracies, bearing friction, and lubricant dynamics, as documented in [18].

Chapter 4
MICROVIBRATION SENSOR PAYLOAD

In this chapter, a more detailed examination is conducted on the design of the microvibration sensor as the payload of AlbaSat. This section delves into the process of designing and specifying the necessary characteristics of the sensor to ensure its optimal functionality within the AlbaSat mission framework.

The initial phase of this endeavour encompasses the establishment of the precise payload objectives pertaining to the AlbaSat mission. Subsequent to this, an exhaustive exposition concerning the dimensioning of the sensor and the selection of the prerequisites for this distinct space segment will ensue. Ultimately, a comprehensive explication of the embraced model philosophy governing the development trajectory of the MVS will be delineated.

4.1 Payload Objectives

One of the fields of study on which the University of Padova, and specifically the Dipartimento di Ingegneria Industriale (DII), has dedicated significant attention to is the development of *high-stable pointing mechanisms*. In this specific scenario, there has been consideration of the potential development of a sensor capable of measuring microvibrations on space.

Microvibrations on spacecraft represent an issue for payloads requiring high pointing accuracy and/or stability over time [19], and they might represent a particular concern for CubeSats and small satellites that, usually, are not equipped with very-high performance attitude control systems.

The behaviour of microvibrations on ground differs from the one on orbit due to the different conditions between the two environments e.g., different boundary conditions, different mounting status of flexible accessories, structure dynamic bias induced by gravity or air damping. In addition, there is a lack of information about microvibrations

on small satellites in the published scientific literature. Hence, collecting reliable measures of the possible vibrations spectra in realistic operational scenarios represents a significant research activity.

Within the context of the AlbaSat mission, a paramount objective of the microvibration sensor payload is to conduct an exhaustive investigation into the microvibration environment prevalent during diverse mission phases. This investigation assumes particular significance due to the inherent challenges associated with studying microvibrations.

The main mission objective is to collect information on microvibrations experienced by payloads on a CubeSat caused by the MW that represents one of the most important microvibrations contribution. The data collected by a dedicated sensor is used to understand how the effect of the former is spread inside the satellite whenever the MW is powered on.

Moreover, existing literature underscores the pressing need to enhance the precision and reliability of various subsystems, especially those related to pointing accuracy and optical systems. The microvibration sensor, therefore, serves as a pioneering step towards addressing this need by facilitating comprehensive data collection, analysis, and characterization of microvibrations in the space environment. In doing so, it not only advances the understanding of these phenomena but also contributes to the development of future CubeSat missions, ultimately enabling more precise and effective satellite systems for a wide range of applications.

Furthermore, there is no CubeSat that has ever investigated such field with a dedicated payload so far.

Summarizing, the objectives of the MVS payload are:

1. To study the microvibration environment on the satellite due to Momentum Wheel;
2. To address the need for enhanced precision in future CubeSat missions, particularly in optical and pointing systems through the comprehensive collection, analysis, and characterization of microvibration data in the unique space environment.

4.1.1 *MVS Payload Data Product*

For what concerns the data obtained by the microvibration sensor, they will enrich the current knowledge on the microvibration environment on CubeSats, hence working within the framework of highly-stable pointing mechanisms.

In the last years the pointing precision requirements of the payloads mounted on CubeSats are becoming increasingly stringent. However, there is a lack of knowledge on the microvibrations environment onboard the CubeSats. The second mission objective of AlbaSat will fill this knowledge gap by measuring microvibrations caused by the MW. Microvibrations will be measured with a bandwidth between $0.1\ Hz$ and $500\ Hz$ and with a resolution of $100\ \mu g$. The mission will generate $300\ MB$ of data that will deepen the knowledge on the microvibrations onboard CubeSats.

The data will be elaborated by the team and published in scientific journals. In addition, the data obtained by measurements in space will be compared with the results of the numerical simulations and the tests performed before the launch. The results of this study will be published to deepen the guidelines to future mission on how to simulate and tests the microvibrations environment.

4.2 **Dimensioning and Requirements Selection**

In the process of sizing the MVS and specifying its requirements, the research endeavour commenced with a meticulous review of scientific literature. However, the primary impetus was derived from an in-depth analysis of microvibration sources, which encompassed rotor imbalances, ball bearing imperfections, torque ripple, and various other potential contributors to disturbances. This comprehensive examination, notably expounded upon in Chapter 3 of the study, served as the foundational underpinning for comprehending the precise nature and distinct characteristics of the vibrations that the MVS must have the capacity to detect and quantitatively assess.

The starting point for the sizing process was the mathematical modelling of disturbances and to investigate the characteristic of the MW selected by the ADCS subsystem for AlbaSat.

This enabled the research team to gain a systematic understanding of the behaviour of microvibrations emanating from the MW, providing insights into their magnitudes, frequencies, and temporal patterns.

4.2.1 *AlbaSat Momentum Wheel*

AlbaSat is going to exploit CubeADCS from CubeSpace for the attitude control.

The selection of CubeSpace CubeADCS Y-Momentum for AlbaSat ADCS was a result of a comprehensive evaluation, driven by two primary considerations. Firstly, this choice was made because it ensures that the satellite meets the necessary performance criteria, aligning with the mission objectives. Secondly, the CubeADCS Y-Momentum offers the advantage of having its components pre-integrated when delivered to the end user, streamlining the integration process. CubeADCS Y-Momentum provides the capability for $3 - axis$ stabilized attitude control. This means it can maintain the satellite orientation with precision, ensuring that the IS is continuously pointed in the direction of the velocity vector, while the MRR remains oriented towards the Nadir direction. Furthermore, the subsystem enables pitch manoeuvres within the orbital plane by regulating the speed of a MW, allowing for enhanced flexibility in satellite operations. The wheel is biased to an offset speed to provide gyroscopic stiffness to the satellite, and magnetorquers are used to control the orientation of the satellite to stay Nadir pointing. An essential feature of CubeADCS Y-Momentum is its flexibility. Users can select the appropriate sensors and actuators based on specific mission requirements. Those selected for the mission are reported in Table 5.

Table 5 - Components of the ADCS of AlbaSat.

	Name	Quantity
Sensors	Fine sun sensor	2
	Coarse sun sensor (up to 10)	6
	Rate sensor	3
	Magnetometer	1
	Redundant magnetometer	1
Actuators	Magnetorquer	2
	Coil	1
	Momentum Wheel	1

These sensors and actuators are integrated into PC104 boards, ensuring compatibility and reliability. These PCBs are interconnected with an interface board, facilitating seamless communication with both a dedicated controller and an onboard computer, thereby enabling precise control and monitoring of the ADCS system. This integration approach contributes to the overall efficiency and effectiveness of AlbaSat ADCS, ultimately supporting the success of the mission.

The CubeADCS Y-Momentum configuration with mounted small reaction wheel and the system physical architecture are shown, respectively, in Figure 16 ([20]) and Figure 17.

Among the available options, the <u>Small CubeWheel</u> has been chosen.
The Small CubeWheel is mounted on the connector interface of the ADCS, and it has three sets of four M2 mounting holes on three different facets, as illustrated in Figure 18. The outer dimensions of the wheel are $28\ mm\ x\ 28\ mm\ x\ 26.1\ mm$. The characteristics of the Small CubeWheel are summarized in Table 6.
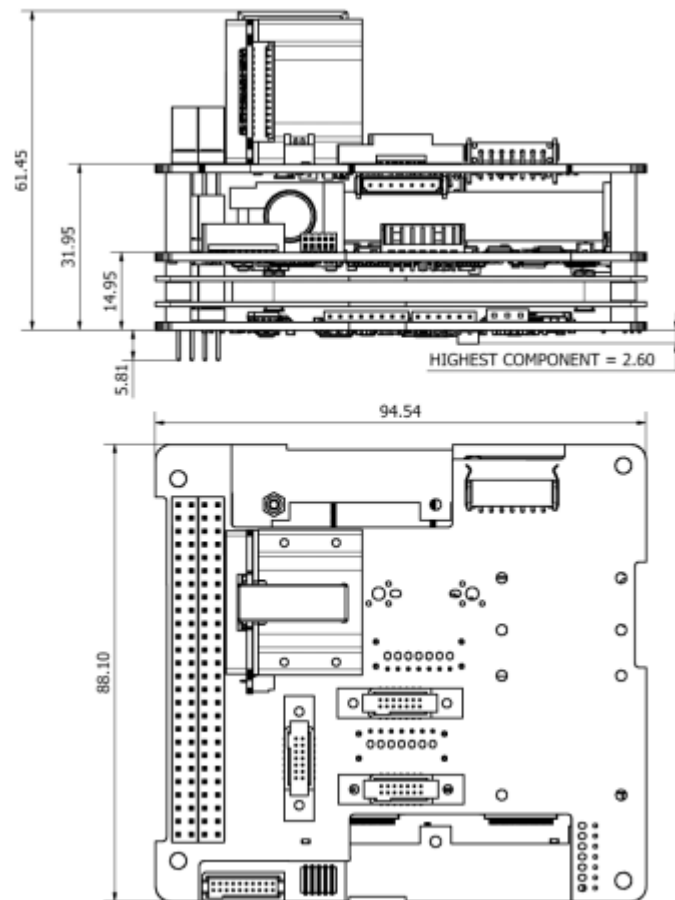
Figure 16 - CubeADCS Y-Momentum configuration with mounted small reaction wheel [20].
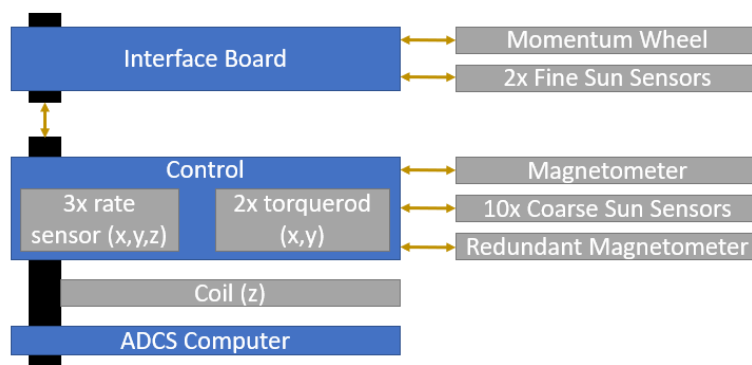
Figure 17 - ADCS of AlbaSat physical architecture.
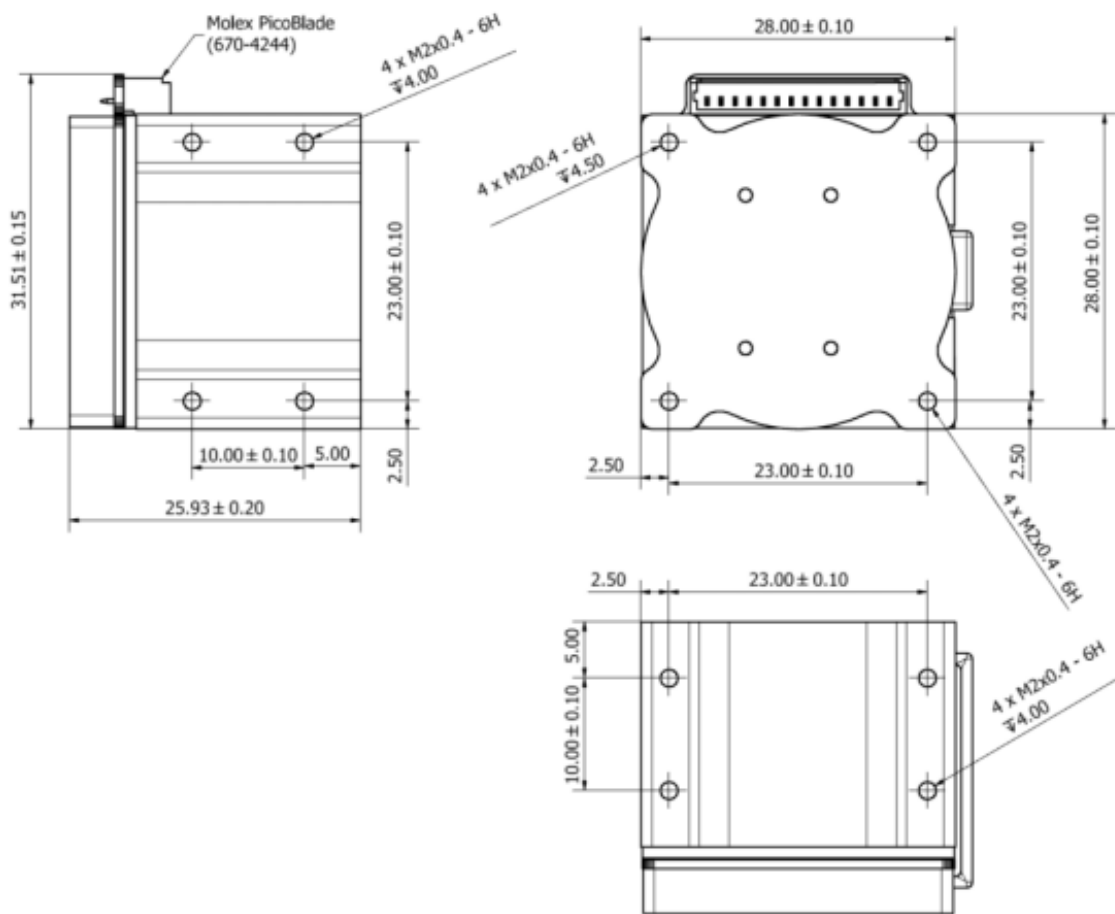
Figure 18 - Small CubeWheel mechanical interface [20].

Table 6 - CubeWheel S characteristics.

Performance	Value
Maximum Wheel Speed $[rpm]$	$\pm\,8000$
Maximum Momentum $[mNms]$	1.7
Maximum Torque $[mNm]$	0.23
Static Imbalance $[g \cdot cm]$	< 0.003
Dynamic Imbalance $[g \cdot cm^2]$	< 0.005
Physical	**Value**
Mass $[g]$	50
Dimensions $[mm]$	$28 \times 28 \times 26.2$
Electrical	**Value**
Supply Voltage $[V]$	$3V3\ \&\ Vbat$
Idle Power $[mW]$	65
Average Power $[mW]$	150
Peak Power $[W]$	0.65
Environmental	**Value**
Vibrations $[g\ RMS]$	14.16
Operating Temp $[°C]$	$-10\ to\ 60$
Radiation $[kRad]$	24

From the reported values it is possible to estimate the disturbance fundamental harmonic, engine order $h = 1$. The term engine order refers to signals of which frequency shows a linear dependency with the wheel speed Ω. Assuming that the rotating speed of the wheel during the mission is in the interval $1000 \div 7000\ rpm$, one can obtain the minimum centrifugal force, related to the static imbalance, by using equation $\boldsymbol{F_s = U_s \cdot \Omega^2}$ (2):

$$U_s = 0.003\ g \cdot cm$$

$$F_{s\,min} = 0.003 \cdot 10^{-3} \cdot 10^{-2} \cdot \left(\frac{1000}{60}\right)^2 \simeq 8.33 \cdot 10^{-6}\ N$$

As a primary objective, a minimum force variation of the same order of magnitude the result just achieved is fixed, hence:

$$F_{detec} \leq 1 \cdot 10^{-6} \, N$$

where F_{detec} is the minimum detectable force.

The choice to size based on static imbalance stems from a broader decision regarding simplicity and cost-effectiveness. Indeed, it was decided to use a single accelerometer sensor capable of measuring accelerations along three mutually perpendicular axes. Furthermore, CubeSat missions come with stringent budget constraints, and employing a single accelerometer to measure forces along all three axes can significantly reduce the overall payload cost. Multiple accelerometers, especially those capable of measuring both forces and moments (related, for example, to dynamic imbalance) in all directions, can be costly in terms of both equipment and integration (at least 4 accelerometers would be required in preferred positions to fully characterize the microvibrations of a momentum wheel). Simplifying the project by using a single accelerometer can streamline the development process. Undoubtedly, it reduces the complexity of integration and calibration, making it easier to ensure the sensor accuracy and reliability. Additionally, CubeSats often have limited resources in terms of space and power, and a single sensor is more efficient in this regard. In line with the specific payload objectives, measuring forces along the three axes is sufficient, providing valuable information without adding complexity due to additional sensors. Lastly, managing data from multiple sensors can be more complex, requiring additional computational resources on the satellite. Using a single accelerometer simplifies data collection and management, reducing computational burden. These things considered it is required that only one accelerometer sensor capable of measuring accelerations along all three axes shall be used.

Microvibrations generated by R/MWs are usually expressed in N instead of acceleration g, since the vibrations caused by the reaction wheel is generally considered as a force source rather than a speed for a space vehicle. This can be explained by the fact that the MW mass is much less than the overall spacecraft. As a result, disturbance forces from the MW onboard are equivalent to a blocked force source and no movement is produced. However, accelerometers, which represent the payload sensors, usually detect acceleration expressing it in g. To pass from N to g one must know the mass to which the force is applied to:

$$g = \frac{F}{m \cdot 9.81}$$

Supposing that the sensor mass does not exceed 1 g one obtains a minimum resolution for the accelerometer equal to:

$$Minimum\ resolution \simeq 1 \cdot 10^{-4}\ g \simeq 100\ \mu g$$

Furthermore, it is imperative to select an accelerometer with an appropriate range to meet the specific requirements of the application. If the expected acceleration falls outside the accelerometer designated range, signal saturation may occur, potentially leading to inaccurate or even unattainable measurements. It is customary to encounter accelerometers with selectable or configurable ranges, enabling the choice of the most suitable measurement interval for the application. To determine the specific acceleration range for the analysed application, it is essential to ascertain the maximum acceleration that could be present in the signal.

This requirement necessary for sensor selection was established with reference to a practical example found in the literature [9]. Drawing requirements for the MVS from an existing practical example found in scientific literature is a strategic decision with multiple advantages. It essentially means that the criteria governing the choice of the sensor have been derived by studying a real-world scenario documented in prior research or mission reports. This approach holds several merits for the MVS design. Firstly, in the domain of microvibrations and spacecraft attitude control, certain sources of disturbances, like rotor imbalances or bearing imperfections, tend to be recurrent and consistent across missions. By referring to past missions or studies, one can leverage the wealth of collective knowledge and solutions developed over time. Moreover, the space industry encourages collaboration and knowledge sharing. The reports and research papers of earlier missions provide comprehensive insights into the challenges faced and the solutions devised. Leveraging this shared knowledge can significantly expedite the development process of the payload.

However, it is crucial to note that while literature provides valuable insights, it is essential to tailor these requirements to suit the specific needs of the current mission. Not all aspects of a previous mission may be directly applicable, and adjustments may be necessary to align with the unique goals and constraints of the new endeavour.

Finally, it was impossible to calculate the geometric and mass characteristics of the MW mounted on AlbaSat, as the necessary tools for accurate calculation were unavailable, and these specifications were not provided by the manufacturer.

A bibliographic reference [9] was chosen in which the validity of a mathematical linear model was tested through practical experiments to best represent an MWA. This model can also be applied to the MW that AlbaSat possesses and clarifies the expected microvibrational disturbances in the test output. Detailed expressions of the linear mathematical model adopted in [9] can be found in the Appendix B

Linear mathematical model of MWA.

Hereunder, the experiment conducted in [9] is briefly presented.

A larger momentum wheel with the characteristics listed in Table 7 was considered. A conservative approach was chosen at this stage, as it was believed that transient acceleration spikes could potentially occur under specific operational conditions or during specific manoeuvres.

Table 7 - Parameters of the MWA from [9] used for the comparison.

Parameter	Value	Source
Working speed range $[r \cdot min^{-1}]$	± 5000	Manufacturer
Maximum speed $[r \cdot min^{-1}]$	< 6100	Manufacturer
Static imbalance $[g \cdot cm]$	0.217	Manufacturer
Dynamic imbalance $[g \cdot cm^2]$	0.130	Manufacturer
Mass of MWA $[kg]$	3.39	Manufacturer
Mass of the flywheel $[kg]$	1.282	
Moment of inertia of the flywheel $[kg \cdot m^2]$	$I_{1xx} = I_{1yy} = 0.00321$ $I_{1zz} = 0.00641$	Calculated
Moment of inertia of the MWA $[kg \cdot m^2]$	$I_{xx} = I_{yy} = 0.01030$	Calculated
Natural frequencies $[Hz]$	$f_{kx} = 250$ $f_{ky} = 250$ $f_{kz} = 125$ $f_\alpha = 62$ $f_\beta = 62$	Experimental estimation
$k_x, k_y, k_z \ [N \cdot m^{-1}]$	$3.16 \times 10^6,$ $3.16 \times 10^6,$ 7.9×10^5	Calculated
$k_\alpha, k_\beta \ [N \cdot m \cdot rad^{-1}]$	4.87×10^2	Calculated

The microvibrations test was carried out using a measurement setup comprising a Kistler table 9253B12 and an optical tabletop. The MWA was affixed to the Kistler table, which recorded the forces and moments generated by the MWA in three directions. The Kistler table, in turn, was placed on the optical tabletop. The optical tabletop served the dual purpose of isolating vibrations from the surrounding environment and maintaining the Kistler table in a horizontal position. Throughout the test, the MWA was operated across a range from 0 to $6000\ rpm$, with increments of $100\ rpm$, and measurements were taken at $5-minute$ intervals. This allowed for an investigation of the vibrations generated during steady-state conditions at each rotational speed. In general, the raw experimental data obtained from the Kistler table are somewhat coarse. As a result, a series of data processing techniques are applied to capture the primary frequency components of the disturbances caused by the MWA.

The experimental campaign has demonstrated the full validity of the linear model and has also shown, as already mentioned in Chapter 3, that the maximum measurable force values can be assessed in cases where structural resonance occurs. Moreover, it is demonstrated that the radial disturbance forces are very similar to each other. Therefore, the outputs related to radial disturbance forces (x and y) and those related to axial disturbance force (z) are shown in Figure 19.
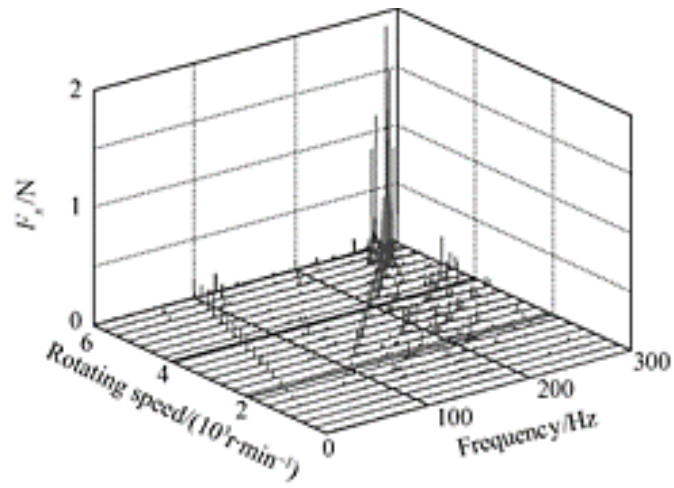
(a) F_x
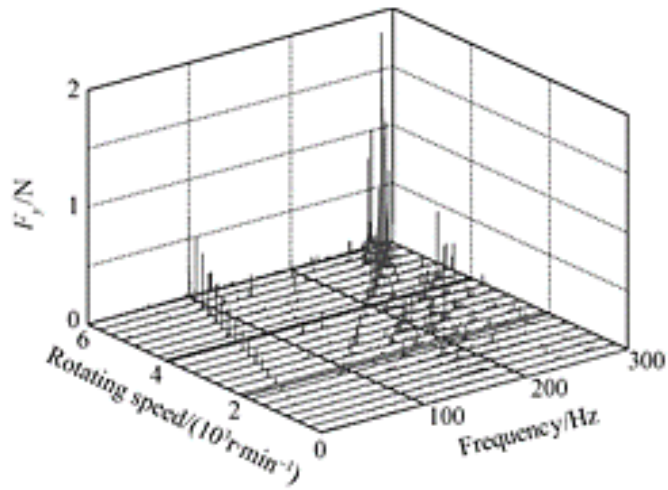
(b) F_y
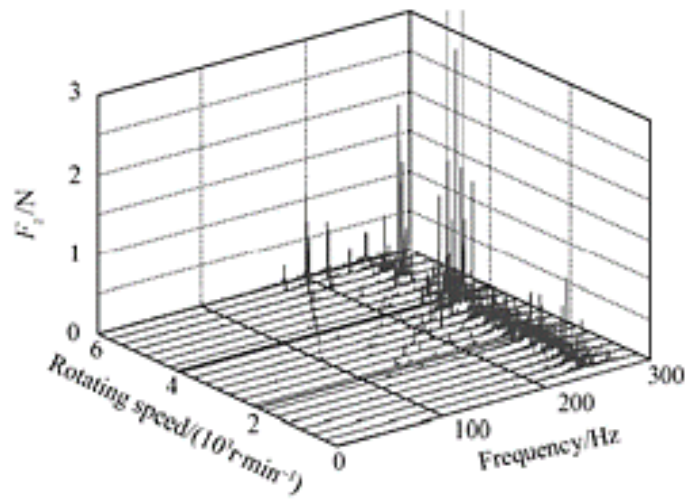
(c) F_z

Figure 19 - Waterfall plots MWA of reference [9].

Referring to the theory previously explained, Figure 19 shows that a dynamic amplification occurs when the bearing imperfections intercept the structural mode frequencies of the MW, especially inside the interval of the radial translation frequencies between 250 and 290 Hz. Such disturbance is high when the rotating speed is close to 6000 rpm since the forward whirl frequency intercept the radial translation frequency at 7000 rpm. The analysis reported in [9] shows maximum forces at the interface (without considering structural modes) below 4 N.

Taking into account the analysis conducted on the MW in reference and considering that the MW used in the AlbaSat project is smaller, along with reduced input errors, it is possible to determine the required dynamic range for the accelerometer. By analysing the available accelerometers, one can chose one of them which has:

$$Dynamic\ range = \pm 2\ g$$

Another fundamental parameter to fix is the band of interest.

Considering the study conducted in [9], Figure 20 illustrates the frequency components observed during typical rotational speeds when the MWA is spinning at 3000 rpm. Furthermore, the amplitudes of certain higher harmonics surpass those of the fundamental harmonic.
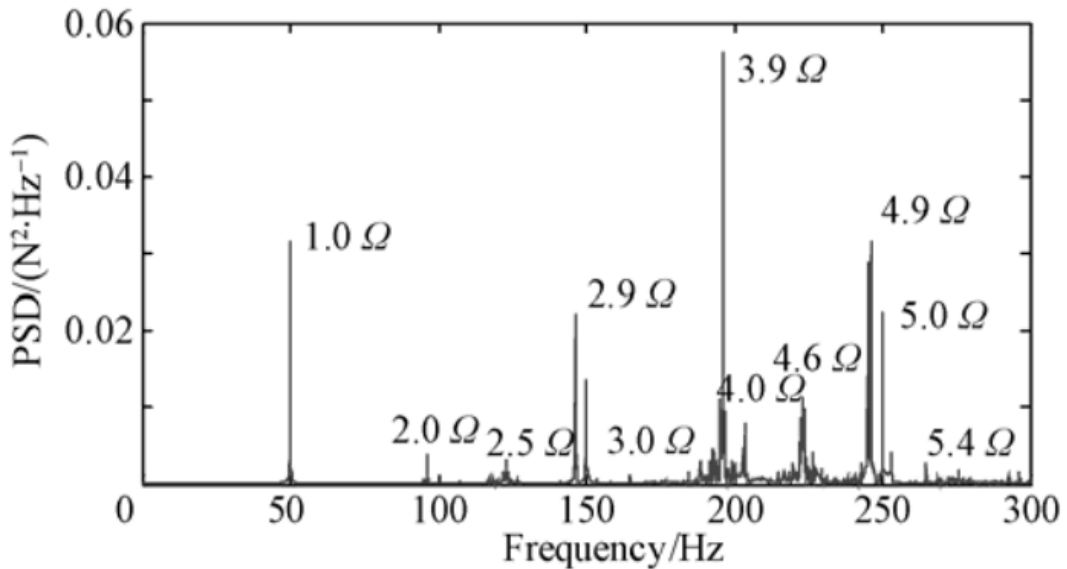
Figure 20 - Power spectral density of F_x ($3000\ rpm$) [9].

It can be observed that the amplitude of certain harmonics is greater even than the fundamental harmonic because of dynamic amplification generated when polyharmonic disturbances and structural modes interact with each other.

Assuming to extend the analysis to the engine order to the fourth order (that is most significative as suggested by the Power Spectral Density (PSD)) and considering a maximum rotation speed of the MW of AlbaSat equal to $\Omega = 7000\ rpm$, frequency band can be fixed at:

$$0.1\ Hz < f < \frac{4 \cdot 7000}{60} \simeq 500\ Hz$$

Naturally, a wide bandwidth (i.e., a range of input frequencies) implies low sensitivity (or scaling factor), and vice versa.

In signal processing and measurement systems, bandwidth refers to the range of frequencies that a system can effectively detect or transmit. A wide bandwidth means that the system can capture a broader range of frequencies, including both low and high-frequency components. Sensitivity, on the other hand, refers to how effectively the system responds to small changes or variations in the input signal. In this context, sensitivity is related to the ability to detect weak signals or small changes in the measured data. When a system has a wide bandwidth, it can capture a broad range of frequencies, but it may be less sensitive to small changes in the signal. Conversely, if a system is highly sensitive, it can detect small variations in the signal, but it may have a limited bandwidth and be less effective at capturing a wide range of frequencies. So, the wider the bandwidth, the lower the sensitivity, and vice versa. This trade-off is important to consider when designing measurement systems, as the choice of bandwidth and sensitivity depends on the specific application and the desired level of detail in the measured data.

Moreover, the sensor should provide an Output Data Rate (ODR) of at least $100\ Hz$ to capture high-frequency microvibrations.

Another important aspect to consider for the accelerometer choice is the sensor noise. A low noise allows better microvibrations measurements reducing the uncertainty of the values obtained. In the present case, a noise density less than the minimum detectable value is chosen:

$$Noise\ spectral\ densiy \leq 100\,\frac{\mu g}{\sqrt{Hz}}$$

This decision is crucial because it ensures that the sensor noise floor is below the threshold of what needs to be detected and measured. By keeping the noise level well below the minimum detectable value, the accelerometer becomes highly sensitive to even the smallest microvibrations, enhancing the accuracy and reliability of the collected data.

Low power consumptions, dimensions and weight are also important parameters since such sensors has to be fitted into a CubeSat that has reduced resources of space and power. In terms of power, it can be fixed:

$$P_{consumption} \leq 100\ mW$$

The PC104 board housing the sensor should not exceed $10\ cm\ (width) \times 10\ cm\ (length) \times 1.5\ cm\ (height)$ to fit comfortably within the allocated space of the CubeSat.

The PC104 board should weigh no more than $100\ grams$ to ensure it does not exceed the CubeSat weight constraints.

Measurement stability is also very important for the payload mission success since microvibrations have to be detected correctly for the entire mission period. Key parameters in such terms are the following:

$$Non\ linearity \leq 1\%\ FS$$

where FS stands for Full Scale;

$$0\ g\ offset \leq 100\ mg$$

Temperature range shall be considered as well for the choice of the accelerometer:

$$-10\ °C < T < 70\ °C$$

The sensor, furthermore, shall be compliant with the onboard electronic systems and shall provide a suitable communication interface. Most accelerometers adopt an entire acquisition chain that allows to send acceleration data in digital for through *I2C* or *SPI* serial protocols.

Table 8 summarises the requirements of the MVS.

Table 8 - MVS requirements

ID requirement	Description
Payload mission requirements	
MVS-MI-010	The payload should be capable of achieving specific scientific objectives related to the measurement of microvibrations generated by the MW
MVS-MI-020	The MVS should be work, without problems, for the expected operational duration of the payload, accounting for AlbaSat mission requirements
MVS-MI-021	The payload should be reliable and operate without failures for the entire mission duration
MVS-MI-030	The payload success will be measured by its ability to capture and transmit microvibration data for analysis
MVS-MI-031	The MVS should be able to perform 100000 measurements per axis as a mission success criterion
MVS-MI-032	The sensor should be capable of collecting $300\ MB$ of data
MVS-MI-040	The MVS should have a minimum detectable force of $F_{detec} \leq 1 \cdot 10^{-6}\ N$
MVS-MI-041	The sensor resolution should be sufficient to capture vibrations in the frequency range of $0.1\ Hz\ to\ 500\ Hz$ with a minimum of at least $100\ \mu g$
MVS-MI-042	The output data rate of the sensor should be $\geq 100\ Hz$
MVS-MI-043	The dynamic measurement range of the sensor should be $\pm\ 2\ g$
MVS-MI-050	The payload should be designed for an operational lifetime of at least $24\ months$
MVS-MI-060	The sensor's noise spectral density should be less than $100\ \mu g/\sqrt{Hz}$ to minimize measurement uncertainty.
MVS-MI-061	The MVS should have a $Non\ linearity \leq 1\%\ FS$
MVS-MI-062	The MVS should have a $0\ g\ offset \leq 100\ mg$

MVS-MI-070	The payload should support telemetry for health monitoring and telecommand for reconfiguration if needed
MVS-MI-080	The sensor should have 3 sensitive axes: $x - y - z$
Design requirements	
MVS-DE-010	The weight of the PC104 board should not exceed $100\ g$ to stay within the CubeSat weight limitations
MVS-DE-020	All components, including the accelerometer and PC104 board, should be designed to withstand the mechanical stresses of launch and space conditions
MVS-DE-030	The payload should be radiation-hardened to endure the space environment
MVS-DE-040	The payload design should ensure mechanical compatibility with the CubeSat interface and attachment mechanisms
MVS-DE-050	The sensor and microcontroller, when combined on the PC104 board, should have a maximum power consumption of no more than $100\ mW$ to ensure it operates efficiently within the power budget of the CubeSat
MVS-DE-060	The PC104 board housing the sensor should not exceed $10\ cm\ (width) \times 10\ cm\ (length) \times 1.5\ cm\ (height)$ to fit comfortably within the allocated space of the CubeSat
MVS-DE-070	The sensor should be compliant with the onboard electronic systems and shall provide $UART$ as communication interface
MVS-DE-071	The design should include safety features to prevent electrical or mechanical hazards
MVS-DE-072	The MVS should be compliant with electromagnetic interference and electromagnetic compatibility regulations to avoid interference with other onboard equipment
MVS-DE-080	The design should consider potential risks and include mitigation strategies to minimize mission disruption

MVS-DE-090	The total cost for producing a single PCB104 board, including all necessary components such as the accelerometer and microcontroller, should not exceed 500 €. This cost should cover materials procurement, manufacturing, assembly, and all associated expenses required to obtain a fully functional and ready-to-use board
Operational requirements	
MVS-OP-010	Temperature range of the MVS shall be: $-10\,°C < T < 70\,°C$
MVS-OP-020	The payload should be operable and monitorable remotely from the GS
MVS-OP-030	The payload should have modes for activation and deactivation during the mission
MVS-OP-040	The MVS should not pose any risks to the overall mission, and its operations should not interfere with other satellite components
MVS-OP-050	The payload should be designed to operate maintenance-free throughout its operational lifetime
MVS-OP-060	The payload should comply with all applicable space regulations and international laws
MVS-OP-070	The payload should undergo rigorous testing and verification procedures to ensure it meets all established requirements

4.2.2 Estimation of Generated Data

The procedure used to estimate the amount of data generated by the MVS over the mission period is detailed below.

One of the objectives of the payload is to gather microvibrations data, equivalent to 100000 measurements per axis, for a total of 300000 microvibration measurements throughout the entire mission duration ($\sim 1.5 \; years$). This specific quantity has been chosen because it is statistically significant for achieving the mission goals.

The data collected by the payload undergoes preprocessing on the satellite before transmission to the GS. The subsequent steps are executed by a dedicated on-board Digital Signal Processor (DSP) and include:

- Computation of the Discrete Fourier Transform (DFT) for each axis;
- Computation of the Power Spectral Density (PSD) for each axis.

The DFT is computed via the Fast Fourier Transform (FFT) algorithm which requires a number of samples equal to a power of two for best efficiency. Given a sample sequence, with $n_0 \leq n < n_0 + N$, the DFT is defined by the equation:

$$X_{DFT}[k] = \frac{1}{N} \sum_{n=n_0}^{n_0+N-1} x[n] e^{-j2\pi \frac{k_n}{N}}$$

where $F = 1/N \, T_s$ is the *frequency quantization step*. The width of the latter, also called *frequency granularity*, is inversely proportional to signal observation interval, $T_W = NT_s$. This means that the larger the observation time, the larger the frequency resolution. Two problems immediately arise:

1. Larger acquisition time means larger memory for storing samples; the DFT can be applied well to periodic signal which periods is exactly NT_s;
2. The DFT can be applied well to periodic signal which periods is exactly NT_s. If this is not the case, spectral leakage occurs.

Hence the following assumptions can be considered:

1. A compromise has to be taken in order not to saturate both computer memories and the communication channel, hence a maximum acquisition time has to be adopted;

2. Windowing must be applied when it comes to compute the DFT on the signal samples sequence.

To obtain a frequency resolution of granularity of $F = 0.1$ Hz:

$$NT_s = \frac{1}{F} = 10$$

Because of the Shannon-Nyquist theorem, the sampling frequency has to be at least doubled the frequency (f_{max}) of the quickest signal one wants to observe. In practice, $F_s = 3 \div 5\, f_{max}$. Being the required bandwidth equal to 500 Hz, a sampling frequency of $1500 \div 2500\, Hz$ well satisfies the sampling conditions. Starting from $Fs = 2000\, Hz$, the sampling period becomes:

$$T_s = \frac{1}{F_s} = 0.5\, ms$$

which means that the required number of samples is given by:

$$N = \frac{10}{T_s} = 10 \cdot F_s = 20\, ksamples$$

The FFT requires a number of samples which has to be a power of two. Hence it must be:

$$N = \begin{cases} 2^{14} \rightarrow 16384\ samples \\ 2^{15} \rightarrow 32768\ samples \end{cases}$$

The lower the sampling frequency, the lower the number of samples that are required. To achieve a F_s greater than $1500\, Hz$, a number of samples equal to 16384 has to be adopted. The correspondent sampling frequency becomes $F_s \simeq 1.64\, kHz$. Assuming to store the amplitude value from the accelerometer in $16 - bit$ word, for each acquisition on one axis, the total number of bits is:

$$N_{bit} = N \cdot 16 = 262144\ bit = 32768\ byte$$

The total number of acquisitions has been fixed to 300000, hence total acquisition data size collected would:

$$N_{bit_{tot}} \simeq 300000 \cdot 262144\ b \simeq 78.6\ Gb \simeq 9.83\ GB$$

which, per day, would be equal to:

$$N_{bit_{day}} \simeq \frac{9.83 GB}{548} \simeq 17.9\ MB$$

Where 548 is the estimated duration in terms of days, that is $1.5\ years$ i.e., the expected AlbaSat mission duration.

4.2.2.1 Microcontroller Management

In order to reduce the amount of data sent to the GS, one can consider pre-processing the samples generated by the acquisitions on the CubeSat. It is known that the useful output data size from the FFT of a real value signal, like the one produced by the accelerometer, is halved with respect to the input data size. Furthermore, the bandwidth of interest and the resolution of the microvibration spectrum allows to send only $5000 - 1$ useful amplitudes data after FFT process, that is $n_{PSD} = (5000 - 1) \cdot 16 \simeq 80000\ b$. The drawback is the necessity of implementing a processor unit with dedicated memory for temporarily storing the acquisition samples before the processing phase. This is because to implement the FFT all the samples must be stored in a memory. Hence a memory of at least the size of a single acquisition must be considered in the choice of the processing unit.

Computational speed has also a key role because it can lower the waiting time between two-time adjacent acquisitions. As a rule of thumb, a CPU able to process operations at a frequency greater than $1\ MHz$ can be sufficient. Since the complexity of the FFT is:

$$\Theta\big(N_{samples}\big) = \frac{N_{samples}}{2}\log_2 N_{samples}$$

a clock speed of $1\ MHz$ can be enough to process each acquisition in almost $1/20$ of a second if one clock cycle is used to process a single sample. By letting other half of a second for CPU internal operations, that would allow to have acquisitions separation less than one second. The PSD from the microvibrations data can be computed considering the average from multiple acquisitions. This allows to obtain better knowledge on the microvibration phenomena on the CubeSat and to reduce the amount of data to be sent to the GS without compromising the overall information provided by the raw samples. A processing memory capable of storing at least 10 times the number of acquisition sample must be adopted. Consider computing the PSD from 10 acquisitions, the total amount of data sent to the GS during the mission period is:

$$N_{bit_{mission\ period}} \simeq 80000\ b \cdot \frac{300000}{10} \simeq 2.4\ Gb = 300\ MB$$

that, per day, is:

$$N_{bit_{day}} \simeq \frac{2.4\ Gb}{548} \simeq 4.38\ Mb \simeq 547\ kB$$

The results allow to perform and send a total of 55 PSDs per day to the GS. The procedure so far adopted is shown in Figure 21 while Table 9 summarises all the important results about the data production estimation.

Statistically relevant number of acquisition produced in one year		Legend:
		p number of acquisitions per PSD
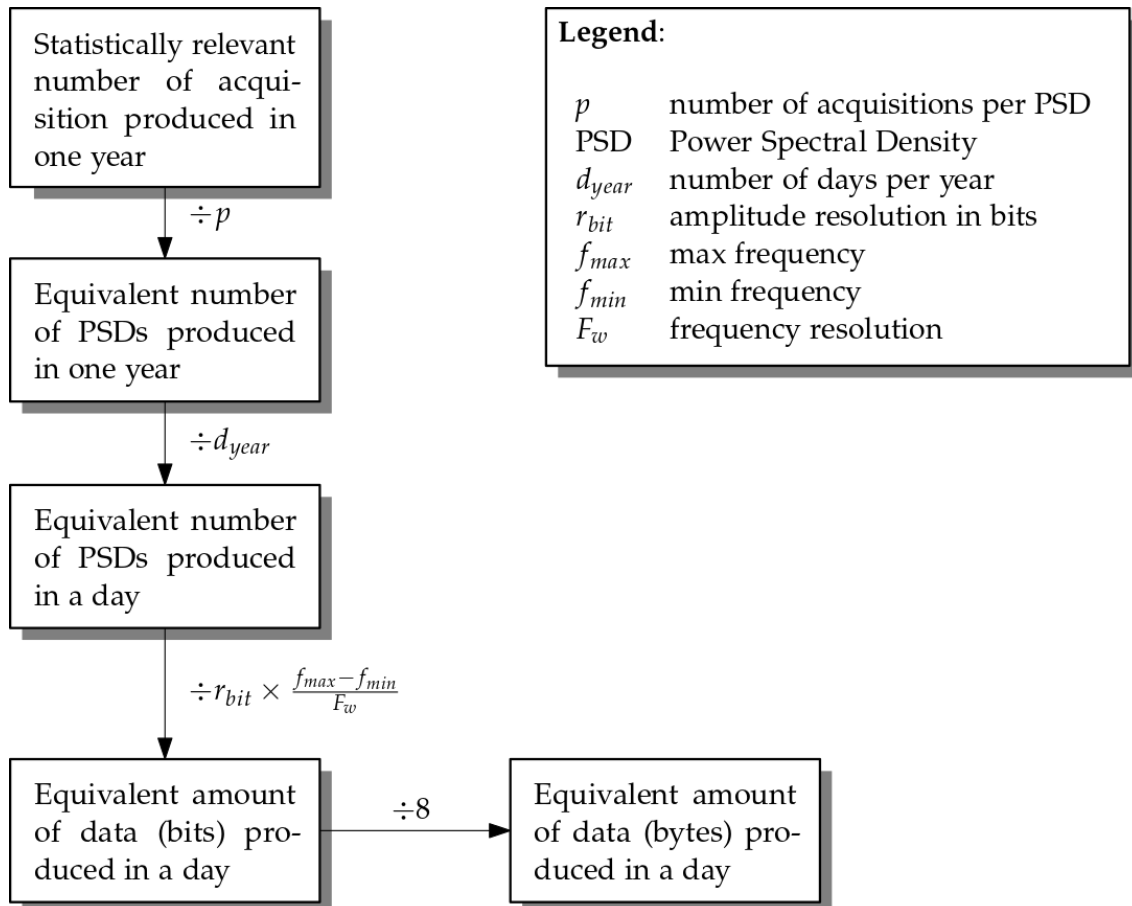
Figure 21 - Payload data production estimation process.

Table 9 - Data production estimation main parameters.

Quantity	Value	Unit
N_{bit}	16	b
$N_{samples}$	16384	
T_w (Acquisition time)	10	s
T_s (Sampling time)	610	μs
F_s (Sampling frequency)	1638	Hz
f_{max}	500	Hz
f_{min}	0.1	Hz
F_w (Frequency resolution)	0.1	Hz
n	200	
k	165	
Bit per acquisition	262144	b
Goal number of acquisition	300000	
N acquisition per PSD	10	
Total PSDs	30000	
Total PSDs per day	55	
Amount of data per PSD	79984	b
Amount of data per day	4382685	b

4.3 **Model Philosophy**

Model philosophy is stated as definition of the optimum number and the characteristics of physical models required to achieve confidence in the product verification with the shortest planning and a suitable weighting of costs and risks [21].

In the model philosophy of the sensor development, a systematic approach is adopted, comprising distinct phases to ensure robust functionality and reliability. The progression commences with the <u>Development Model</u> (DM) phase, where essential functional tests are conducted to validate the core operational aspects of the sensor concept. This model allows for iterative refinement of the design based on test outcomes.

Subsequently, the <u>Qualification Model</u> (QM) phase ensues. Here, a refined version of the sensor, built upon the insights from the DM phase, undergoes comprehensive testing to assess its capability to withstand a range of environmental conditions and operational stressors that it may encounter during its mission. The QM is a model, which fully reflects all aspects of the flight model design, and which, as outlined in [22], is used to complete functional and environmental qualification tests. A qualification model is only required for newly designed hardware. The qualification model is not intended to be used for flight, as it is over-tested. The QM serves as an intermediary step between the DM and the final <u>Flight Model</u> (FM).

Finally, the Flight Model (FM) marks the culmination of the development process. The FM represents the fully matured sensor configuration, incorporating all the design enhancements and lessons learned from the preceding phases. This model undergoes rigorous testing to confirm its readiness for deployment in the actual mission context. The sequential approach, from DM to QM and ultimately to FM, ensures a thorough and systematic validation process, contributing to the overall reliability and success of the sensor operational performance in its intended application.

This philosophy offers the project low risk, completion of qualification activities prior to acceptance, and the ability to use the QM as an integration spare or an in-orbit debugging tool. However, it introduces additional costs and lends itself to longer planning as all hardware has to be purchased twice and test campaigns are conducted on both models. As a result, many university CubeSat teams choose to implement a Proto-Flight Model (PFM) philosophy whereby a single model is manufactured and flown after it has undergone protoflight qualification campaigns and acceptance testing. Typically, these

designs rely on significant flight assets or a robust CubeSat bus so that the associated risk is accepted. In the case of the AlbaSat MVS payload, the increased risk of the PFM approach was not deemed acceptable due to lack of experience within the team [23].
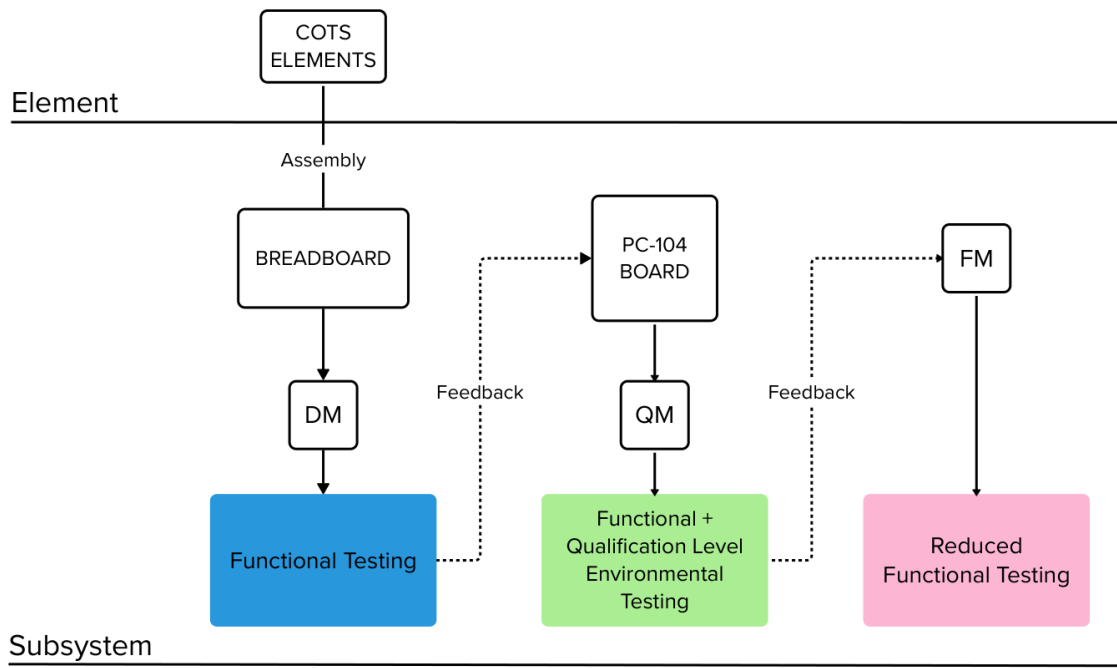
Figure 22 -Model philosophy scheme.

Chapter 5
MVS PHYSICAL AND FUNCTIONAL ARCHITECTURE

This chapter contains a concept selection of the design adopted for the MVS in compliance with the requirements. After a general explanation of the functional architecture of the payload, the focus is on the choice of the type of accelerometer to be used. Then, the selected COTS components are presented in detail. This is followed by a comprehensive description of the hardware of the system. Moreover, 2D and 3D illustrations of the PCB104 qualification board are presented. Finally, the system firmware is briefly explained.

5.1 Functional Architecture of MVS Payload

Figure 23 shows the working principle of the Micro-Vibrations Sensor.
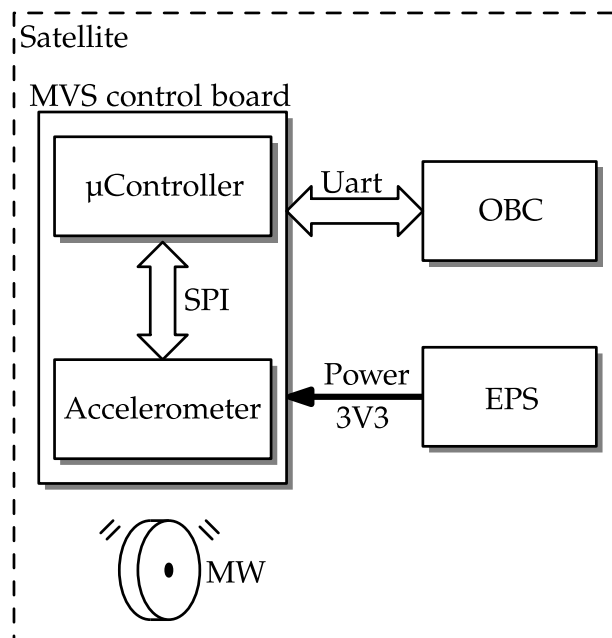
Figure 23 - Representation of the functional architecture of the Micro-Vibrations Sensor.

The MVS control board features an <u>accelerometer</u>, the sensitive component capable of measuring microvibrations, and a <u>microcontroller</u> responsible for data processing. The accelerometer enables the measurement of linear accelerations in all the three spatial directions: $x, y,$ and z. Typically, it interfaces with the microcontroller through a communication interface such as SPI or $I2C$.

The microcontroller serves as the "brains" of the MVS. Its primary responsibilities include acquiring data from the accelerometer, executing signal processing algorithms, and storing data for subsequent interaction with the CubeSat OBC. Communication with the OBC occurs via a $UART$ connection, which serves not only for data transfer but also for sensor configuration. This configuration capability allows the microcontroller to issue commands for starting or stopping measurements.

The PC104 board acts as the physical platform for mounting both the accelerometer and the microcontroller. It also accommodates other auxiliary components, such as damping capacitors and input/output connections. The board is meticulously designed to provide a stable and clean power supply to both the accelerometer and the microcontroller. This design ensures that the components are arranged compactly and efficiently for optimal functionality.

The system is engineered to receive a $3.3\,V$ voltage supply from the CubeSat EPS.

The overall electrical schematic is then used to create the Printed Circuit Board (PCB) in PC104 format to be inserted into the CubeSat stack. The PC104 format not only defines the board dimensions compatible with the MVS-DE-060 requirement but also the power and communication lines between the satellite subsystems.

5.2 Accelerometer Selection Trade-off: Matching Payload Requirements to Available Solutions

Today, various technological solutions for accelerometers are available. It was therefore necessary to make a trade-off among the various accelerometer options available in the market to meet the payload requirements.

Table 10 compares the main types of accelerometers used in the aerospace sector, listing some fundamental characteristics.

Table 10 - Comparison of accelerometers.

Property	MEMS (Micro-Electro-Mechanical System)	Piezoelectric	Capacitive	Magnetic
Operation	Measure capacitive/resistive changes in response to acceleration	Generate voltage in response to mechanical forces	Measure changes in electrical capacitance	Detect changes in the magnetic field induced by acceleration
Resolution	Typically, in the μg range (microgravity), i.e.: $1 \div 100\ \mu g$	Depends on crystal quality but can be in the μg range	Typically, in the μg range (microgravity)	Depends on sensor sensitivity
Sensing Range	From fraction of g to hundreds of g, i.e.: $0.001 \div 100\ g$	From fraction of g to thousands of g	From fraction of g to hundreds of g	Limited to small measurement ranges, usually fractions of g
Other Key Features	Relatively low cost, compact size, lower power consumption	High sensitivity and frequency response but can be expensive and bulky	Good linearity and low noise but require careful calibration	Don't require physical contact but can be influences by external magnetic fields

The decision to employ MEMS accelerometers for the MVS payload is substantiated by several key factors:

a. *Compact Size* and *Reduced Weight*: MEMS accelerometers are renowned for their miniaturized form factor. This attribute holds paramount importance, as it was specified during the payload dimensioning phase, given the constraints of limited space and weight capacity. Furthermore, their diminutive size facilitates seamless integration within the system, necessitating minimal design modifications;

b. *Low Power Consumption*: MEMS accelerometers exhibit a noteworthy characteristic of low power consumption, which is instrumental in conserving energy resources;

c. *Reliability* and *Precision*: MEMS accelerometers commercially available are meticulously engineered to endure the rigorous conditions of the space environment. They demonstrate resilience in the face of temperature fluctuations, radiation exposure, and the vibrational stresses encountered during launch and orbital operations. Additionally, contemporary MEMS accelerometers offer levels of precision well-suited for the majority of space applications. Their precision capabilities are fully adequate for capturing the anticipated microvibrations throughout the mission;

d. *Cost-Efficiency*: MEMS accelerometers, when compared to their traditional counterparts (as outlined in the Table 10), generally present a more economically viable option;

e. *Seamless Integration*: MEMS accelerometers boast a high degree of compatibility with microcontrollers and other electronic systems, owing to their versatile communication interfaces, such as *SPI* or *I2C*;

f. *Readily Available*: MEMS accelerometers have wide availability in the marketplace, simplifying the procurement of backup components if needed.

In summary, MEMS accelerometers are the ideal choice for the MVS because they provide the necessary performance to accurately measure microvibrations in a space environment while meeting the constraints of space, weight, power consumption, and cost

requirements. Furthermore, the latest MEMS capacitive accelerometers are finding use in applications traditionally dominated by piezoelectric accelerometers and other sensors.

After conducting thorough parametric search and comparing various types of MEMS accelerometers, the *ADXL355* emerged as the most suitable choice that effectively met all the specified requirements.

5.3 Accelerometer: *ADXL355*

The accelerometer used is the *ADXL355* produced by *Analog Devices*. It is a MEMS sensor capable of detecting accelerations in three axes: x, y and z with a maximum resolution of 20 $bits$ and a maximum ODR of up to 4 kHz per axis. It can also measure temperature with a $12 - bit$ resolution.

The information is transmitted externally through digital outputs: the accelerometer can be interfaced with a processing system using either the *SPI* or *I2C* communication protocol. The latter limits the maximum ODR to 800 Hz and, for this reason, it was discarded. In technical jargon, the accelerometer is referred to as a '*slave'* because it responds to requests from a device called the *'master'*, which initiates communication. This applies to both protocols used.

The accelerometer has 36 $8 - bit$ registers, of which 18 are read-only. These registers are memory units that allow reading the acceleration values of the three axes and sensor configurations. It goes without saying that the former can only be read because they are generated by the *ADXL355*, while the latter must be settable. Access to a specific register is done by sending its address, i.e., its ID, followed by a bit that requests either reading (logical value 1) or writing (logical value 0). In the first case, the accelerometer responds by sending the content of the register, while in the second case, it awaits the new value to be written. The complete list of all registers and their functions is detailed in a table in the datasheet [24].

In Figure 24, the functional block diagram of the sensor is presented.
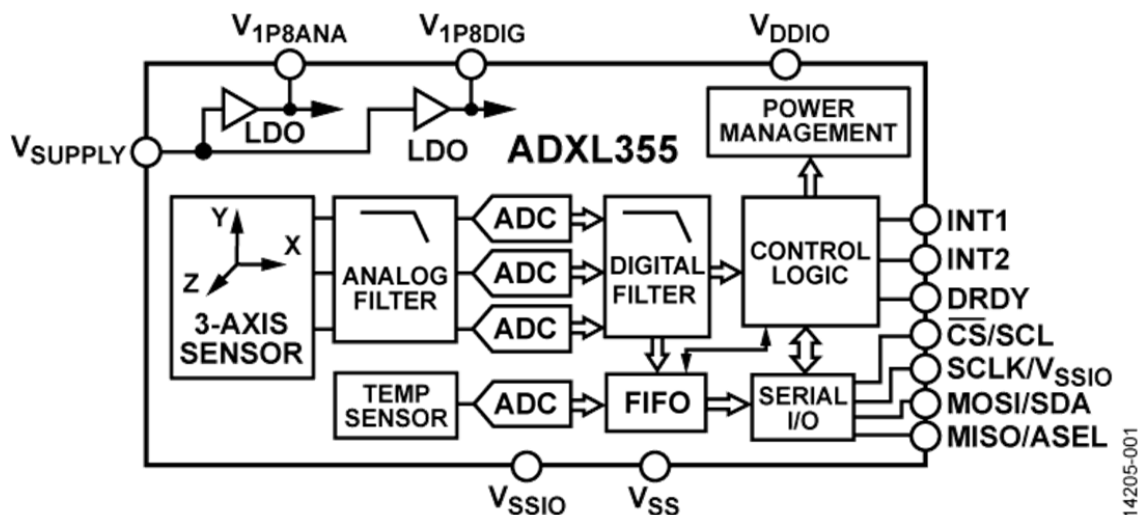
Figure 24 - ADXL355 Functional Block Diagram.

In order to communicate with the accelerometer using the *SPI* protocol, four data lines are required:

i. *Chip Select (CS) Signal*: This is used to indicate to the accelerometer that the master device wants to initiate communication, thus prompting it to activate;

ii. *Clock (CLK) Signal*: This is a periodic, square wave signal generated by the master device and determines the baud rate (or bitrate) of the communication. The slave device must synchronize itself and perform the read or write operation for each cycle of the clock signal;

iii. *Master Output Slave Input (MOSI)*: This line contains the bits coming from the master device that need to be read by the accelerometer;

iv. *Master Input Slave Output (MISO)*: This line contains the bits coming from the accelerometer that need to be read by the master device.

In the *ADXL355* datasheet [24], guidelines for configuring the *SPI* protocol to communicate correctly with the sensor are provided. These guidelines include the maximum frequency of the synchronization signal and the timing diagram to be adopted.

The electrical schematic of the accelerometer section is shown in Figure 25. The only passive components required are decoupling capacitors connected to the device at the power supply terminals. During the design of the printed circuit board, these capacitors should be placed as close as possible to the power supply pins of the accelerometer to ensure more accurate measurements.

The sensor power supply voltage, common to the entire payload, is set to $V_{CC} = 3.3\,V$. Table 11 summarize the characteristics of all pins and whether they are used in the payload.
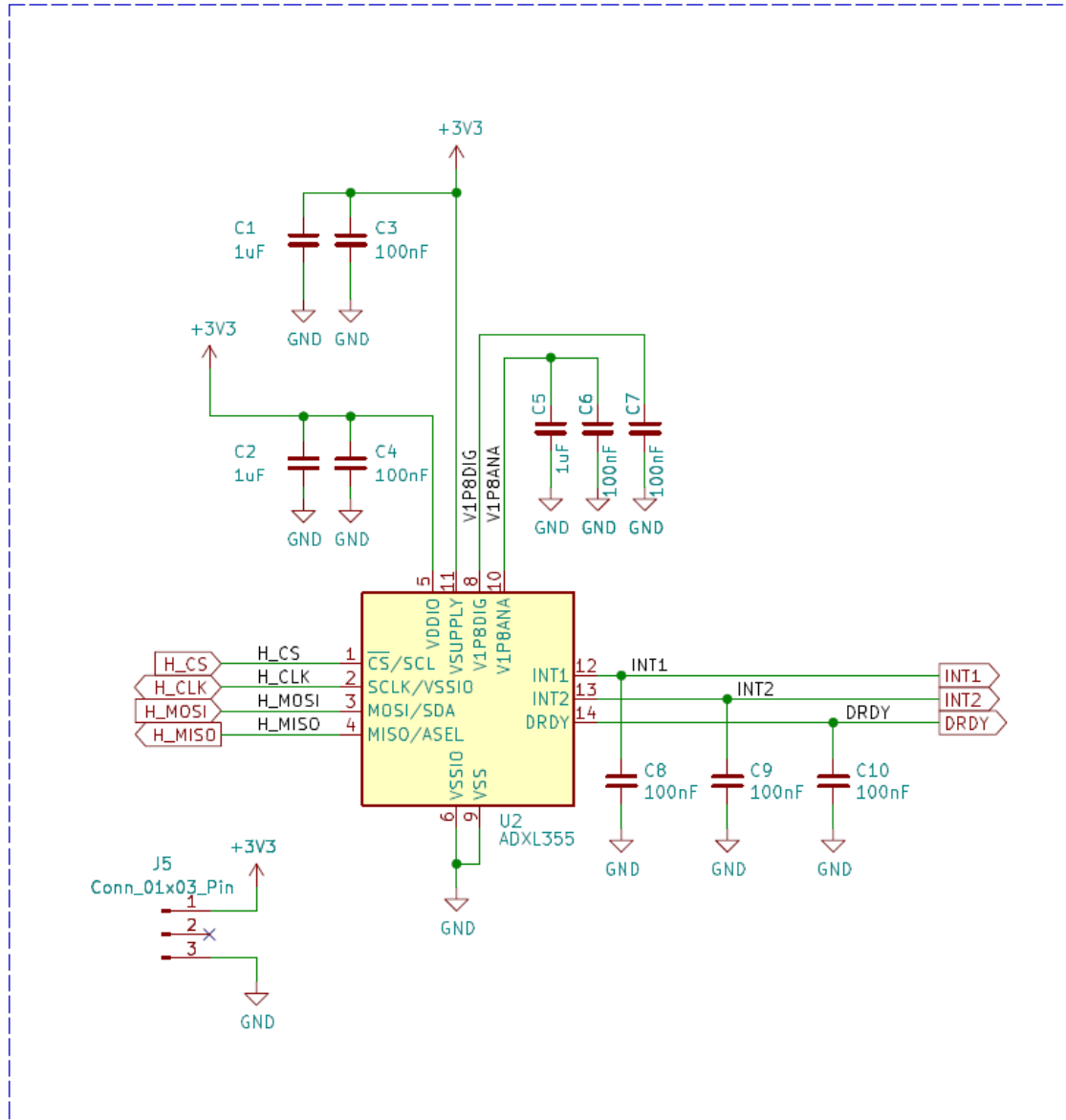
Figure 25 - Schematic illustrating the surrounding circuitry of the accelerometer.

Table 11 - Summary table of *ADXL355* pins.

Pin Number	Mnemonic	Description	In Use
1	$\overline{CS}$/SCL	Chip Select	Y
2	SCLK/VSSIO	Synchronization signal for *SPI* or VSS if *I2C* is used	Y
3	MOSI/SDA	Master Output Slave Input for *SPI* or Signal Data for *I2C*	Y
4	MISO/ASEL	Master Input Slave Output for *SPI* or Alternate Signal Address Select for *I2C*	Y
5	VDDIO	Positive power supply	Y
6	VSSIO	Digital reference	Y
7	RESERVED	Reserved, connect to ground, or leave open	N
8	VIP8DIG	Digital power supply	Y
9	VSS	Analog reference	Y
10	VIP8ANA	Analog power supply	Y
11	VSUPPLY	Power supply voltage	Y
12	INT1	Interrupt 1pin	N
13	INT2	Interrupt 2 pin	N
14	DRDY	Pin Data Ready	N

The tests on the DM were conducted using a development board produced by *Analog Devices*, which implements the same electrical schematic and provides, on a 2.54 *mm* bayonet connector, all the necessary pins for testing.
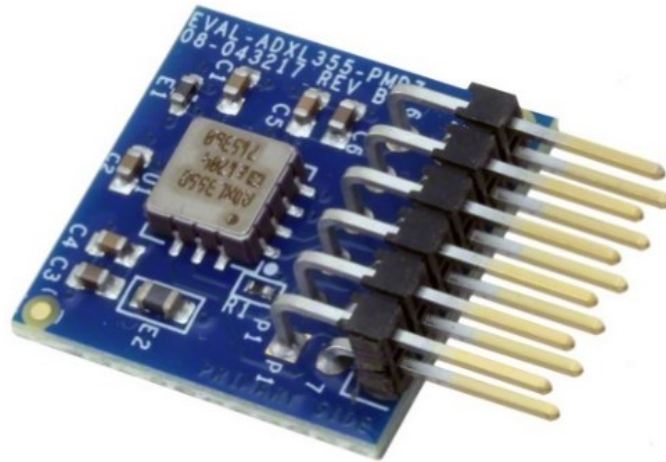
Figure 26 - ***ADXL355*** **Evaluation Board.**

5.4 Microcontroller: *STM32U575*

The chosen microcontroller is the *STM32U575* produced by *STMicroelectronics*. The selection was based on the processor performance, the amount of Random Access Memory (RAM) available for computation, communication peripherals, and power consumption. Additionally, there is a development board available for this microcontroller, the *NUCLEO-U575ZI-Q*, which was used to build the DM.

Figure 27 - NUCLEO-U575ZI-Q development board used for the payload DM.

The connections are made through the bayonet connectors located on the sides of the board, allowing it to be connected to the accelerometer development board.

Here are the main features of the microcontroller:

- $32 - bit$ architecture;
- $2\,MB$ of flash memory and $786\,kB$ of Static Random Access Memory (SRAM);
- Up to $160\,MHz$ clock frequency;
- 22 types of communication protocols, including *SPI*, *I2C*, and *UART*;
- Dedicated co-processor for mathematical operations;
- Up to 136 input/output pins.

For more detailed information on its features, please refer to the respective datasheet [25].

For its operation, the microcontroller requires a clock signal: in this case, an external $32\,kHz$ quartz oscillator is used, which, through a Phase-Locked Loop (PLL) integrated into the microcontroller, allows the processor to operate at a frequency of $160\,MHz$. Alternatively, an oscillator integrated into the microcontroller can be used directly. The microcontroller is powered by a voltage of $V_{CC} = 3.3\,V$.

The microcontroller mode of operation is described in the firmware section; Table 12 with the pin connections. For simplicity and summary purposes, only the pins used in the PCB design are listed.

Figure 28 shows the microcontroller electrical schematic.

Table 12 - List of used microcontroller pins.

Pin Number	Mnemonic	Description
8	OSC_32_IN	Clock input
9	OSC_32_OUT	Clock output
14	NRST	Hardware reset
24	H_CLK	Clock signal for *SPI*
31	H_MISO	Master Input Slave Output *SPI*
32	H_MOSI	Master Output Slave Input *SPI*
48	VCAP	Used by the LDOs (Low-dropout) integrated into the microcontroller
68	USART1_TX	MVS USART1 Trasmitter (to OBC USART1 Receiver)
69	USART1_RX	MVS USART1 Receiver (to OBC USART1 Trasmitter)
72	JTMS/SWDIO	Dedicated to the STM programmer/debugger (Data)
76	JTCK/SWCLK	Dedicated to the STM programmer/debugger (Clock)
77	JTDI/GND	Dedicated to the programmer/debugger
81	H_CS	Chip Select *SPI*
82	DRDY	Data Ready *ADXL355* (not used)
83	INT2	Interrupt 2 *ADXL355* (not used)
84	INT1	Interrupt 1 *ADXL355* (not used)
89	JTDO/TRACESWO	Dedicated to the programmer/debugger
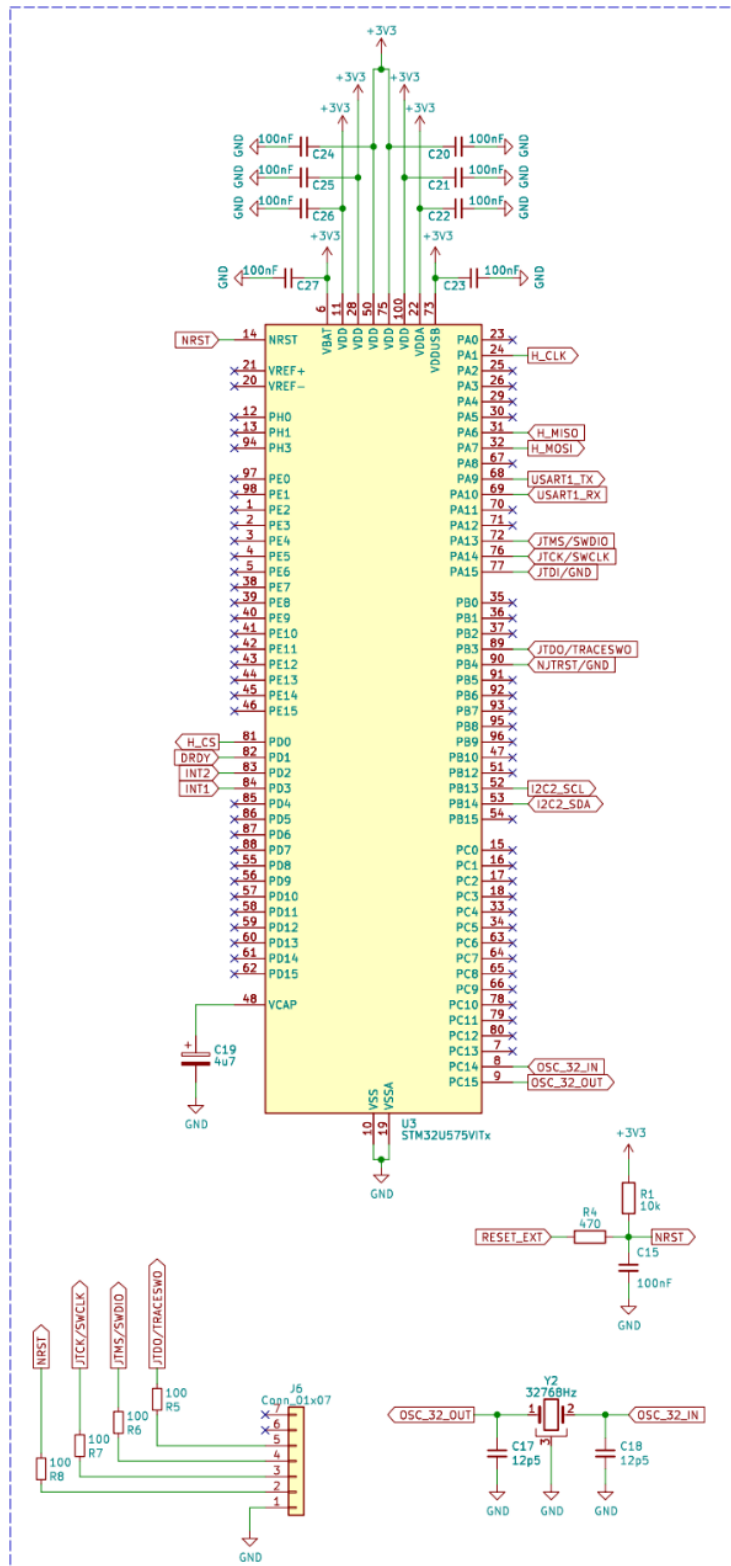
Figure 28 - *STM32U575* **microcontroller electrical schematic.**

5.5 PC104 Connections

The PCB connections were inherited from the OBC datasheet: connections related to power supplies were removed, and a dedicated connector for power supply was added.

Figure 29 - PC104 connectors electrical schematic.

Table 13 provides a list of the used connections. For simplicity and summarization purposes, only the pins with assigned nets (traces) are listed.

Table 13 - List of pins used from PC104 standard connectors.

Pin Number	Mnemonic	Description
1	CAN_Low	Dedicated to *CAN* communication protocol
3	CAN_High	Dedicated to *CAN* communication protocol
33	GND	Ground connection
34	GND	Ground connection
39	USER_1_1	User-defined
40	USER_3_2	User-defined
41	SDA	Dedicated to *I2C* communication protocol
42	USER_3_4	User-defined
43	SCL	Dedicated to *I2C* communication protocol
44	USER_5_2	User-defined
46	USER_5_4	User-defined
47	USER_supply_0	User-defined power supply and selection
48	USER_ supply _1	User-defined power supply and selection
49	USER_ supply _2	User-defined power supply and selection
50	USER_ supply _3	User-defined power supply and selection
51	USER_ supply _4	User-defined power supply and selection
52	USER_ supply _5	User-defined power supply and selection

The connection to the OBC is made through the *MOLEX P2* connector. This connector includes two *UART* data lines and an additional signal for hardware reset of the micro by the OBC in case of no response from the payload. Three other lines are available for user-defined purposes.

5.6 **PCB Design Details**

The design of the PCB for the payload is a crucial aspect of the project. It involves the use of four distinct layers, each serving a specific purpose:

1. *Front Copper Layer*: This layer is the topmost external layer of the PCB and is primarily dedicated to routing signal traces. Signal traces are the conductive pathways that carry electrical signals between various components on the PCB;

2. *Inner 1 Copper Layer*: Positioned just under the front copper layer, this is the upper internal layer. Unlike the front layer, it doesn't contain components or traces visible from the outside. Instead, it serves as a ground plane. A ground plane is an electrically conductive layer that helps with signal integrity, reduces electromagnetic interference, and provides a stable reference voltage for the circuit;

3. *Inner 2 Copper Layer*: This is the lower internal layer of the PCB, situated beneath the ground plane (*Inner 1*). It is dedicated to the power distribution of 3.3 *V*;

4. *Bottom Copper Layer*: Similar to the front copper layer, this is the bottommost external layer of the PCB. It is used for routing additional signal traces, similar to the top layer.

In Figure 30, a three-dimensional representation of the PCB is provided. It is possible to observe that the visible components are soldered onto the upper external layer, which is the front copper layer. This design approach optimizes the use of space while maintaining a clear separation between signal traces, ground, and power planes, which is essential for proper functioning and signal integrity in complex electronic systems.

Additionally, in Figure 31, a 2D representation of the MVS PCB is provided, which will be printed by a reputable company in the field.
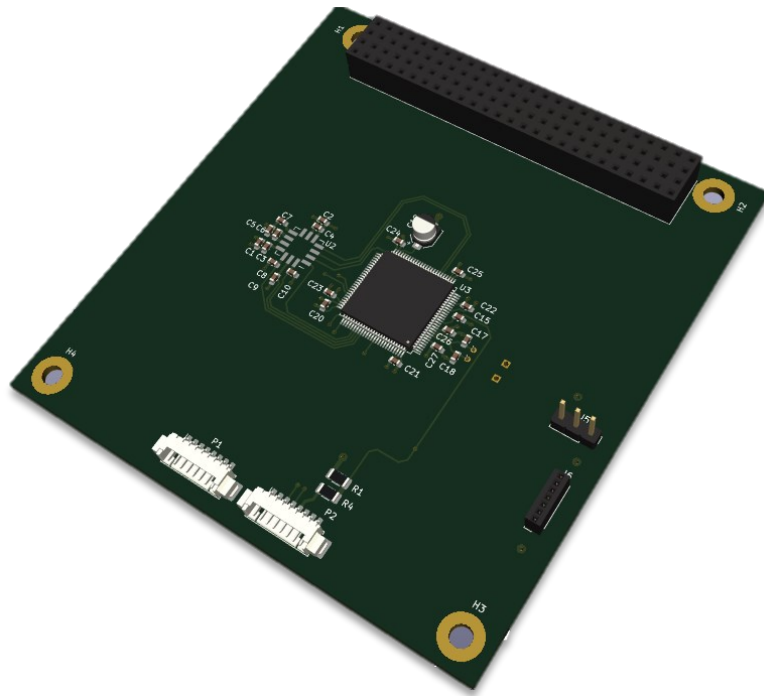
Figure 31 - 3D representation of the MVS PCB, with an emphasis on the top side. The quartz crystal is located on the bottom side.
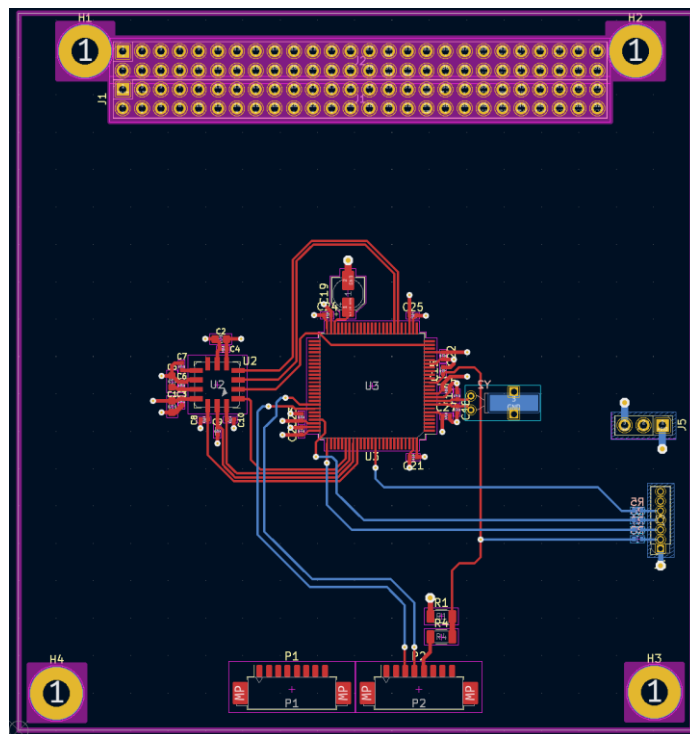
Figure 30 - 2D representation of the MVS PCB.

5.7 **Firmware**

The firmware is structured into the following parts:

1. *Control and initialization routines*, executed at microcontroller startup and after every reset: these routines configure communication peripherals, the device General Purpose Input/Output (GPIO) pins, and set certain parameters related to the internal clock and error management. They also verify the correct operation of the accelerometer and configure it;

2. *Sensor management routine*: organized as a state machine and called once the configuration phase is completed. It interacts with the sensor and is responsible for collecting raw data from the accelerometer, which is stored in a buffer awaiting processing. This routine includes specific functions for reading and writing to the registers of the adopted sensor (*ADXL355*) and is continuously active as long as the microcontroller is powered on. The processing phase, such as FFT and PSD calculations, can be performed in this stage;

3. *Communication and command interpretation routine* for commands sent by the OBC. This routine must also be called continuously by the program. Its role is to interpret and execute commands issued by the onboard computer, as well as to report malfunctions and possible faults so that the OBC can take appropriate action, such as rebooting the payload.

Figure 32 illustrates a simple flowchart illustrating the procedure described so far.
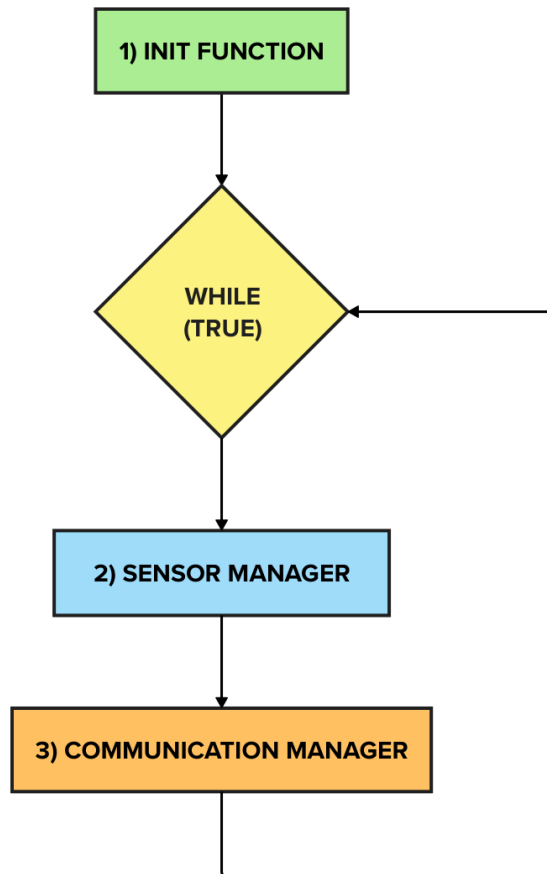
Figure 32 - Simplified firmware flowchart.

The *Initialization routine* performs the following operations in chronological order:

1. Configures the system clock;

2. Configures power management for internal microcontroller peripherals (processor, Analog to Digital Converter (ADC) e Digital to Analog Converter (DAC), etc.);

3. Configures and initializes the microcontroller GPIO peripherals;

4. Initializes the *SPI* peripheral for communication with the accelerometer;

5. Initializes the *UART* peripheral for communication with the OBC;

6. Requests the accelerometer to transmit the values of four system registers and compares them with the corresponding values in the *ADXL355* datasheet. If there are no differences, the accelerometer is functioning correctly and is ready for a software reset. Once the sensor is reset, the function instructs the sensor to enter standby mode.

If there are differences between the values read from the sensor and those reported in the datasheet, the microcontroller signals it. At that point, a factory reset, and a restart of the accelerometer must be performed.

In standby mode (hibernation), it can be can configurated the acquisition frequency, the upper cutoff frequency of the low-pass filter, and the lower cutoff frequency of the high-pass filter, which are integrated into the accelerometer. One can also define its range; in this case, it has been set to ± 2 *g* (MVS-MI-043).

In acquisition mode, it is possible only modify certain registers, as listed at the beginning of the *ADXL355* Register Map section of the datasheet. It is not possible to independently set the sampling frequency and the Low-Pass Filter (LPF) cutoff frequency. Instead, reference should be made to the t to set the ODR_LPF configuration register. The ODR is the frequency, per axis, at which samples are generated. For simplicity, it can be confused with the sensor sampling frequency.

Table 14 - Configuration Values of the ODR_LPF Register.

Hexadecimal Register Value	ODR [Hz]	Cut-off Frequency of the Low-Pass Filter [Hz]
0×00	4000	1000
0×01	2000	500
0×02	1000	250
0×03	500	152
0×04	250	62.5
0×05	125	31.25
0×06	62.5	15.625
0×07	31.25	7.813
0×08	15.625	3.906
0×09	7.813	1.953
$0 \times 0A$	3.906	0.977

The suitable configuration for the CubeSat application is one that sets ODR to $4\,kHz$ and a cutoff frequency at $1\,kHz$. The High-Pass Filter (HPF) has been disabled. The range has been set to $\pm 2\,g$ using the *RANGE* register.

The *Sensor Manager routine*:

1. Initializes variables for FFT calculations;
2. Initiates the accelerometer to start the acquisition process;
3. Reads k samples sequentially from the accelerometer and stores them in a buffer. The data is converted into decimal values compatible with the defined range;
4. Puts the accelerometer in standby mode to save power;
5. Calculates the FFT on the collected k samples;
6. Computes the PSD and divides it by N, adding it to the dedicated buffer;
7. Repeats the process from 1 to 6 for N times.

The final result is the PSD averaged over $N \cdot k$ samples, to be sent to the OBC.

The *Communication Manager routine*:

1. Sends a request to the OBC to transmit acquisition data;
2. Transmits the data to the OBC once authorization is received via *UART*.

This cycle is then repeated indefinitely. The microcontroller must periodically send a bit (or a string) to the OBC to confirm proper operation. If the OBC does not receive this bit, it will perform a physical reset of the payload.

Chapter 6
FUNCTIONAL TEST PLAN

In this chapter, the focus shifts to outlining the comprehensive approach to be adopted for the functional tests of the MVS. The primary objective is to achieve a TRL4 of the payload. This forms an integral part of the test program for the payload, which adheres to rigorous guidelines and procedures to ensure the payload reliability and performance. Two distinct test setups are delineated, designed to address various aspects of the payload functionality. The payload, assembled in a development board, will be integrated on the *Theia Space ESAT* educational CubeSat, available at the laboratories of the University of Padova. To facilitate these tests, a suite of Ground Support Equipment (GSE) and specialized test tools has been identified and integrated into the testing process.

It is expected to conclude the functional testing campaign by the year 2023.

6.1 Elevating CubeSat Success: The Vital Role of Functional Testing

The CubeSat standard mandates that payloads incorporated on nanosatellites must adhere to important requirements, particularly during the launch phase. However, the standard does not mandate extensive testing campaigns; in fact, only environmental testing is obligatory, and it is conducted at levels specified by the launch provider. This results in a notably low success rate for CubeSat missions, which could be significantly enhanced by improving Assembly, Integration, and Testing (AIT) and Assembly, Integration and Verification (AIV) activities, which are typically minimized due to time constraints [26].

Traditional multitone spacecraft are obligated to meet numerous verification and testing criteria that aren't obligatory for small satellites, as per ESA's customization guidelines. Nevertheless, following nearly two decades of nanosatellite missions, statistical investigations into CubeSats have been conducted, notably by the University of Saint-Louis (Missouri, USA) [26].

The pie charts in Figure 33 show that a significant number of failed CubeSat missions are led by universities. However, this is not surprising. Universities often have limited resources, leading to significantly reduced development and testing timelines. In contrast, industrial players utilize expensive standard practices and plan for longer engineering periods, resulting in more reliable spacecraft. 'Crafters' falling somewhere between hobbyists and industrialists, possess the expertise to create reliable vehicles and conduct tests but are generally more accepting of risks than industrial entities.

(a) CubeSats mission status for Hobbyists (2000-2019)

(b) CubeSats mission status for Industrialists (2000-2019)

(c) CubeSats mission status for Crafters (2000-2019)

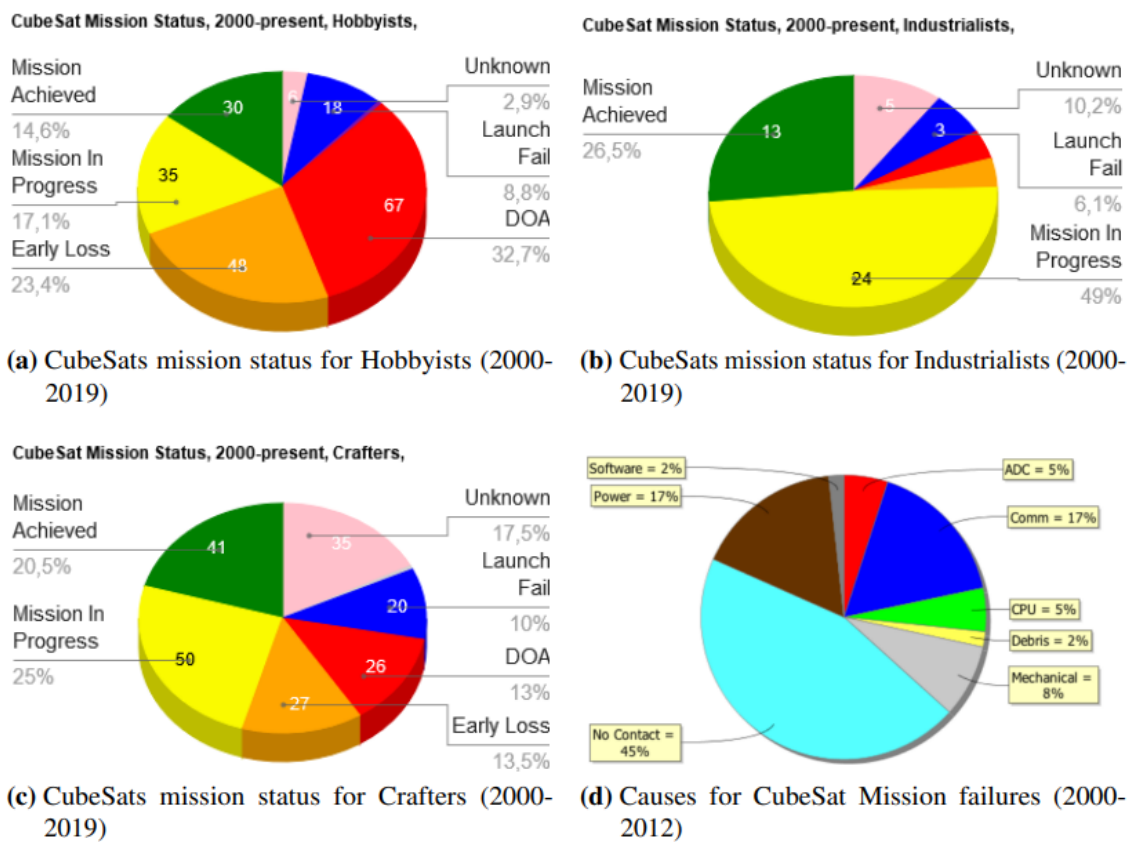**(d)** Causes for CubeSat Mission failures (2000-2012)

Figure 33 - CubeSats mission status grouped per builder type and causes of failure (2000-2019) [26].

93

One noticeable trend in the statistics is that the more time and effort a developer invests in satellite development and testing, the higher the likelihood of mission success.

Figure 33-(d) provides a breakdown of failure causes. Interestingly, over a third of CubeSats fail to establish contact with the ground after launch, making it impossible to diagnose the exact reason for their loss.

Configuration mismatches between communication hardware, power subsystems, and flight processors are a prominent cause of failure. These mismatches result in unrecoverable computer errors, faulty power connections, and inadequate power generation for up/downlink operations. Therefore, it is estimated that about two-thirds of failures stem from inadequate functional integration, which could have been prevented through basic system-level functional testing. University-led projects are especially vulnerable to these issues due to engineering delays, tight testing schedules to meet launch deadlines, and a primary focus on environmental compliance.

From the analysis of this data, it is clear that functional testing is deemed the most crucial. These tests are prioritized as the first step in the testing process and are elaborated upon in this thesis. It is essential to carry out a thorough testing campaign, even in the case of AlbaSat, and more specifically in this section of the MVS payload, considered a space segment element according to the ECSS standards. Within the scope of this thesis, the Functional Test Plan (FTP) of the payload will be described, aiming to define the on-ground activities and procedures necessary to evaluate the functionality of the MVS payload.

The FTP is continuously updated based on hardware production and facility availability.

Defined by ECSS standard [22], a Functional Test (FT) is a "comprehensive test that demonstrates the integrity of all functions of the item under test, in all operational modes" whose main objectives are to "demonstrate absence of design manufacturing and integration error".

In the framework of the AlbaSat project, functional tests are initially executed and defined on the DM of the payload.

Component-level testing demonstrates the complete performance of a component based on its functional requirements, demonstrating that it is ready to be integrated into the system. FTs must be performed before and after environmental tests to ensure that the

space equipment has survived and maintained its functionality. Throughout the environmental test campaign, Reduced Functional Tests (RFTs) are performed, the purpose of which is to verify the major functions of the spacecraft in a relatively short period of time.

In the context of this thesis, neither RFTs nor the qualification tests that the payload will undergo will be presented.

The technique adopted for MVS is the <u>Hardware-In-the-Loop</u> (HIL). This technique is implemented on real hardware and software and may include electrical simulations of system dynamics, environment, or external effects. This is the most capable approach for effective functional testing because it allows verification of the entire hardware and software complex [27].

6.2 **Objectives and Tasks**

The main <u>objectives</u> of <u>functional tests</u> are:

1. *Check the correct assembly of the MVS*: it is important to make sure that all selected COTS components are correctly assembled, all electrical connections are stable and working and that there are no connection or communication problems with the OBC;

2. *Evaluate the ability to detect microvibrations*: the test must verify if the payload is able to accurately detect the microvibrations generated inside the CubeSat. This includes verifying the sensitivity of the payload to microvibrations, the ability to discriminate vibrations from other ambient noises and accurately measuring the detected vibrations.

The <u>tasks</u> related to these objectives are:

- *Verify the accuracy of the measurements*: the main task is to verify the accuracy of the measurements provided by the payload. This includes analysing the linearity of the measurements and evaluating the stability of the measurements over time;

- *Verify compliance with the requirements*: it is necessary to verify if the payload meets the requirements specified, not only in terms of resolution for the accelerometer but also of the data budget obtained (at the microcontroller

95

level). This includes comparing test results against requirements for accuracy, sensitivity, frequency range, and other key parameters established during the payload sizing phase;

- *Document test results*: it is important to accurately document test results, including the data collected, the analyses performed, and the conclusions drawn. This documentation will be useful for the subsequent analysis of the results and as a yardstick for the measurements that will be performed in-orbit.

The objectives and tasks listed allow to demonstrate the validity of the design and performance of the MVS payload, according to the expected requirements. Furthermore, it is demonstrated that there are no defects in the component such as not to guarantee its use, in each level of complexity considered and it is confirmed, at a functional level, that the element is able to complete the required mission.

6.3 **Test Setups**

The techniques used to measure the microvibrations of, for example, reaction wheels are quite well established. There are two main types of microvibration tests: <u>hard-mounted</u> or <u>coupled</u>. In the hard-mounted condition, the wheel is rigidly mounted to a dynamometer table. The models, hence, consider only the dynamics of the wheel, measuring directly microvibrations at the source and ignoring the spacecraft. This is useful for determining wheel microvibrations and for validating the wheel itself but gives no indication of its coupled behaviour with the satellite it will be mounted on. For this reason, coupled models are built, where the dynamics of the satellite are considered and simulated in tests with a mechanically representative structure, such as a mockup. This is usually hung to a ceiling with strings to simulate a <u>free-free boundary condition</u>, such as that imposed by microgravity in space [5].

The microvibrations caused by these sources are transmitted through the satellite structure, exciting the modes of the structure. When a MW excites its mounting structure, the structure itself also excites the MW and so on, creating a coupled motion between the two bodies such that the loads at the boundary are different from those produced by the MW itself when rigidly mounted. It is therefore preferable to choose a coupled test

configuration to obtain the produced microvibrations more accurately even if, however, this solution is not mature in research [2].

In this regard, it was preferred to carry out 'end-to-end' tests using a mockup that manages to represent the configuration of AlbaSat in orbit. The mockup selected for conducting the test is *ESAT* by *Theia Space* (Figure 34), an educational CubeSat of 1U ($10 \times 10 \times 10\ cm$), weighing less than $1\ kg$, available in the laboratories of the DII of the University of Padova.

ESAT has the following spacecraft subsystems:

- Electrical Power;
- Command and Data Handling;
- Attitude Determination and Control;
- Structure.

All the information necessary for the functioning and extension of the *ESAT* is available in the documentation [28].
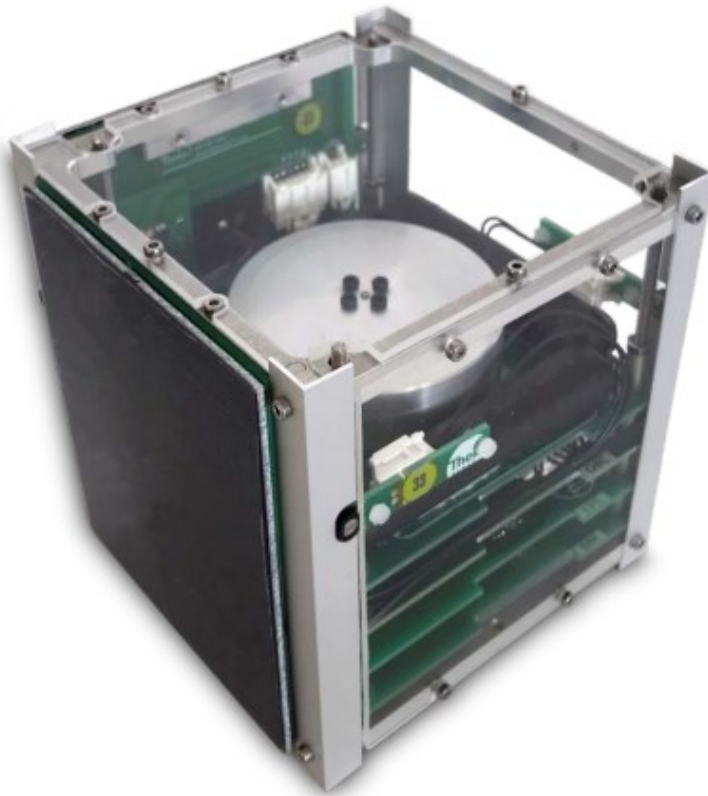
Figure 34 – ESAT [28].

The main source of microvibrations that this CubeSat can produce comes from a MW integrated in the attitude control board, which has the following characteristics:

- It changes the satellite azimuth once assembled on a rotatory table;
- It is actuated by a brushless motor with a digital electronic speed controller, and it is regulated by a user settable PID control loop;
- It is possible to control the duty cycle and angular speed;
- It can rotate clockwise and counterclockwise;
- It has the following characteristics:
  - Wheel absolute speed range: $-8000\ rpm$ to $8000\ rpm$;
  - Wheel nominal operation speed range: $-7200\ rpm$ to $7200\ rpm$;
  - Wheel weight: $50\ g$;
  - Wheel height (alone): $16.5\ mm$;
  - Wheel height (assembled, with mounting screws): $20.3\ mm$;
  - Wheel diameter: $60\ mm$;
  - Wheel inertia moment: $330\ g\ cm^2$;

- o Wheel current consumption ($4500\ rpm$): $550\ mA$;
- o Wheel peak power consumption: $1100\ mA$.

The ADCS takes the instantaneous orientation (azimuth) of *ESAT* and rotates the satellite to follow a certain angle with respect to the reference frame.

It is therefore planned to mount the MVS DM in the test satellite and carry out functional tests on the complete structure. It is chosen to keep the CubeSat in a vertical orientation which therefore aligns its *z* axis with the normal to the ground. The activation of the MW in *ESAT* generates a torque (torsional moment) due to the conservation of angular momentum principle. According to this principle, the total angular momentum of an isolated system remains constant unless external forces or torque act upon it. When the MW is activated, it starts rotating on its axis. When the momentum wheel changes its angular velocity, its angular momentum changes accordingly. However, to maintain the conservation of angular momentum principle, if the momentum wheel changes its angular momentum, there must be an equal and opposite reaction within the system. In this case, the reaction is a torque exerted on the rest of the CubeSat. This torque causes a change in the orientation of the CubeSat with respect to the axis around which the momentum wheel is rotating.

The test requires a complex setup due to the requirement that on-orbit conditions should be simulated as closely as possible in order to obtain reliable estimates for expected on-orbit performance. In particular, the satellite should be in an almost 'free-free' configuration and the forces of gravity acting on the structure and the effects of the surrounding air should be minimized. As a general rule, the satellite should be supported such that the maximum natural frequency of the suspension is less than 25 % of the first structural mode. Suspension and potential gravity compensation devices may also help isolate the specimen from external disturbances that affect test performance [1].

To respond effectively to the test objectives and complete the related tasks, it is chosen to adopt two different setups: the first one (*A*) is simpler and allows verifying the correct integration of the sensor development board, while the second one (*B*), more representative of flight conditions, implements the use of a wire suspension system.

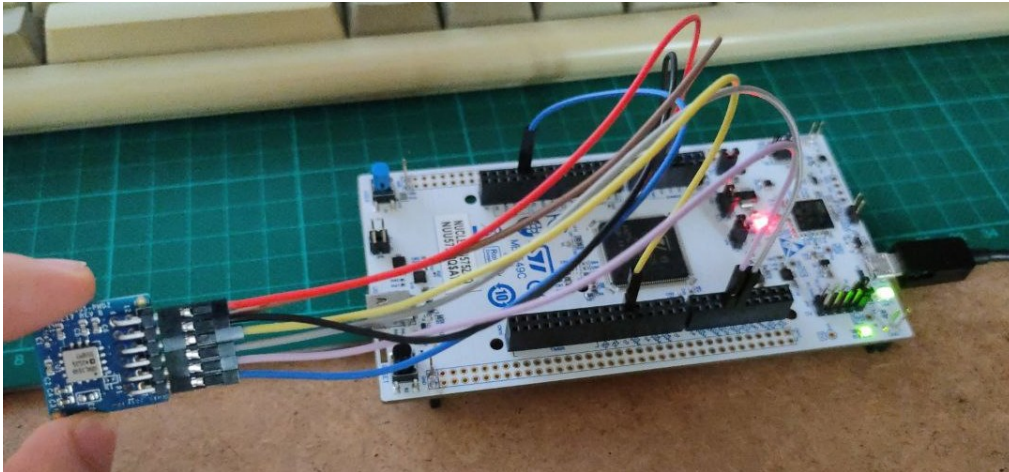### 6.3.1 *Setup A*

The setup *A,* used to verify the DM in the laboratory, is represented in Figure 35.
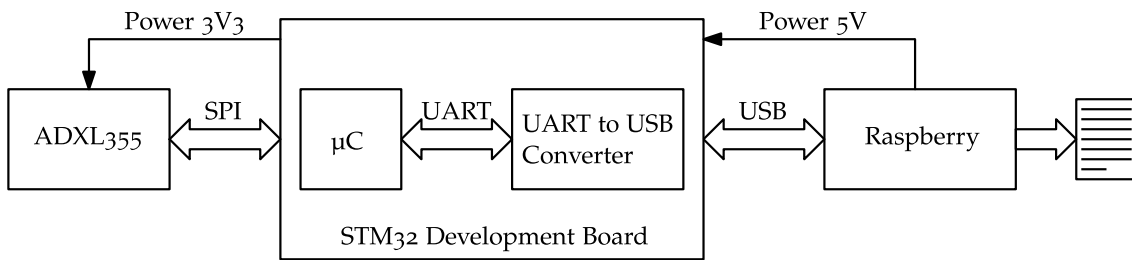
Figure 35 - Connection of the blocks for laboratory testing.

The evaluation board of the *ADXL355* is connected to the *NUCLEO-U575ZI-Q* microcontroller development board using the *SPI* protocol, thus forming the actual DM of the MVS (Figure 36).

Figure 36 - MVS Development Model.

The *Raspberry Pi 4* board replaces the OBC in the experimental setup. The *Raspberry Pi 4* is a single-board computer developed by the *Raspberry Pi Foundation*. It features:

- A quad-core *ARM Cortex-A72* processor;
- 4 *GB* of RAM;
- Multiple *USB* ports;
- Dual micro-*HDMI* ports for display output;
- Gigabit Ethernet port;
- Support for microSD card storage;
- Various connectors and headers for expansion and connectivity;
- Support for running various operating systems, including *Linux*-based distributions like *Raspbian*.

In this setup, the *Raspberry Pi* is connected to a monitor, mouse, and keyboard available in the laboratory. Furthermore, it is connected to the sensor DM via *UART* protocol and is externally powered at 5 *V* through a *USB-C* connector. A converter is used to generate the nominal voltage of 3.3 *V* for both the microcontroller and the accelerometer.

The described system is securely assembled on multiple levels using custom-made PVC structures at *ESAT*, as shown in Figure 37. Care was taken to position the accelerometer as close as possible to the MW and to secure the entire system using plastic straps.

During the tests, the *Raspberry Pi* board receives values from the microcontroller and writes a text file. This file is then loaded into the *MATLAB* computing environment for post-processing.

This initial setup allows to achieve the outlined objective 1. Indeed, it enables to verify the proper integration of the development board and, most importantly, test the functionality of the system software.
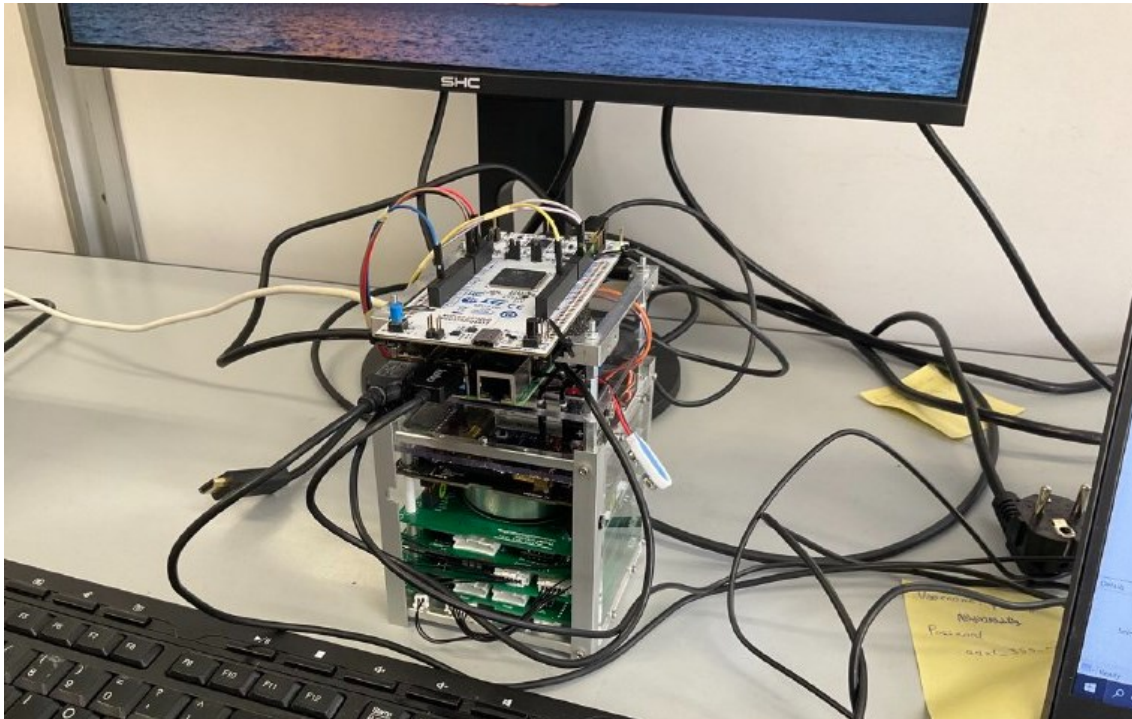
Figure 37 - Setup *A* Functional Test.

6.3.2 *Setup B*

The evolution of setup *A* involves the use of a structure capable of simulating the free-free boundary conditions. This is achieved by employing a wire suspension system designed for this purpose.

The design plans to use:

- A swivel hook with a low-friction bearing;
- Nylon 6,6 thread;
- 4 aluminium two eyelet turnbuckles;
- 2 spirit level;
- A screw with a diameter of 4 mm and a bolt at the end, at least 7 cm long;
- A battery capable of providing power to the *Raspberry Pi 4*;

The selected swivel hook is manufactured by the company *I-WILL* and has the following features:

- Made of 7075 aluminum alloy;
- Weighs 134 g;

102

- Allows 360° rotation with a low-friction self-lubricating ball bearing;
- Features a triangular shape at the ends to prevent the attached object from slipping easily;
- Tested with a maximum breaking load of 30 kN;
- *CE&EN* certified.

The double eyelet turnbuckle has the following characteristics:
- Eyelets with a diameter of 5 mm (ISO $M5$);
- Material: Galvanized steel;
- Weight: 350 g;
- Length (closed): 10 cm.

The length of the wires has been chosen to control the natural frequency of the suspension system. Assuming a simplified mass-spring system, where the suspended mass represents *ESAT* and the spring is the nylon wire, it is possible to calculate the natural frequency (f_n) using the formula:

$$f = \frac{1}{2\pi} \cdot \sqrt{\frac{k}{M}}$$

Where k represent the spring constant of the system and M the suspended mass;
Considering that:
- $E = 4\ GPa$ is the Young's modulus of the nylon 6,6;
- A is the cross-sectional area of the nylon wire (considered to have a diameter of $d = 0.6\ mm$);
- $L = 0.3\ m$ is the length of the wire;
- $M = 2.5\ kg$ (1 kg $ESAT$ + 4 $\cdot$ 350g $turnbuckles$):

$$k = \frac{E \cdot A}{L} = \frac{4\ GPa \cdot 0.2827\ mm^2}{300\ mm} = 3769.91\ N/m$$

Thus, the natural frequency of the system f_n is approximately 6.18 Hz.

A nylon wire (fishing line) with a diameter of $0.6\ mm$ can typically withstand forces of around $20\ kg$, making it suitable for the required application.

The swivel hook will be attached to a ceiling hook in the laboratory. At its lower end, it will be connected via a $15\ cm$ long nylon wire to a turnbuckle that allows four turnbuckles to be connected together. The bolt in the turnbuckle ensures the secure locking of the turnbuckles. Each turnbuckle will be connected at the bottom to a nylon wire tied to one end of *ESAT*. The aluminium turnbuckles are necessary to balance the system. To evaluate the proper balance of the CubeSat, two spirit levels will be used to position them above *ESAT*. The turnbuckles will be extended or contracted until the system is levelled.

Compared to setup *A*, the *Raspberry Pi* will be appropriately connected to a battery capable of powering it and will be linked to the computer through a wireless connection to extract the necessary data. In this setup, indeed, to faithfully replicate orbital conditions, it is necessary to eliminate all external connections to the test mockup; wiring systems for power or data exchange would disrupt the free-free boundary conditions.

Below the suspension system, a microfiber cloth will be used to protect the instrumentation from accidental damage in case of a fall. The microfiber cloth will act as a protective layer, absorbing and cushioning any impact to minimize the risk of damage to the equipment. This additional safety measure is essential to ensure the integrity and functionality of the payload during testing and handling. The microfiber cloth is soft and has non-abrasive properties that make it an ideal choice for providing a gentle yet effective protective barrier for the sensitive components of the payload.

Figure 38 displays the complete setup *B*.

Setup *B*, being more representative of flight conditions, ensures the possibility of fulfilling the second testing objective by ensuring that the sensor can collect data correctly as required by the requirements.
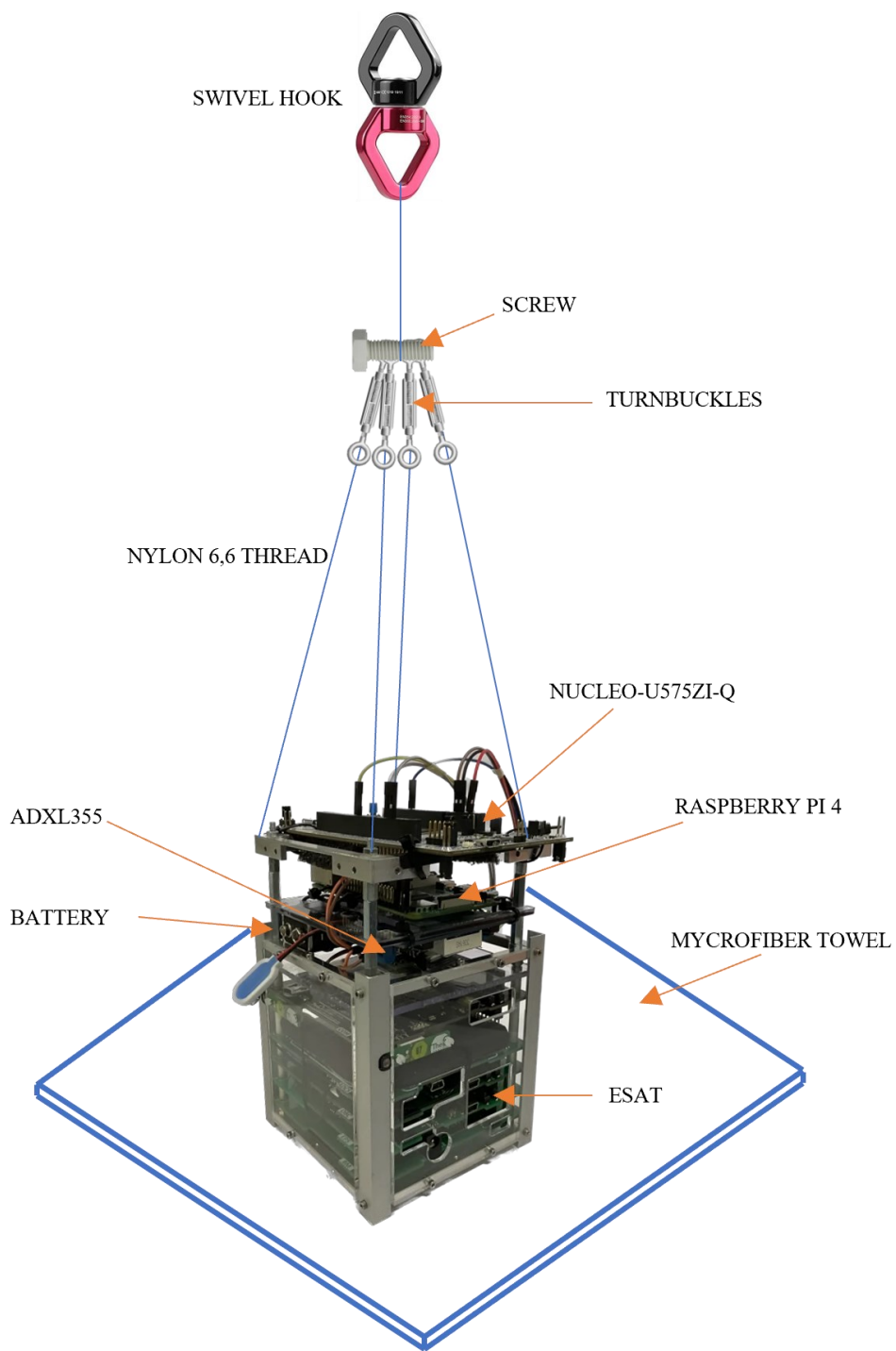
Figure 38 - Setup *B* Functional Test.

6.4 **GSE and test Tools Required**

To complete the equipment, a computer located in the laboratory will be used, which will be connected to *ESAT* and the payload under test. The computer will serve as the central control and data acquisition unit for the entire testing process. It will be responsible for sending commands to *ESAT* and the payload, receiving data from the sensors, and recording and analysing the test results. The computer will be equipped with the necessary interfaces and software to communicate with *ESAT* and the payload. It will be able to send commands and receive real-time data from the *Raspberry*, allowing for precise control and monitoring of the test conditions. Additionally, the computer will store and manage the test data, enabling comprehensive data analysis and post-processing. This will facilitate the evaluation of the payload performance, the verification of test objectives, and the identification of any anomalies or deviations from expected results. By using the laboratory computer as part of the equipment, the testing process will be efficient, reliable, and well-documented, ensuring that valuable data is collected and processed accurately for the proper evaluation of the payload microvibration sensing capabilities. Finally, other laboratory tools such as oscilloscopes, screwdrivers, 3D printers, and other instruments can be used if needed.

6.5 **Background Noise**

The background noise must be compared with the acceptable disturbance level requirement. The background noise density should be lower than $100 \, \mu g/\sqrt{Hz}$, as established during the sensitive element design phase. In the technical specifications provided by the manufacturer *Analog Devices*, *Inc.*, for the *ADXL355* sensor, the typical background noise (*RMS*) is indicated as $25 \, \mu g/\sqrt{Hz}$ at a $1 \, Hz$ noise bandwidth.

As per the Figure 39, measures can be implemented to mitigate disturbance sources.

Noise source	Frequency band	Countermeasures
• **Electromagnetic noise:**		
electrical noise from main supply (50 Hz and harmonics)	narrow band noise appearing on spectra lines	proper grounding of equipment
tonal noise induced by rotating machinery and illumination systems		- remove light sources - appropriate shielding
internal amplifiers and acquisition system noise	in general 1/f broadband noise, characteristic of equipment	selection of high quality, low noise electronics
instrumentation noise (piezo-electric accelerometers, force cells)		use of high sensitivity sensors, with reduced amplifier volt level
signal conditioning, amplification and acquisition		use of very low noise electronics
• **Acoustic noise:**		
coupling of test article with surrounding air	broadband noise with relevant frequency components in the band of interest for the test	- test at night without air-conditioning, laminar flux off and reduced human activity close to the test room, - potential encapsulation of complete test set-up in at for better isolation (while maintaining clean air conditions),
acoustic perturbations reaching the satellite structure		- potential use of acoustic enclosure; better however to use vacuum chamber
• **Ground-borne noise (ground vibration input):**	low to mid-frequency (250 – 300 Hz) range for transportation noise (e.g. truck or train)	special seismic isolation devices for noise filtering, use of proper suspension devices for test article
• **Signal processing noise:**	broadband noise	adequate signal processing to improve signal-to noise ratio

Figure 39 - Classification of noise sources affecting microvibration tests [1].

6.6 Operation Mode

The vibrations of the reaction wheels are recorded during three operational modes:

- Coast down mode: the wheel is accelerated to its maximum speed of $8000\ rpm$, and then the input power is removed, allowing the wheel to slow down gradually due to its internal friction. Microvibrations of the wheel are continuously recorded during this test.

- Constant speed mode: the wheel speed is maintained at a constant level. Microvibrations emitted during constant speed are recorded, typically for a couple of minutes.

For each operational mode, tests are conducted for a duration of 3 minutes ($\cong 10\ s$ for each sampling $\times$ 10 acquisition for PSD).

6.7 Test Conditions

The test conditions must be established according to [22], adopting appropriate margins and utilizing relevant ground environments. The control of cleanliness and contamination for the test programs shall conform to ECSS-Q-ST-20-07.

The Electrical Ground Support Equipment (EGSE) or other support systems for the test item must:

- Not compromise the test results;
- Be immune to signals used for sensitivity tests;
- Be designed to comply with applicable legislation, including safety regulations (e.g., EC Directives).

Therefore, it has been chosen to conduct the functional tests at the laboratory of the DII at the University of Padova, which meets the necessary safety requirements for test execution.

The following precautions are further imposed:

- The test area is thoroughly cleaned immediately before conducting the tests;
- External electromagnetic sources not essential to the test are turned off in the vicinity of the test setup;

- Tests are conducted in natural sunlight to eliminate potential background noise from artificial lighting;
- Air conditioning systems are turned off to limit acoustic noise from these devices.

The test setup, test levels, and operational procedures must not create conditions that could:
- Induce failures in the test item;
- Create hazardous situations.

The temperature recorded in the test area must be between $15°C$ and $30°C$, allowing both the described instruments to operate within their operational range and the selected personnel to perform the tests without requiring air conditioning measures.

6.8 Test Tolerances

The tolerance bands for the tests must be specified in the test error budgets and agreed upon before conducting them. As a result, the tolerances must be justified with reference to the uncertainty budget and confidence level of the measurement instrument(s) used. The test tolerances are listed in Table 15.

Table 15 - Test tolerances.

Test Parameters	Tolerances
Acceleration	$\pm\,10\,\%$
Data stored	$\pm\,10\,\%$
Background noise	$\pm\,10\,\%$
Test duration	$\pm\,20\,\%$

6.9 Test Accuracies

The test accuracies must be specified in the test error budgets and agreed upon before conducting the tests. Table 16 provides the assigned accuracy values for the functional tests of the payload.

Table 16 - Test accuracies.

Test Parameters	Accuracy
Acceleration	$\pm\,0.1\,\mu g$
Amplitude of microvibration	$\pm\,0.1\,mN$
Ambient temperature	$\pm\,0.5\,°C$
Voltage supply	$\pm\,0.1\,V$
Sampling frequency	$\pm\,100\,Hz$
Test duration	$\pm\,1\,min$

Any anomaly in the test equipment, detected during the initial calibration, must be reported.

6.10 Functional Test Progress

As of the completion of this thesis, the MVS DM has been successfully assembled with the microcontroller and accelerometer correctly connected. Additionally, significant progress has been made in laying the groundwork for setup *A*, primarily focusing on testing the interconnections among the various components. Nevertheless, it should be noted that the full implementation outlined in this FTP remains pending. It is anticipated that all the planned functional tests will be executed and concluded by the conclusion of the year 2023.

CONCLUSIONS AND FUTURE WORKS

In conclusion, this thesis has explored the intricate realm of microvibrations in satellites. Research on microvibrations characterization is currently a significant concern in satellite structural dynamics due to the challenges these disturbances present to the modern, highly sensitive payloads aboard spacecraft. For instance, in ECSS-E-HB-32-26A [1], the largest chapter is dedicated to the topic of microvibrations and microdynamics.

Following a thorough literature review, the historical context of challenges related to microvibrations faced by various space missions was discussed, emphasizing the increasing importance of addressing this issue, particularly in the context of CubeSats.

The in-depth examination of disturbance sources and the detailed analysis of microvibrations induced by MWs shed light on the complexities and nuances of this problem. This knowledge proved crucial for the development of effective solutions and served as the starting point for characterizing the design of a sensor capable of detecting microvibrations.

The thesis focuses on the design of a microvibration sensor as a payload for a CubeSat. This innovative payload is contextualized in the AlbaSat mission of the University of Padova, selected by the ESA as part of the "Fly Your Satellite!" project. The foundations were laid for the realization of the MVS, meticulously describing its objectives, physical and functional architecture, and the selection of key components, such as the *ADXL355* accelerometer and the *STM32U575* microcontroller. The work done so far has been approved by both the development team and ESA FYS reviewers.

Furthermore, the last chapter defines the FTP as a fundamental guide for evaluating the functionality of the MVS payload. Two different test sets, Setup *A* and Setup *B*, were outlined to address various aspects of payload performance. GSE and test tools were identified to facilitate these tests, taking into account issues such as background noise, operating mode, test conditions, tolerances, and accuracies.

The Setup *A* has been successfully implemented, enabling the achievement of the first objective of the functional tests. Tests on Setup *B* will be conducted by the team at a later stage.

Looking ahead, there are several avenues for research and development:
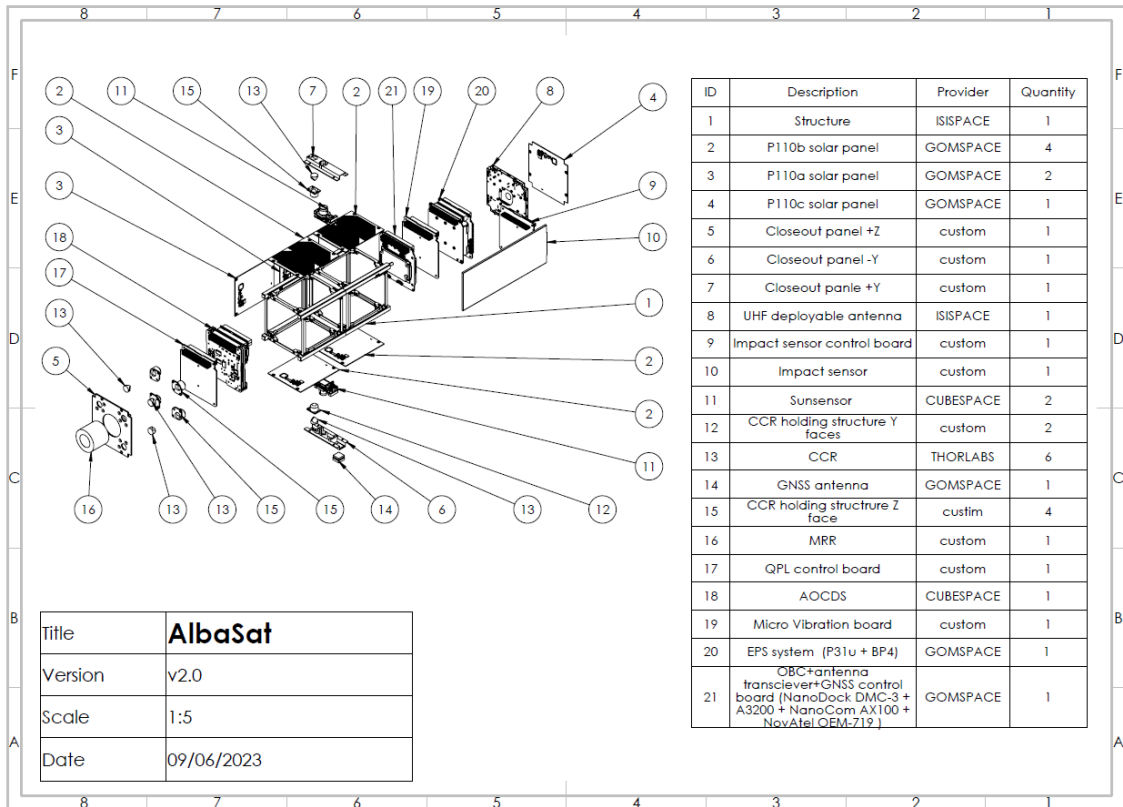
- *Complete Test Implementation*: The full execution of functional tests is pending. The upcoming year, 2023, promises to complete these tests, providing valuable insights into the performance of the MVS payload;

- *Advanced Payloads*: Knowledge gained from this research can be applied to the development of more advanced payloads for microvibration detection. This may include exploring new sensor technologies, improved capabilities of microcontrollers, and enhanced data processing techniques;

- *Integration with new CubeSats*: Integrating the MVS payload with CubeSats, as tested in Setup B, opens the door to future CubeSat missions prioritizing microvibration management for equipment requiring specific control, such as optical instruments. Future work can explore integrating this technology into more advanced CubeSat missions;

- *Qualification Testing*: While functional tests are crucial, environmental tests are equally vital. Future research may include qualification tests to validate the payload performance under the rigorous conditions of space;

- *Data Analysis and Validation*: Data collected from functional tests will require thorough analysis and validation. This involves not only assessing payload performance but also validating the data products it generates.

In conclusion, this thesis has laid the groundwork for the development of a payload capable of measuring microvibrations in CubeSats, with specific attention to the AlbaSat mission. The FTP and insights derived from this research will contribute to the successful development of the MVS. The future holds promising opportunities to advance knowledge and capabilities in this critical sector of space technology.

APPENDIX A
OVERALL VIEW OF THE ALBASAT CUBESAT

ID	Description	Provider	Quantity
1	Structure	ISISPACE	1
2	P110b solar panel	GOMSPACE	4
3	P110a solar panel	GOMSPACE	2
4	P110c solar panel	GOMSPACE	1
5	Closeout panel +Z	custom	1
6	Closeout panel -Y	custom	1
7	Closeout panle +Y	custom	1
8	UHF deployable antenna	ISISPACE	1
9	Impact sensor control board	custom	1
10	Impact sensor	custom	1
11	Sunsensor	CUBESPACE	2
12	CCR holding structure Y faces	custom	2
13	CCR	THORLABS	6
14	GNSS antenna	GOMSPACE	1
15	CCR holding structrure Z face	custim	4
16	MRR	custom	1
17	QPL control board	custom	1
18	AOCDS	CUBESPACE	1
19	Micro Vibration board	custom	1
20	EPS system (P31u + BP4)	GOMSPACE	1
21	OBC+antenna transciever+GNSS control board (NanoDock DMC-3 + A3200 + NanoCom AX100 + NovAtel OEM-719)	GOMSPACE	1

Title	**AlbaSat**
Version	v2.0
Scale	1:5
Date	09/06/2023

Figure 40 - Overall view of the AlbaSat CubeSat.

APPENDIX B
LINEAR MATHEMATICAL MODEL OF MWA

The linear mathematical model of the MWA, also adopted for the momentum wheel of AlbaSat, can be schematically represented in Figure 41.
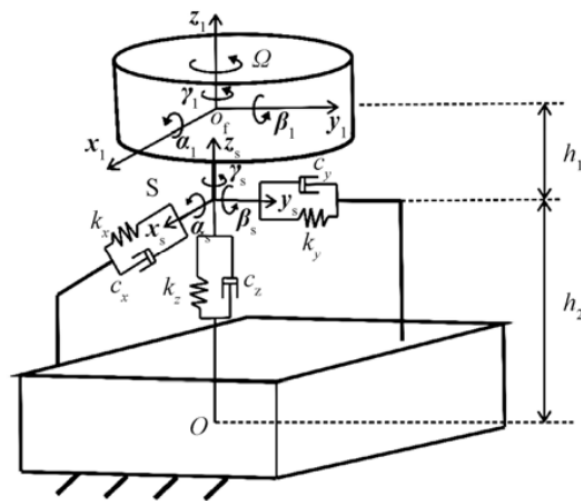

Figure 41 - Sketch of the mathematical model
[9].

The ball bearings elastic support effect is symbolized by an elastic component denoted as S. This component imparts a linear stiffness matrix to the flywheel. The coordinates $o_f x_1 y_1 z_1$ represent the body center at the mass centre of the flywheel o_f, while h_1 signifies the vertical distance from o_f to S. Similarly, h_2 stands for the vertical distance from S to the center of the mounted plane of the MWA, denoted as O.

$x_1, y_1, z_1, \alpha_1, \beta_1, \gamma_1$ are displacement vectors of the body coordinates of the flywheel to its inertial coordinate; $x_s, y_s, z_s, \alpha_s, \beta_s, \gamma_s$ are the relative displacement vectors of the elastic element S. k_x, k_y, k_z are the force coefficients in the x, y, z directions of the body coordinate respectively. Ω is the rotational angular speed.

By applying the Euler equations, neglecting the effects of higher-order terms, and assuming small angles ($\sin(\alpha) \approx \alpha, \cos(\alpha) \approx 1$), it is possible to derive the linear equations of motion for the MWA:

$$\begin{cases} f_1 = M_1\ddot{x}_1 + G\,\dot{x}_1 + T_{s1}C_sT_{sx_1}\dot{x}_1 + T_{s1}K_sT_{sx_1}x_1 \\ \qquad f_2 = T_{s2}C_sT_{sx_1}\dot{x}_1 + T_{s2}K_sT_{sx_1}x_1 \end{cases}$$

where M_1 is the mass matrix of the flywheel in body coordinate; G the gyroscopic matrix in the body coordinate; C_s the nonrotational damping mass matrix at S; K_s stiffness matrix of the elastic element S; f_1 the input disturbance force vector at the mass centre of the flywheel; f_2 the output disturbance force vector at the base mount centre O; T_{sx1} the displacement transfer matrix; T_{s1} and T_{s2} are the force transfer matrices.

Note that there is $h_1 = 0$, because the MWA is axial symmetrically supported in this paper. In addition, the damping matrix C_s is assumed to be zero in this Master thesis.

The terms in the system of equations indicated above are as follows:

$$M_1 = \begin{bmatrix} m_1 & 0 & 0 & 0 & 0 & 0 \\ 0 & m_1 & 0 & 0 & 0 & 0 \\ 0 & 0 & m_1 & 0 & 0 & 0 \\ 0 & 0 & 0 & I_{1xx} & 0 & 0 \\ 0 & 0 & 0 & 0 & I_{1yy} & 0 \\ 0 & 0 & 0 & 0 & 0 & I_{1zz} \end{bmatrix}$$

$$T_{sx1} = \begin{bmatrix} 1 & 0 & 0 & 0 & -h_1 & 0 \\ 0 & 1 & 0 & h_1 & 0 & 0 \\ 0 & 0 & 1 & 0 & 0 & 0 \\ 0 & 0 & 0 & 1 & 0 & 0 \\ 0 & 0 & 0 & 0 & 1 & 0 \\ 0 & 0 & 0 & 0 & 0 & 1 \end{bmatrix}$$

$$K_s = \begin{bmatrix} k_x & 0 & 0 & 0 & 0 & 0 \\ 0 & k_y & 0 & 0 & 0 & 0 \\ 0 & 0 & k_z & 0 & 0 & 0 \\ 0 & 0 & 0 & k_\alpha & 0 & 0 \\ 0 & 0 & 0 & 0 & k_\beta & 0 \\ 0 & 0 & 0 & 0 & 0 & k_\gamma \end{bmatrix}$$

$$G = \begin{bmatrix} 0 & 0 & 0 & 0 & 0 & 0 \\ 0 & 0 & 0 & 0 & 0 & 0 \\ 0 & 0 & 0 & 0 & 0 & 0 \\ 0 & 0 & 0 & 0 & \Omega I_{1zz} & 0 \\ 0 & 0 & 0 & -\Omega I_{1zz} & 0 & 0 \\ 0 & 0 & 0 & 0 & 0 & 0 \end{bmatrix}$$

117

$$C_s = \begin{bmatrix} c_{sx} & 0 & 0 & 0 & 0 & 0 \\ 0 & c_{sy} & 0 & 0 & 0 & 0 \\ 0 & 0 & c_{sz} & 0 & 0 & 0 \\ 0 & 0 & 0 & c_{s\alpha} & 0 & 0 \\ 0 & 0 & 0 & 0 & c_{s\beta} & 0 \\ 0 & 0 & 0 & 0 & 0 & c_{s\gamma} \end{bmatrix}$$

$$T_{s1} = \begin{bmatrix} 1 & 0 & 0 & 0 & 0 & 0 \\ 0 & 1 & 0 & 0 & 0 & 0 \\ 0 & 0 & 1 & 0 & 0 & 0 \\ 0 & h_1 & 0 & 1 & 0 & 0 \\ -h_1 & 0 & 0 & 0 & 1 & 0 \\ 0 & 0 & 0 & 0 & 0 & 1 \end{bmatrix}$$

$$T_{s2} = \begin{bmatrix} 1 & 0 & 0 & 0 & 0 & 0 \\ 0 & 1 & 0 & 0 & 0 & 0 \\ 0 & 0 & 1 & 0 & 0 & 0 \\ 0 & -h_2 & 0 & 1 & 0 & 0 \\ h_2 & 0 & 0 & 0 & 1 & 0 \\ 0 & 0 & 0 & 0 & 0 & 1 \end{bmatrix}$$

BIBLIOGRAPHY

[1] ECSS-E-HB-32-26A, *Space engineering, Spacecraft mechanical loads analysis handbook,* Noordwijk: Requirements & Standards Division, 2013.

[2] M. P. Le, "Micro-disturbances in reaction wheels," Technische Universiteit Eindhoven, 2017.

[3] C. Dennehy and O. S. Alvarez-Salazar, "Spacecraft Micro-Vibration: A Survey of Problems, Experiences, Potential Solutions, and Some Lessons Learned," *Computer Science,* 2018.

[4] D. Addari, "A semi-empirical approach for the modelling and analysis of microvibration sources on-board spacecraft," 2016.

[5] F. Mingione, "Microvibration test bench for tiny reaction wheels," Delft University of Technology, 2022.

[6] H. Polat et al., "Survey, Statistical Analysis and Classification of Launched CubeSat Missions with Emphasis on the Attitude Control Method," *Journal of Small Satellites,* vol. 5, pp. 513-530, 2016.

[7] L. Meza et al., "Line of Sight Stabilization of James Webb Space Telescope," in *28th Annual AAS Guidance and Control Conference*, Breckenridge, Colorado, 2005.

[8] F. Dekens et al., "Kite: Status of the External Metrology Testbed for SIM," *SPIE Conference on Astronomical Telescopes and Instrumentation,* 2004.

[9] W. Zhou, D. Li, Q. Luo e K. Liu, «Analysis and Testing of Microvibrations Produced by Momentum Wheel Assemblies,» *Chinese Journal of Aeronautics,* vol. 25, pp. 640-649, 2012.

[10] R. A. Masterson, «Development and validation of empirical and analytical reaction wheel disturbance models,» Massachusetts Institute of Technology, 1999.

[11] L. Elias and D. Miller, "A coupled disturbances analysis method using dynamic mass measurement techniques," in *43rd AIAA/ASME/ASCE/AHS/ASC Structures, Structural Dynamics, and Materials Conference*, Denver, Colorado, 2002.

[12] T. Shigemune and O. Yoshiaki, "Experimental and Numerical Analysis of Reaction Wheel Disturbances," *JSME International Journal Series C Mechanical Systems,* vol. 46, pp. 519-526, 2003.

[13] W.-Y. Zhou, G. S. Aglietti and Z. Z, "Modelling and testing of a soft suspension design for a reaction/momentum wheel assembly," *Journal of Sound and Vibration,* vol. 330, pp. 4596-4610, 2011.

[14] B. Noda and T. Momono, "Sound and Vibration in Rolling Bearings," NSK, Motion and Control No. 6, 1999.

[15] W. Salah, D. Ishak and K. J. Hammadi, "Minimization of torque ripples in bldc motors due to phase commutation-a review," *Przegląd Elektrotechniczny,* vol. 87, pp. 183-188, 2011.

[16] L. Soula and G. Laduree, "Modelling Micro-vibrations by Finite Element Model Approach," in *12th European Conference on Spacecraft Structures, Materials and Environmental Testing*, Noordwijk, The Netherlands, 2012.

[17] J. Borgharts and P. Le, "Results of Torque Instability Characterization," Bradford report RWU-BE-TN-30004, 2014.

[18] B. Bialke, "Microvibration disturbance fundamentals for rotating mechanisms," in *34th Annual Guidance and Control Conference*, 2011.

[19] Galeazzi, Marucchi-Chierro and Holtz, "Experimental activities on ARTEMIS for the micro-vibration verification," in *Proc. Conference on Spacecraft Structures, Materials & Mechanical Testing*, 1996.

[20] CubeSpace, "CubeWheel Gen1," 2021. [Online]. Available: https://www.cubespace.co.za/products/gen-1/actuators/cubewheel/.

[21] ECSS-E-ST-10-02C, *Space engineering, Verification,* Noordwijk: Requirements & Standards Division, 2009.

[22] ECSS-E-ST-10-03C, *Space engineering, Testing,* Noordwijk: Requirements & Standards Division, 2012.

[23] I. Latachi, T. Rachidi, M. Karim and A. Hanafi, "Reusable and Reliable Flight-Control Software for a Fail-Safe and Cost-Efficient Cubesat Mission: Design and Implementation," *Aerospace,* vol. 7, no. 10, p. 146, 2020.

[24] Analog Devices, "ADXL355 Datasheet and Product Info," 2020. [Online]. Available: https://www.analog.com/en/products/adxl355.html.

[25] STMicroelectronics, "STM32U575/585 - PDF Documentation," [Online]. Available: https://www.st.com/en/microcontrollers-microprocessors/stm32u575-585/documentation.html.

[26] Y. Surel, "CubeSat for In-Orbit technology verification: on-ground characterisation, qualification testing activity planning and results.," 2019.

[27] I. Gavrilovich, "Development of a robotic system for CubeSat Attitude Determination and Control System ground tests," 2016.

[28] J. F. Gómez, "ESAT- The Educational Satellite developed by Theia Space," 2021. [Online]. Available: https://www.theia.eusoc.upm.es/esat/.